Zn-VI/Cu_2O Heterojunctions for Earth-Abundant Photovoltaics

Thesis by

Samantha Wilson

In Partial Fulfillment of the Requirements

for the Degree of

Doctor of Philosophy

California Institute of Technology

Pasadena, California

2015

(Defended December 10, 2014)

Acknowledgments

I have worked with many people in the years I've been at Caltech, and I would like to acknowledge the people who helped me with my research. First I would like to thank my adviser, Professor Harry Atwater, for allowing me to join the Atwater group many years ago. Harry has always been a source of fantastic research ideas and boundless optimism and he has aided me greatly in my time at Caltech. I would also like to thank my thesis committee, Professor Julia Greer, Professor William Johnson, and Professor Austin Minnich, for taking time out of their busy schedules to critique my defense.

I would also like to acknowledge my manuscript coauthors and research collaborators over the years, including Dr. Chengxiang Xiang, Dr. Greg Kimball, Dr. Davis Darvish, Dr. Jeff Bosco, Dr. David Scanlon, Yulia Tolstova, Jianchi Chen, and Stefan Omelchenko. I would also like to thank the entire earth-abundant solar research team, including Naomi Coronel, Faisal Tajdar, Amanda Shing, and Dr. Lise Lahourcade. All the work in this thesis directly benefited from these individuals' advice and critic.

My research project would not have been possible with the collaboration and support of The Dow Chemical Company, whose grant funded the entire earth-abundant solar effort at Caltech. Additionally I would like to thank Dr. James Stevens, Dr. Marty DeGroot, Dr. Rebekah Feist, and Dr. Robert Wright for taking the time to meet with us and review our research regularly for 5 years. Most of my ideas were a direct result of those research meetings.

I have done much of my work in the Molecular Materials Research Center at

Caltech, where I have made extensive use of the materials characterization equipment and the expertise of the staff. I would like to thank Bruce Brunschwig and all of the graduate lab assistants that keep that facility running.

Most of the research in the thesis relates to analyzing thin films I deposited in the Atwater sputterer and I would like to thank all the Atwater graduate students who have been responsible for keeping the sputterer running, including Dr. Andrew Leenheer, Carrisa Eisler, Sunita Darbe, Dr. Jing-Shun Huang, Dr. Jonathon Grandidier and many others. I would not have been able to complete this research without the sputter being continuously operational for nearly 6 years.

Finally I would like to thank all the other members of the Atwater group that I did not specifically name. Thank you to everyone for keeping all the equipment running, being available to help out in the lab at any time, and just generally being great!

Abstract

The need for sustainable energy production motivates the study of photovoltaic materials, which convert energy from sunlight directly into electricity. This work has focused on the development of Cu_2O as an earth-abundant solar absorber due to the abundance of its constituent elements in the earth's crust, its suitable band gap, and its potential for low cost processing. Crystalline wafers of Cu_2O with minority carrier diffusion lengths on the order of microns can be manufactured in a uniquely simple fashion — directly from copper foils by thermal oxidation. Furthermore, Cu_2O has an optical band gap of 1.9 eV, which gives it a detailed balance energy conversion efficiency of 24.7% and the possibility for an independently connected Si/Cu_2O dual junction with a detailed balance efficiency of 44.3%.

However, the highest energy conversion efficiency achieved in a photovoltaic device with a Cu_2O absorber layer is currently only 5.38% despite the favorable optical and electronic properties listed above. There are several challenges to making a Cu_2O photovoltaic device, including an inability to dope the material, its relatively low chemical stability compared to other oxides, and a lack of suitable heterojunction partners due to an unusually small electron affinity. We have addressed the low chemical stability, namely the fact that Cu_2O is an especially reactive oxide due to its low enthalpy of formation (ΔH_f^0 = -168.7 kJ/mol), by developing a novel surface preparation technique. We have addressed the lack of suitable heterojunction partners by investigating the heterojunction band alignment of several Zn-VI materials with Cu_2O. Finally, We have addressed the typically high series resistance of Cu_2O wafers

by developing methods to make very thin, bulk Cu_2O, including devices on Cu_2O wafers as thin as 20 microns. Using these methods we have been able to achieve photovoltages over 1 V, and have demonstrated the potential of a new heterojunction material, Zn(O,S).

Contents

List of Figures

List of Tables

List of Publications

Portions of this thesis have been drawn from the following publications:

Samantha S. Wilson, Jeffrey P. Bosco, Yulia Tolstova, David O. Scanlon, Graeme W. Watson, and Harry A. Atwater. "Interface Stoichiometry Control to Improve Device Voltage and Modify Band Alignment in ZnO/Cu_2O Heterojunction Solar Cells" *Energy & Environmental Science,* 7:3606-3610, 2014.

Samantha S. Wilson, Jeffrey P. Bosco, Yulia Tolstova, David O. Scanlon, Graeme W. Watson, and Harry A. Atwater. "Valence Band Engineering in Zn-VI/Cu_2O Heterojunctions for Improved Photovoltaic Device Voltage" *To be submitted.*

Samantha S. Wilson, Chengxiang Xiang, Yulia Tolstova, Nathan S. Lewis, and Harry A. Atwater. Thin, free-standing Cu_2O substrates via thermal oxidation for photovoltaic devices" *Proceedings of the 38th IEEE Photovoltaic Specialists Conference,* 2012.

Samantha S. Wilson, Jeffrey P. Bosco, Yulia Tolstova, David O. Scanlon, Graeme W. Watson, and Harry A. Atwater. "Interface stoichiometry control in ZnO/Cu_2O photovoltaic devices" *Proceedings of the 39th IEEE Photovoltaic Specialists Conference,* 2013.

Chapter 1

Introduction to Cuprous Oxide as a Photovoltaic Material

Currently, much of the power in the United States is generated by methods that produce troubling amounts of carbon and are inefficient. In 2013, the United States consumed 97.6 quadrillion BTU of energy, with 14.7 quadrillion BTU being direct electricity consumption [3]. Much of the difference in energy consumption is due to the inefficiency of producing electricity from carbon. The sun represents a large source of untapped energy, as about 41,000 quadrillion BTU of energy are incident on the area of the continental United States annually [1]. However, only 0.3 quadrillion BTU of consumed energy was generated from solar power in 2013 [3].

One way to capture energy from this effectively unlimited source is through photovoltaics, which describes the study of optoelectronic devices that convert sunlight into power. Commercial photovoltaic technologies have reached a $/watt value on par with the price of grid electricity, but each of the these technologies (CdTe, CIGS, silicon, and amorphous silicon) have fundamental limitations that make them less then ideal for meeting large scale energy production demands. For example, solar cells made with silicon as the absorbing material are costly to process due to its high temperature requirements and large amounts of energy required to extract elemental silicon from SiO_2. Amorphous silicon has never reached a high efficiency in research cells despite the large number of man hours dedicated to the effort. And finally, CIGS, and CdTe contain constituent elements that are not abundant enough in the earths crust to allow production of enough material to reach large scale energy production [1].

We choose study cuprous oxide (Cu_2O) in part because the abundance of its constituent elements means it can be manufactured in sufficient quantity to meet much of the energy demands of the United States [62]. Additionally, calculations based on the optical properties of Cu_2O indicate that it has a high thermodynamic limit to power conversion efficiency, which should enable high efficiency devices. Synthesizing Cu_2O is also uniquely simple, as wafers of Cu_2O can be derived directly from Cu foils [42]. However, Cu_2O has not been extensively studied as a photovoltaic material, and the current record energy conversion efficiency is only 5.38% [37]. In this thesis we will detail the material's properties, uniquely simple processing, and elemental abundance, all of which make Cu_2O an intriguing solar material worthy of additional study. Additionally we will detail the challenges to photovoltaic device fabrication that lead to the low demonstrated efficiency, and the work we are doing to mitigate the challenges of these materials.

1.1 Introduction to Photovoltaics

Photovoltaic devices convert sunlight directly into electricity through the photovoltaic effect, or the creation of and electronic current in a semiconductor under illumination. In this section we will briefly describe the physics of photovoltaics in order to understand the material requirements for an efficient solar cell. Photovoltaic devices, or solar cells, are quite simply diodes. They are built from the junction of two semiconductors with different chemical potentials, or Fermi levels, and different majority carrier types. When the two materials are put into physical and diffusive contact, holes flow from the p-type material into the n-type material and electrons flow from the n-type into the p-type material until equilibrium is established. When the carriers diffuse through the junction they leave behind exposed ion cores which are positively charged in the n-type material and negatively charged in the p-type material. Thus a dipole is created at the interface in equilibrium. The dipole is directed to resist the flow of majority carriers through the junction and thus is the origin of the classic current-voltage character of a diode. When a positive voltage is applied to a diode, current flow increases exponentially as the applied bias shrinks the width of the dipole region; this region is also called the space charge region or depletion width due to the lack of free carriers. On the other hand, a negative bias increases the width of the space charge region, decreasing current flow. Thus diodes only allow current flow under positive bias due to the presence of an interface dipole, and the dipole originates from joining two semiconductors with different Fermi levels.

When a semiconductor like silicon is illuminated, the photons with energy above the band gap can excite an electron-hole pair. In p-type silicon the majority carrier is holes, and the number of holes will be relatively unaffected by creation of electron-hole pairs under illumination. However, the number of minority carriers, in this case electrons, will increase by several orders of magnitude. The interface dipole is directed to prevent the flow of majority carriers, but minority carriers will be swept through by the high voltage if they diffuse to the edge of the space charge region. Thus the photo-generated minority carriers that diffuse to the edge of the space charge region

produce a sizable current in the opposite direction to the majority carriers, allowing a light generated current to be collected. However, the collection of a current does not automatically generate power, as voltage must be produced as well. The photovoltaic effect arises from preventing some of the photo-generated current from exiting the solar cell. The dipole serves to restrict the electrons to the n-type side and the holes to the p-type side. If excess holes and electrons are prevented from exiting the device, an electric field builds up in opposition to the existing interface dipole, reducing the net electric field and changing the equilibrium condition. The carriers extracted now have both a voltage and a current, and thus we are generating power. The ratio of the extracted electric power to the incident solar power is defined as the power conversion efficiency [24, 41, 55]. The current-voltage characteristic of solar cells will be explored in depth in Chapter 6.

Now that we understand how power generation in a photovoltaic cell works, we can identify several material properties that allow for more efficient power generation. First light must be absorbed, which is dependent both on the band gap and extinction coefficient of a material. Band gaps in the energy range of the solar spectrum (0.5-2.5 eV) paired with high absorption are favorable. Next, the photo-generated minority carriers must be able to diffuse to the space charge region because only minority carriers that travel through the junction contribute to the photovoltaic effect. Thus minority carrier diffusion lengths must be longer than light absorption lengths. Finally, the magnitude of the interface dipole, which indicates the magnitude of the photovoltaic effect, depends on the chemical potential difference between the two materials. Thus the materials used to make the junction must be capable of being doped, either intrinsically or extrinsically, to maximize the chemical potential difference between two materials [24, 41]. We will explain why we believe Cu_2O meets all these requirements in Chapter 2.

There are three materials that currently dominate the commercial photovoltaic market: silicon, CIGS, and CdTe. Silicon is the most mature technology and is the most widely deployed as well. It has several material advantages, including the fact that it can be doped both n- and p-type, allowing the formation of a homojunction,

or a p-n junction built from the same material. Additionally, it has an extremely long minority carrier diffusion length, allowing efficient collection of all light generated carriers. However, Si has some disadvantages as a solar material. It has an indirect band gap, which means it takes several hundred microns of material to absorb all light with energy above the band gap. Additionally, the production of the silicon wafers used to make silicon based solar cells is an energy intensive process that involves melting the purified silicon and re-condensing it as a single crystal. Thus silicon cells have much longer energy payback times, on the order of several years [1]. The other two commercially produced solar materials are CIGS and CdTe, which are produced as approximately 1 micron thick thin films. CIGS, or sometimes just CIS, is a copper-indium-gallium-selenide-sulfur alloy. Varying the ratio of the constituent elements alters properties like the band gap and carrier concentrations. CIGS is can only be doped p-type, thus CdS is used as an n-type partner to form a heterojunction, or a p-n junction of dissimilar materials. CdTe is also a p-type solar absorber that forms a heterojunction with CdS [7]. CIGS and CdTe have favorable material properites for solar cells, but both both contain rare constituent elements like tellurium and indium. All three commercial solar materials have reached power conversion efficiencies over 20% in lab tested champion cells. Cu_2O potentially addresses the disadvangtages of each of these materials, detailed discussion of which follows.

1.2 Motivation for Cu_2O: The Abundance of Common Elements for Photovoltaics

The problem that earth-abundant photovoltaics primarily addresses is that the component elements of current commercial photovoltaic thin film technologies (CIGS and CdTe) are not present in sufficient quantities in the lithosphere to make large scale production of these materials economical. CIGS and CdTe contain elements like tellurium and indium that are among the rarest elements in the earth's crust. Figure 1.1 plots the abundance of elements in the earth's crust, with the elements used in

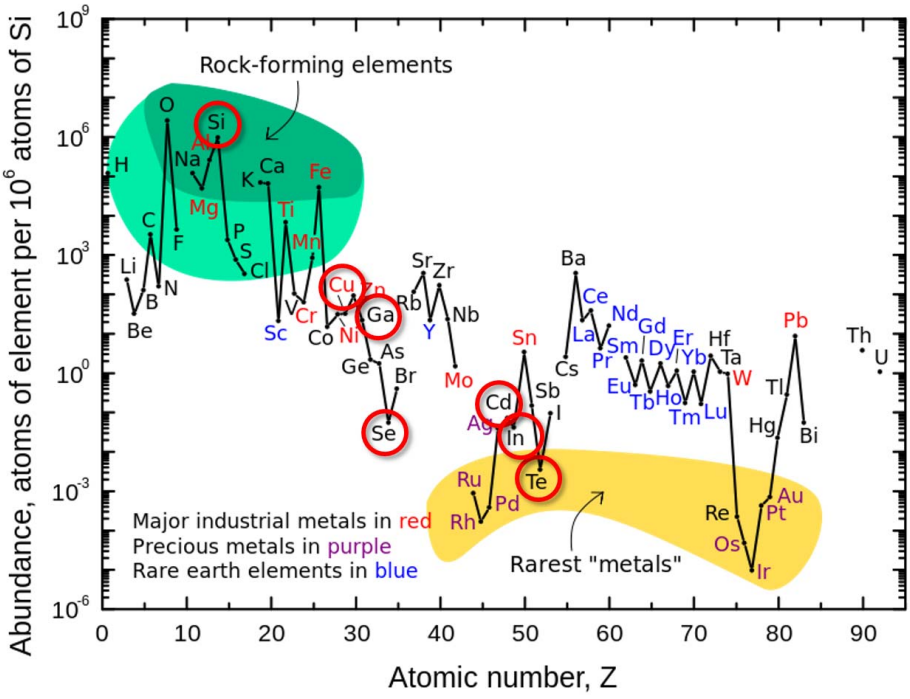

Figure 1.1: Comparison of elemental abundance in the lithosphere in parts per million. Constituent elements of photovoltaic absorbers are marked in red. Data is shown in appendix B.

commercial solar absorbers marked in red. Data for the plot was provided by minerals.usgs.gov [4]. Copper and oxygen are also marked on the figure and are much more abundant then elements like tellurium, indium, cadmium, and selenium. Silicon, the most widely deployed photovoltaic absorber, is also very abundant. The question then becomes how rare is too rare?

First lets estimate how much energy the US would need if we relied solely on photovoltaics for energy production. In 2013 the US consumed about 97.6 quadrillion BTU in total energy according to the U.S. Energy Information Administration [3]. 39.2 quadrillion of that was used to make 14.7 quadrillion BTU of electricity, with a conversion loss of 24.5 quadrillion BTU. Since photovoltaics has no conversion loss we can disregard 24.5 quadrillion BTU. Transportation also consumes 27 quadrillion BTU, primarily in petroleum. Again, there is a large transfer loss in an internal combustion car engine can be very large (an optimistic estimate is 65%), while the

transfer loss in an electric car is much smaller, at around 12% [57]. Thus, if energy for transportation were derived primarily from photovoltaics, we would estimate we would need about 9.2 quadrillion BTU for transportation. Thus a rough estimate of the total energy we would need to produce from photovoltaics in order for them to be the primary power source in the US based on 2013 consumption levels is about 55.3 quadrillion BTU.

We calculated the approximate volume of material we would need to produce 55.3 quadrillion BTU of energy every year solely from photovoltaics. In order to estimate the area the solar panels would need to cover, we used maps of the annual photovoltaic solar resource for the United States. The map for flat plate tilted panels is reproduced in Figure 1.2 . The quantity of solar energy varies from 4-7 kWh/m^2/day across the United States. We choose the intermediate value of 5.5 kWh/m^2/day to represent the solar power incident on the panel. We also assumed the panels employed have a solar conversion efficiency of 20%. The calculation of the area needed is summarized below:

$$\frac{(55.3\ \text{Quadrillion Btu})}{(5.5\,\text{kWh/m}^2\text{day})\,(20\%\,\text{Energy Conversion Efficiency})\,(365\ \text{Days})} = 40,366\,\text{km}^2$$

This is equivalent to 0.5% of the total land area of the continental United States.

Now in order to estimate the volume of material used we assumed the absorber layer was 1 micron thick (except for silicon, which we assumed was 100 microns thick), and the density of the absorber material was 10 g/cm^3, giving us a material mass of

$$\left(40,366\,\text{km}^2\right)(1\,\mu\text{m})\,(10\,\text{g/cm}^3) = 4 * 10^5\,\text{metric tons}$$

In order to compare this number to production, we have listed the production numbers for the constituent elements in Table 1.1 . The first column lists the primary commodity. The less abundant elements are not cost effective to individually mine and are instead the byproduct of mining for the listed primary commodity. This is important primarily because it means mining of these materials cannot be scaled

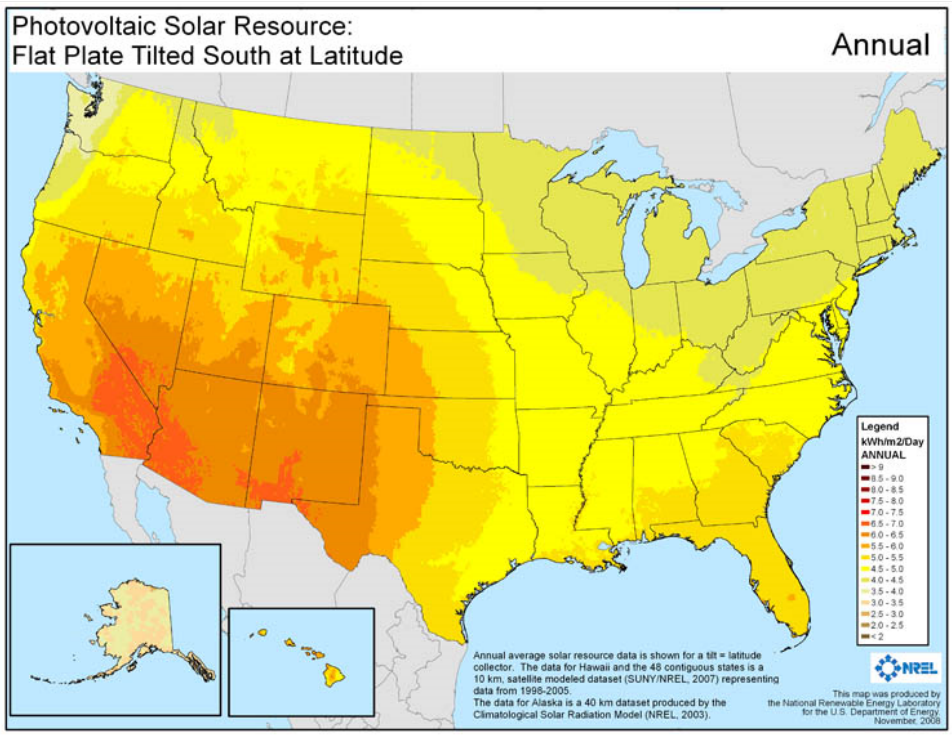

Figure 1.2: The photovoltaic solar resource for flat panels that are tilted southward according to the optimal angle for the given latitude. This map was produced by the National Renewable Energy Laboratory.

Element	Primary Commodity	World Wide Production (metric tons)	Time to produce $4*10^5$ metric tons
Copper	-	16,900,000	9 days
Cadmium	Zinc	20,900	19 years
Tellurium	Copper	500	800 years
Indium	Zinc	780	513 years
Gallium	Aluminum, Zinc	273	1466 years
Selenium	Copper	3,000	133 years
Zinc	-	12,800,000	12 days
Silicon	-	7,770,000	5 years

Table 1.1: Worldwide production numbers for the constituent elements of common photovoltaic materials as well as copper and zinc. Data was provided by minerals.usgs.gov. The rarer elements are not mined individually, and production is instead the result of mining other primary commodities, which are listed in the second column. Copper, zinc, and silicon are all primary commodities.

since production relies on the demand for the primary commodity. Thus we can assume that these production numbers are fairly independent of demand. In the final column of Table 1.1 we have calculated the time it would take to mine $4*10^5$ metric tons of material. It would take nearly a thousand years at current production rates to mine sufficient tellurium for CdTe, or sufficient gallium for CIGS. However, copper and silicon are much more abundant and widely produced, with the additional flexibility of being primary mining commodities. The quantity needed for large scale production would be a fraction of what is currently produced. Thus there is a need for earth-abundant semiconductors like Cu_2O and silicon because production of rarer elements likely is too limited to reach power generation levels necessary to meet most of the United States energy demand.

1.3 Motivation for Cu_2O: Detailed Balance Calculations for Single and Dual Junctions

One of the reasons we study Cu_2O is that it has a theoretical power conversion efficiency limit of around 25%, though its demonstrated efficiency is not very high at 5.38 %. Detailed balance calculations are used to assess the thermodynamic limit of photovoltaic device efficiency based on the material's optical properties. We will explore both single and dual junction calculations below

1.3.1 Single Junction Calculations for Cu_2O

Single junction detailed balance calculations are an incredibly straightforward affair. All that needs to be known is the band gap of the material in question [52]. However, naming a single band gap value for Cu_2O is particularly complicated due to the number of easily accessed energy transitions, including a large difference between the material's optical and electronic band gap. Cu_2O has an electronic band gap of 2.1 eV, but an optical band gap of 1.9 eV [10]. We measured the optical band gap ourselves using several methods and found it to have a value of 1.9 eV. We also determined

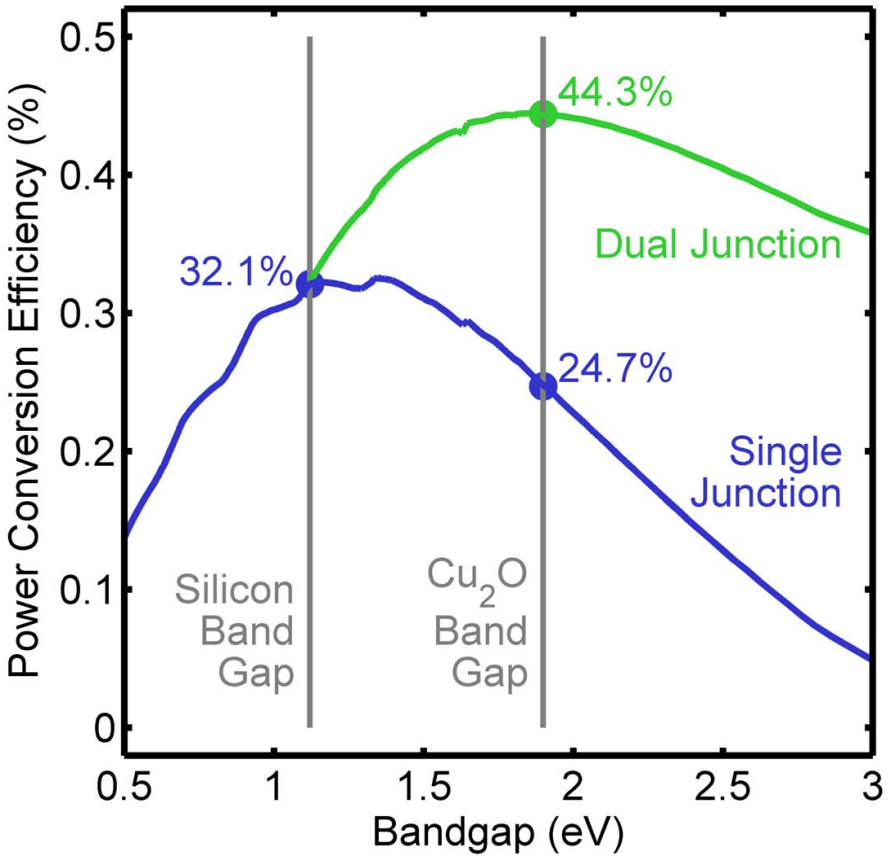

Figure 1.3: Detailed balance calculations for both single photovoltaics junctions (blue line) and dual junctions with a silicon bottom cell (green line) are shown above. The band gaps for silicon and Cu_2O as well as the efficiencies for the two absorbing layers are indicated. Dual junctions reduce energy conversion losses due to thermalisation and thus have larger theoretical efficiencies. The dual junction calculations are made for an independently connected device, meaning that we assume the current from the individual junctions will be inverted before the circuits come together, thus power addition is lossless.

that the optical band gap is the most meaningful transition for Cu_2O photovoltaic devices. The experiments done to reach these conclusions are detailed in the following chapter.

Once a band gap has been selected, theoretical J-V curves can be constructed by balancing absorption emission to determine collected current at different voltages. The process is exhaustively detailed elsewhere [1, 20, 24, 41, 52]. Calculations of theoretical efficiency for single devices using the AM 1.5 G spectrum are easily performed and are shown in Figure 1.3 [1, 24, 41]. We calculate that a 1.9 eV band gap will have a theoretical power conversion efficiency limit of 24.7%.

1.3.2 Modeling a Cu_2O Dual Junction with Silicon

One of the largest sources of loss during power conversion from photons to electrons in a solar cell is thermalisation of the photoexcited electron-hole pair [20]. This occurs when the absorbed photon has more energy then the band gap. The lifetime of electrons above the valence band edge is vanishingly small, and the excited carrier quickly decays to the band edge. One way to combat this power conversion loss is by using multiple p-n junctions stacked on top of one another. The top junction must be composed of wider band gap materials, and will absorb the high energy photons. The below gap energy photons travel through the top junction, and can be absorbed by the second, lower band gap junction below. The two junctions only absorb light nearer to their own band gaps, reducing thermalisation loss.

Cu_2O has a wide band gap compared to the solar spectrum, making it a suitable material for a top cell. It can be paired with materials with materilas with narrower band gaps, like silicon at 1.12 eV [55]. Calculations of device efficiency for a dual junction with a silicon bottom cell and various band gap top cells are shown as the green line Figure 1.3. Cu_2O has an ideal band gap for a top cell, and the device would have a theoretical energy conversion limit of 44.3 %. Thus we believe that Cu_2O is a worthy material for study not because it could possibly compete with silicon, but because it could be incorporated into a silicon module.

To expand on the details of the dual junction detailed balance calculation, tandem cells are often electrically connected in series due to the ease of monolithic manufacture versus the seemingly more complicated structure of a 4-terminal cell. Though this type of electrical connection is often easy to fabricate, especially if the top cell is a thin film, it requires that both cells operate at the same current. Thus due to current restrictions in series connected cells, high efficiencies are only achieved for an ideal AM 1.5 G spectrum. Because the real solar spectrum module will encounter in the field will vary widely day to day and hour to hour due to cloud coverage and varying incidence angles, a device which is only efficient for a certain spectrum is impractical [1]. An alternative device design is independent connections, in this case the individual cells are electrically connected in parallel rather than in series. The DC current in the independent circuits is then independently inverted before the circuits are brought together. Because AC current can be added together with no significant loss of power, the device is much less sensitive to the exact power distribution in the incident solar spectrum. Calculations shown are for independently connected cells.

1.4 Contents of the Thesis

This thesis describes the study of the Zn-VI/Cu_2O interface primarily for increasing the voltage of Cu_2O photovoltaic devices. The chapters are summarized as follows:

- Chapter 2 describes the synthesis of Cu_2O wafers from copper foils and their resulting physical properties. We review the details of the thermal oxidation process that is used to produce Cu_2O and we also review the optical, electronic, and structural data we have for Cu_2O. For example, we determine the optical band gap of Cu_2O is 1.9 eV based on photoluminescence, external quantum efficiency, and absorption measurements.

- Chapter 3 reviews growth and analysis of the various Zn-VI materials we analyze as heterojunction partners, including ZnO, ZnS, ZnSe, Zn(O,S), and Zn(S,SO_4). The films are primarily grown by sputtering and MBE and are characterized

by X-ray diffraction, X-ray photoelectron spectroscopy, transmission, reflection, and ellipsometry.

- Chapter 4 describes the surface composition of Cu_2O wafers as well as an introduction to a novel interface formation technique. Our results suggest an interesting mechanism by which the CuO surface layer on a Cu_2O wafer reacts with the deposited ZnO thin film according to the ratio of Zn:O in the deposition ambient. We demonstrate the ability to reproducibly tune the interface from O-rich, to stoichiometric, to Cu-rich solely by modifying the ratio of Zn:O in the growth atmosphere. We also study the reaction chemistry of ZnSe, ZnS, and Zn(O,S) with Cu_2O.

- Chapter 5 reviews the valence band offset measurements performed by XPS using the Kraut method. In this case we find that the surface stoichiometry alters the band alignment between ZnO and Cu_2O, which helps resolve the cause of the variation in band offset reported in Cu_2O literature. Additionally we find that the band offset measurements suggest ZnSe and Zn(O,S) as heterojunction partners.

- Chapter 6 contains an overview of the photovoltaics devices we analyzed. We are primarily concerned with methods to improve the open-circuit voltage of devices and focus on methods to improve the voltage. We find that maintaining a stoichiometric surface is essential to reaching the voltage entitlement defined by the work function difference between the two heterojunction partners in ZnO/Cu_2O devices. We then find that the open-circuit voltage of the devices could be tuned upward with the addition of sulfur, as implied by the valence band offset measurements.

- Chapter 7 is an overview and path forward for Cu_2O research.

Chapter 2

Synthesis of Cu_2O Wafers

Cuprous oxide (Cu_2O) is unique semiconductor due in part to its straightforward synthesis process. We make crystalline wafers of Cu_2O directly from Cu foils in a vacuum free route. The wafers are simply heated under a nitrogen purge, annealed in an oxygen dilution or even in air, and then cooled under a nitrogen purge. This ease of manufacture gives Cu_2O the capability for high-speed, scalable production.

In this chapter I will describe our procedure for making Cu_2O wafers in depth, as well as some of material properties that make Cu_2O an ideal photovoltaic material. I will also describe our procedure for making 20 µm thick bulk Cu_2O wafers with lateral dimensions on the order of 1 cm^2.

2.1 The Phase Diagram of Cu_2O

The pressure-temperature phase diagram of Cu_2O is displayed in Figure 2.1. This phase diagram was compiled by Xue et. al. [69]. after a meta-analysis of several explorations of the Cu-O phase diagram, as well as their own research into the high temperature, high pressure region. There are many versions of the phase diagram available, but this is regarded as the most accurate version presently [10]. The equations for the lines in Figure 2.1 are taken directly from this reference.

The thermodynamically stable phases of on the Cu-O phase diagram are Cu, Cu_2O, and CuO. There are other reported metastable phases, but as we are not using a growth method in which kinetic concerns can trump thermodynamics, we are not concerned with these other phases [63]. As can be seen in the diagram, Cu_2O is the high temperature phase, and it has wide stability region in both temperature and O_2 partial pressure, making production of phase pure Cu_2O straightforward. The stability region of Cu_2O overlaps with the partial pressure of O_2 in air at room temperature and pressure, which allows Cu_2O to be produced by oxidation in air. CuO is the stable phase at room temperature and pressure, and it will form on the surface of Cu_2O after air exposure. The oxidation of the surface of air-exposed Cu_2O wafers is characterized in the next chapter.

Despite Cu_2O not being thermodynamically stable at room temperature and pressure, studies have shown that it is kinetically stable up to approximately 200 °C [30]. This is suitable for photovoltaic applications.

2.2 Furnace Set-up and Growth Procedure

A schematic of the furnace used in this study is outlined in Figure . We used a 1500 °C furnace from MTI with a 2" diameter quartz tube. A stainless steel quartz to KF 40 flange was used on the end of the tube to simplify attachment of gas lines for the nitrogen purge. The furnace was calibrated using a K-type thermocouple feed through in vacuum, and we found that the temperature of the furnace was around 50

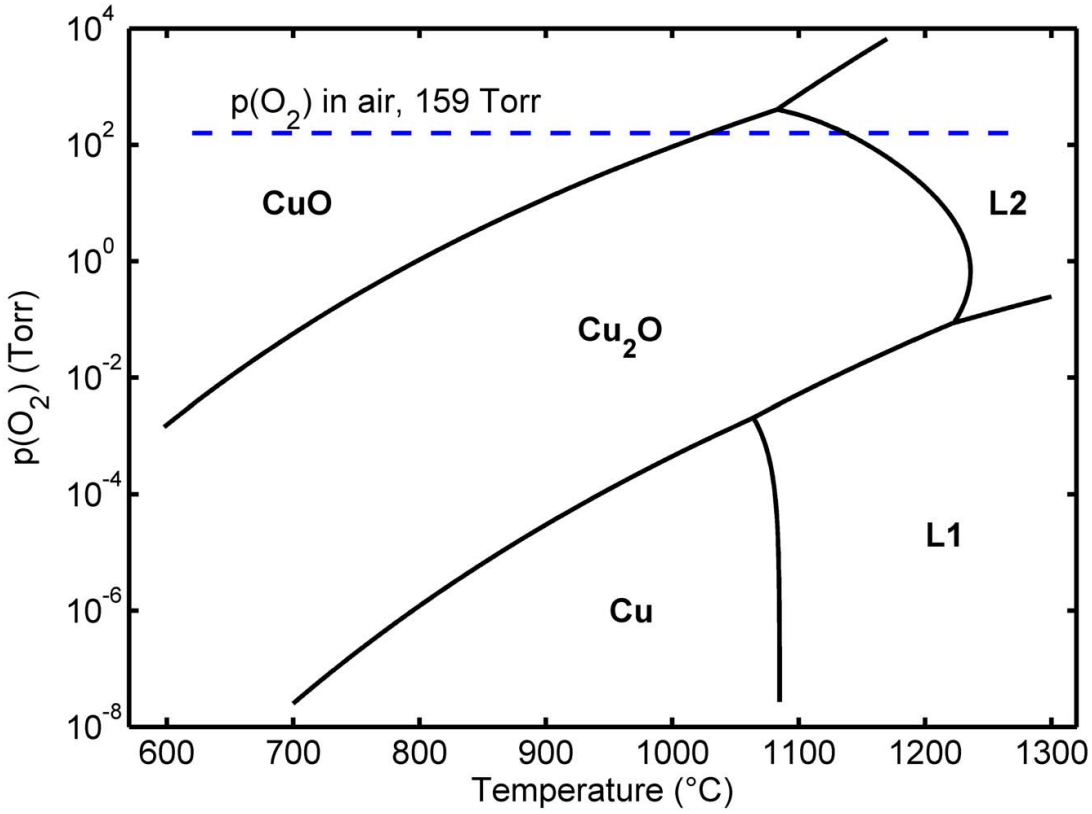

Figure 2.1: The pressure-temperature diagram for the Cu-O system. We are interested in the high temperature oxide phase, Cu_2O. The pressure of O_2 in the atmosphere is indicated by the blue line. The equations for the lines in the graph above are taken directly from Reference [69].

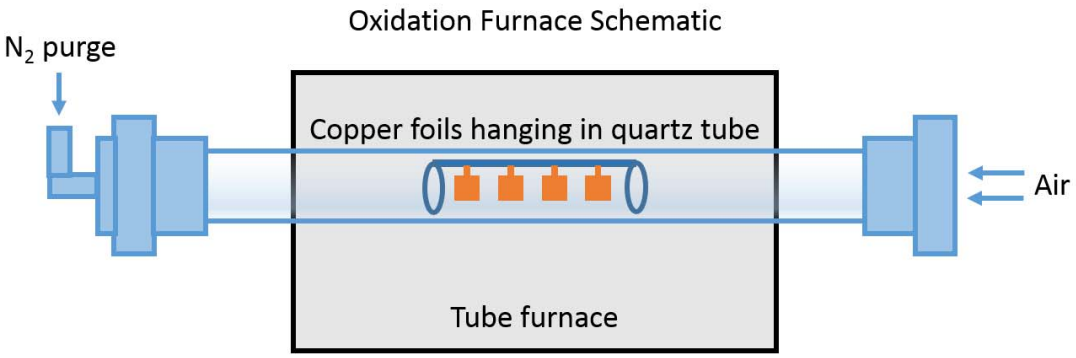

Figure 2.2: Schematic of furnace setup for the copper foil oxidation. The remarkably easy growth procedure is one of the benefits of Cu_2O over other solar materials. We hang the Cu foils from a quartz apparatus, as shown in Figure 2.3. The oxidation is performed in a horizontal tube furnace with a nitrogen purge at one end and the other end open to air. When heating and cooling the foils, the tube is purged with nitrogen. Air is used as the oxygen source, thus to begin oxidation the nitrogen is turned off allowing air to diffuse into the tube from the open end.

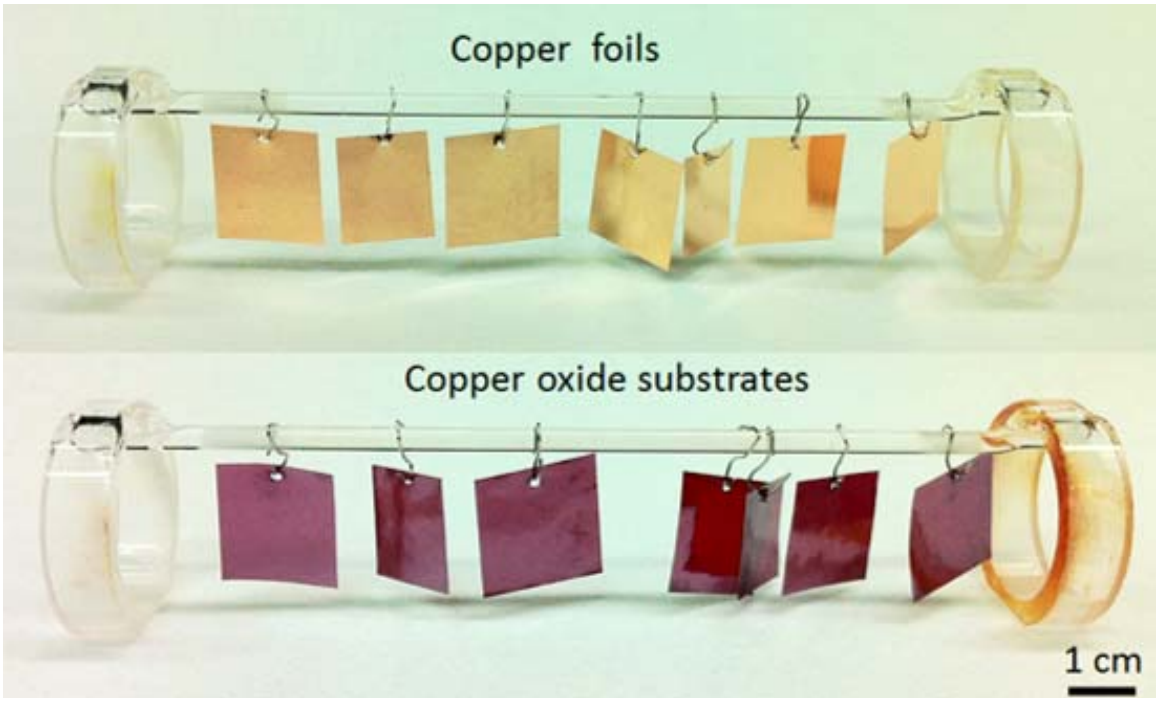

Figure 2.3: Image of Cu foils cut to approximately 4 cm^2 (above) and hung on a quartz rod in preparation for oxidation. After an oxidation the Cu_2O wafers (below) are removed from the furnace still attached to the quartz rod.

°C hotter than indicated throughout the temperature range of interest. All reported temperatures take this offset into account and reflect the actual temperature of the samples. The tube was purged with a 2 scfh nitrogen flow. At the other end of the tube, a KF flange with a 3 mm diameter hole was used to restrict the opening of the tube to prevent ingress of dust into the tube during oxidation.

The experimental details such as anneal temperature and time varied somewhat from run to run, but the basic form of the oxidation was always the same. Most experiments were performed with Cu_2O made from 500 µm copper foil. The copper foil was cut into 2 cm x 2 cm squares using a sheet metal cutter. 1/32" diameter holes were then punched into the Cu using a sheet metal punch. Copper wire was used to hang the foils from a quartz hangar. Both the copper wire and foils were 99.9999% pure and were purchased from Alfa Aesar. A picture of the hanging copper foils and the Cu_2O wafers after oxidation can be seen in Figure 2.3. This image shows that

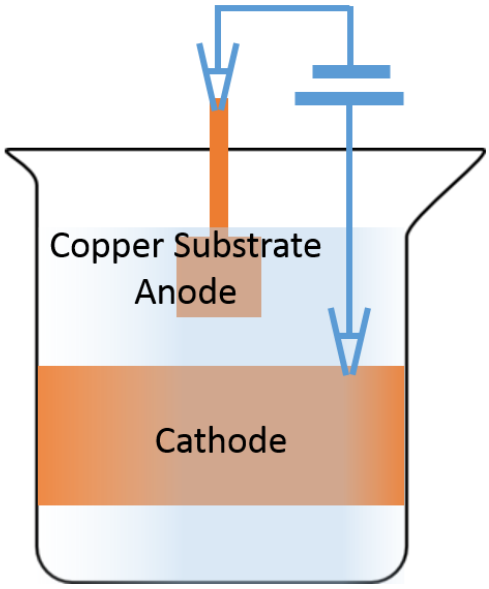

Figure 2.4: The configuration used for electropolishing. The copper sample, which served as the anode, is suspended in the polishing solution by copper wire. A second, larger copper foil lines the walls of the beaker to act as the cathode. A voltage of 4.8 V was placed across the two samples for 100 s to complete the etch.

oxidized Cu_2O wafers will take on the shape of the original copper foil.

The copper needed to be cleaned before oxidation to remove surface contamination from the cutting process. The was done most basically by rinsing the samples in isopropanol and the blowing them dry with nitrogen. An electropolishing procedure was also sometimes used to clean the foils. The recipe is as follows:

1. The electropolishing solution is prepared by mixing 500 mL deionized water, 250 mL orthophosphoric acid, 250 mL ethanol, 10 mL isopropanol, and 5 g urea and then stirring for at least 2 hours while covered

2. The solution is then transferred to a beaker lined with copper foil, which serves as the cathode. The sample, which serves as the anode, is suspended in the solution. This is illustrated in Figure 2.4.

3. Electropolishing is performed at 4.8 V for 100 s. The solution is continuously stirred to keep the etch rate consistent.

4. The samples are then removed from the solution and sonicated in acetone for 3 hours.

Once the copper was clean, it was ready to be oxidized. The copper foils were hung on on the quartz hanger, as described above, and loaded into the furnace. The quartz tube was purged with N_2 for 30 minutes to remove all air from the tube. After 30 minitues the tube was ramped up to 1025 °C over 50 minutes. The copper was annealed in N_2 at 1025 °C for 1 hour. The N_2 purge was then switched off and air was allowed to diffuse into the tube. The samples were annealed in air for 18 hours. The N_2 was then switched back on and the samples were annealed in N_2 for 5 hours before the temperature was ramped down to room temperature over about 6 hours. The samples were allowed to cool all the way to room temperature before they were removed from the furnace.

2.3 Characterization of Cu_2O Foils

The structural, optical, and electronic properties of the Cu_2O wafers were characterized using several methods, which are detailed below.

2.3.1 Structural Characterization

Cu_2O foils were found to be phase pure by the X-ray diffraction (XRD) pattern, shown in Figure 2.5 . All peaks can be indexed to Cu_2O, with no evidence of bulk Cu or CuO formation [54]. There was evidence of a small amount of CuO formation on the surface of the wafers, as Cu_2O is not the stable phase of copper oxide at room temperature and pressure [69]. Detailed analysis of the surface of the wafers can be found in Chapter 3.

An optical microscope was used to image the surface of the Cu_2O and the micrographs are shown in Figures 2.6 and 2.7. The images show lateral grain sizes were of several hundred microns. Grain size could be increased by either increasing anneal time or electropolishing the copper foils before oxidation. An optical micro-

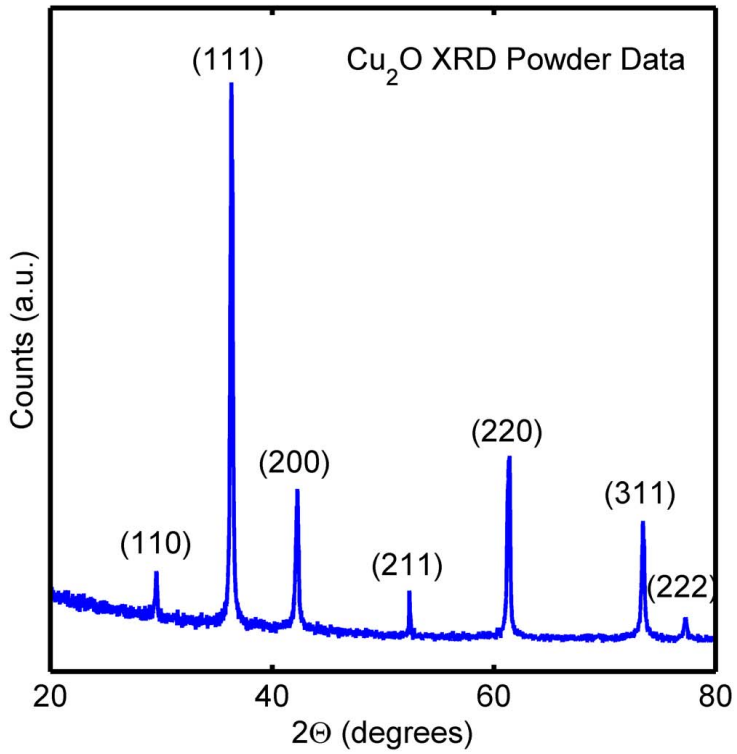

Figure 2.5: X-ray diffraction pattern of thermally oxidized Cu_2O that has subsequently been powdered. Sample is phase pure, as all peaks can be indexed to Cu_2O.

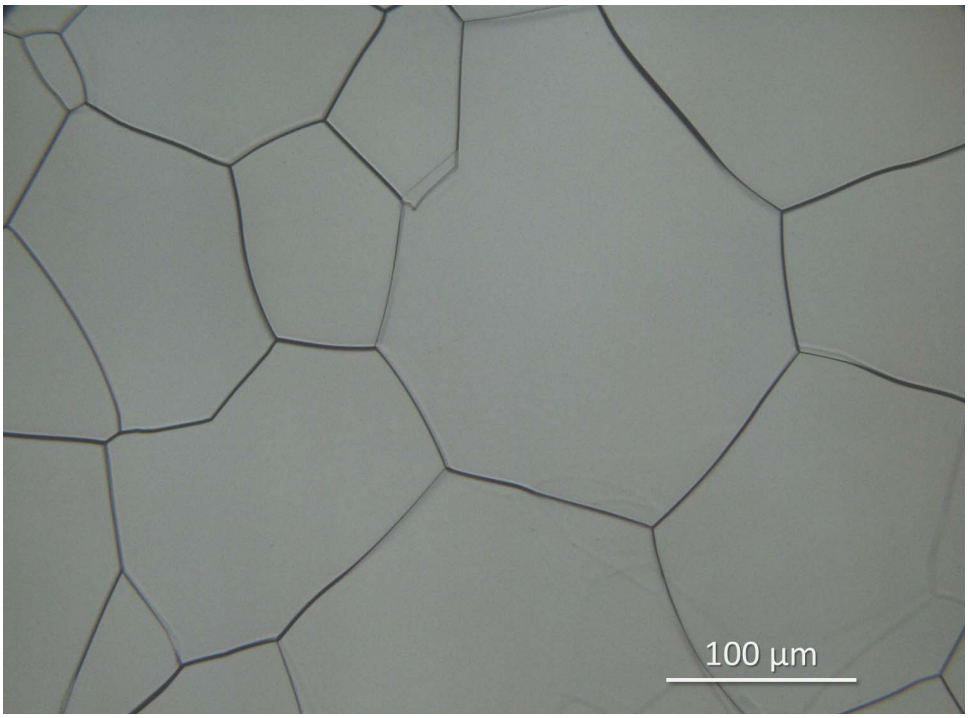

Figure 2.6: Optical microscope image of Cu_2O made from an unpolished copper foil. Lateral grain size is on the order of hundreds of microns.

scope image of a Cu_2O wafer made from electropolished copper is shown in Figure 2.7. The lateral grain size increased to close to 1 mm. The increase in grain size with electropolishing probably means that grain size is limited by the heterogeneous nucleation of grains on surface defects. When we electropolish the sample, we remove mechanical and chemical defects that can serve as low barrier nucleation points. When less grains nucleate, the grains are allowed the grow larger. Annealing works to increase grain size by allowing grains to sinter together. Increasing annealing time to 48 hours increased the grain size to nearly 1 cm. However, it was found that the Cu_2O electrical properties were fairly independent of grain size, and thus long anneals and electropolishing proved unnecessary to device performance.

2.3.2 Optical Characterization

The band gap of Cu_2O reported in literature can vary widely, with values ranging from 1.5-2.5 eV. [19, 42, 48, 60] However, the values of the both the electronic and

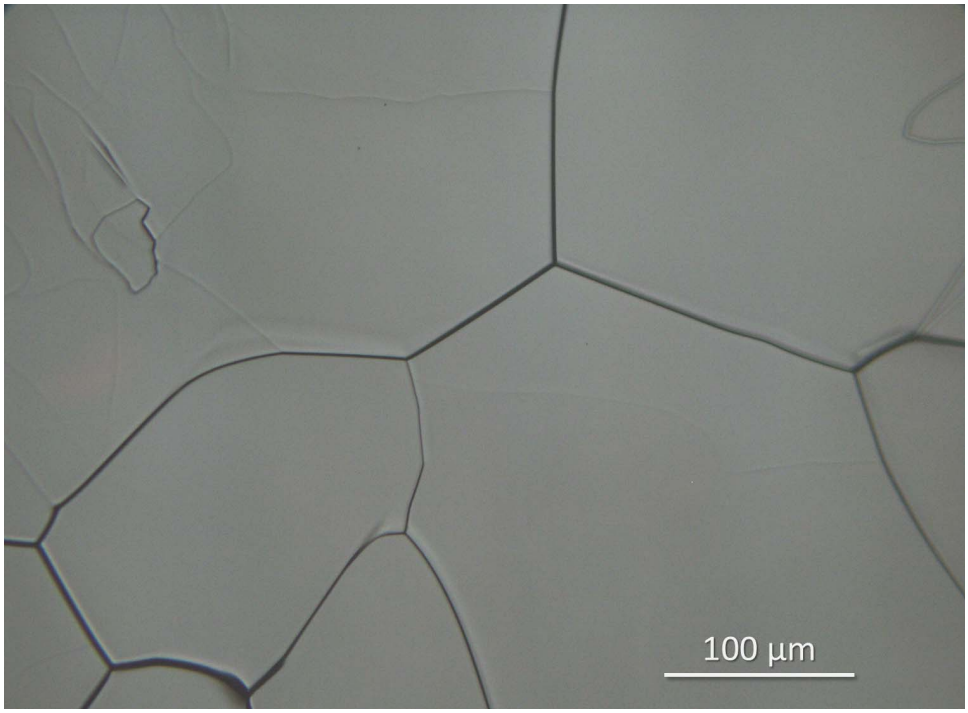

Figure 2.7: Optical microscope image of Cu_2O made from an electropolished copper foil. Lateral grain size is on the order of hundreds of microns, and grains are larger than the unpolished sample.

optical band gap are actually well known. There is a direct electronic band gap at 2.5 eV, a direct-forbidden electronic band gap at 2.1 eV, and the optical band gap is at 1.9 eV [10]. Much of the variance in reported band gap is due to the difficulty of making phase pure Cu_2O without inclusions of CuO. CuO has a smaller band gap, around 1.2 eV, and thus the reported values on the smaller end of the spectrum are probably due to CuO inclusions [64]. Additionally, the extinction coefficient of Cu_2O near the band gap is small because the valence band and conduction bands have the same parity. Direct transitions at 2.1 eV are not allowed, thus all absorption into the band gap is indirect [10]. Direct absorption occurs around 2.5 eV, thus the higher reported values are often due to mistakenly identifying the direct transition as the band gap. Additionally, Cu_2O has a large difference between the optical band gap and the electronic band gap, where the optical band gap is defined as the electronic band gap minus the exciton binding energy. The exciton binding energy for Cu_2O is approximately 200 eV due to the small dielectric constant of Cu_2, which is ~7 [10]. Thus optoelectronically Cu_2O is more similar to an organic, molecular material than to most solid state semiconductors. Photons may be absorbed by the optical band gap, further complicating measurements of the optical characteristic.

We analyzed the optical properties of Cu_2O using a variety of techniques, including ellipsometry, absorption, photoluminescence, and external quantum efficiency. We measured the real and imaginary parts of the refractive index (n and k) by spectroscopic ellipsometry on a bulk Cu_2O wafer. The data is shown in Figure 2.8. The transition from absorption into a direct forbidden transition to absorption into an allowed direct transition is evident in the large increase in the extinction coefficient around 2.5 eV (500 nm). If we assume the bulk wafer we used is infinitely thick, then the n and k data can be calculated directly from the delta and epsilon parameters measured by ellipsometry. We can verify this assumption by analyzing the n and k data that were calculated from the ellipsometry data. The absorption coefficient at 640 nm is 0.001952. Using the Beer-Lambert law we see that 99% of light with a wavelength of 640 nm will be absorbed at a thickness 120.15 µm. Thus the assumption that 800 µm of Cu_2O is essentially infinite in an optics measurement is a good

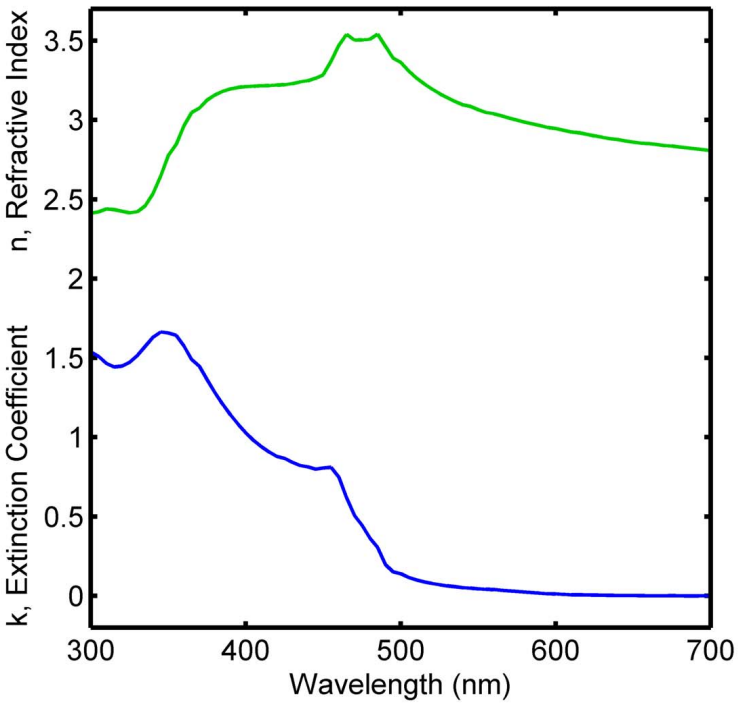

Figure 2.8: The real and imaginary parts of the refractive index were directly calculated from ellipsometry measurements on polished Cu_2O wafers. The beginning of direct allowed absorption at 500 nm (2.5 eV) is clearly visible in the extinction coefficient.

assumption. As a side note, the test sample was a polished Cu_2O wafer. Wafers were polished for a limited number of experiments using a series of alumina and diamond polishing discs provided by South Bay Technologies. Polishing the surface was necessary to reduce scattering of the ellipsometer light source from the surface.

The band gap can be derived from a Tauc plot built using the extinction coefficient, but this is a relatively imprecise method that is only accurate for films of infinite optical thickness. Films this thick are impractical to manufacture. Some of the variance in reported band gap is also surely due to the difficulty in making an accurate assessment of the band gap from a Tauc plot. Tauc plots will be discussed in more detail in Chapter 3. We are working with bulk wafers that we proved above are infinitely thick to absorption, thus we should be able to see the absorption cutoff from the raw transmission data. Transmission data was collected by a Cary 5000

UV-Vis-NIR spectrophotometer with an integrating sphere to capture diffuse light. The transmission data is the red line shown in Figure 2.9. The absorption cutoff at 640 nm, or 1.9 eV, is very clear. Thus the optical band gap, and not the electronic band gap, limits absorption.

We also performed a steady-state photoluminescence (PL) measurement on a bulk wafer, which is shown as the black line in Figure 2.9. The steady-state PL excitation was performed using the 488 nm line from an Ar-ion laser that was chopped at 10 kHz using an acuosto-optic modulator. The emission was passed through a monochromator and focused onto an infrared photomultiplier tube, and the PL signal was monitored using a lock-in amplifier. The Cu_2O used was unpolished and untreated, or as-grown. There is an emission peak from the sample at 1.9 eV, also where absorption cuts off, which is another indicator that we are looking at the optical band gap.

The blue line in the Figure 2.9 is an external quantum efficiency measurement. The sample used in this measurement was a ZnO/Cu_2O photovoltaic device. The details of the manufacture of this device are in Chapter 6. For this measurement the ZnO/Cu_2O device is exposed to light of different wavelengths and the collection efficiency of photoexcited carriers at each wavelength is measured. Similarly to the photoluminescence measurement, the light source is chopped before the sample, and the collected signal is separated from stray thermal generation by a lock-in amplifier. This is really the most important optical experiment for devices, because it tells us not just whether or not a photon is absorbed, but also the number of electron hole pairs collected per wavelength. The signal for this measurement also terminates at approximately 1.9 eV.

We would expect emission and absorption to cut off at the optical rather than the electronic band gap, and that is indeed what we see. What's more notable is that carrier collection in the external quantum efficiency data proceeds to the optical band gap as well. This effect is related to Cu_2O's large exciton binding energy giving the excitons a long lifetime at room temperature [10]. Additionally, based on this spectral response data (which is very typical of Cu_2O spectral response data [11]) excitons are

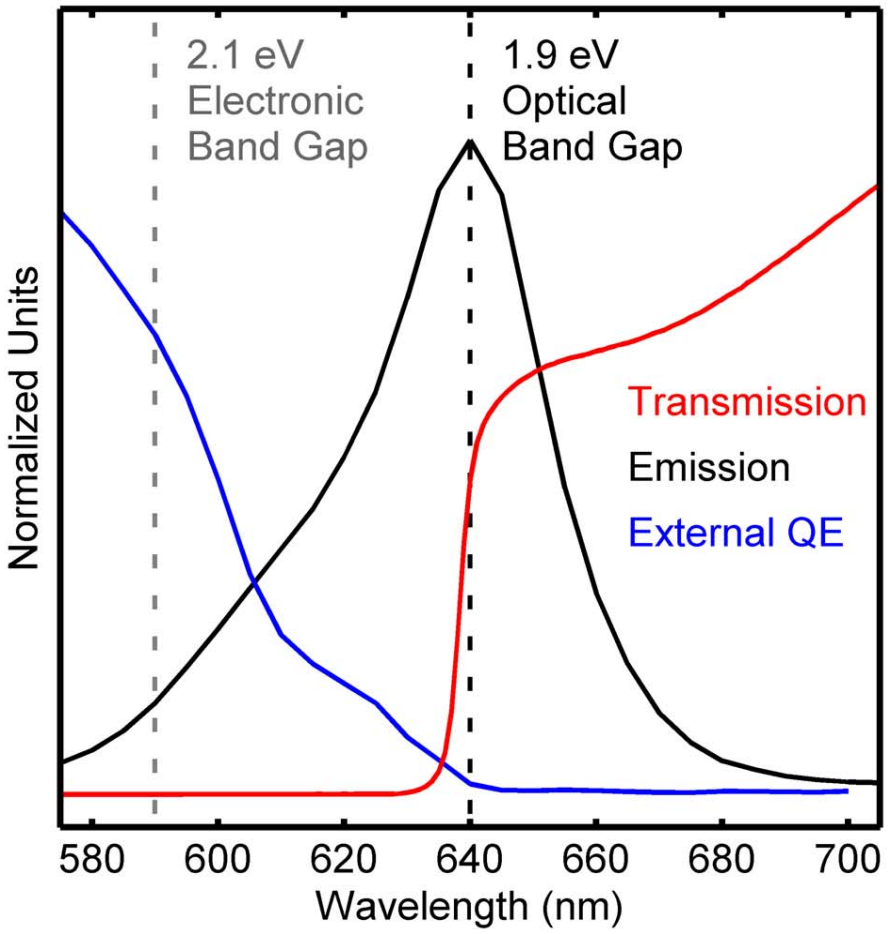

Figure 2.9: Data from three different methods for measuring the band gap are combined onto one plot. All data is normalized to fit onto the same y-scale. The red line is transmission through an 800 µm thick Cu_2O wafer. The black line is photoluminescence from a similar wafer. The blue line is spectral response data from a ZnO/Cu_2O heterojunction. The combined methods all indicate an absorption edge at 1.9 eV, or about 640 nm.

collected at Cu_2O heterojunctions. If the excitons are being collected then the optical band gap must be treated as the voltage limit in Cu_2O cells. Thus in all detailed balance calculations, which really are optical calculations as they solely deal with emission and absorption, I have used 1.9 eV as opposed to the more traditional value of 2.1 eV because of the unique role that excitons play in Cu_2O photovoltaic devices. From here on out I will also simplify my notation by referring to the optical band gap of Cu_2O simply as its band gap.

2.3.3 Electrical Characterization

Electronic properties were determined by Hall coefficient measurements at room temperature. The Cu_2O wafers typically had carrier concentrations on the order of 10^{13} cm^{-3} with a mobility of 100 $cm^2V^{-1}s^{-1}$. These values are in line with previously reported carrier concentrations and mobility data [10, 42, 48].

These electronic properties were also verified by X-ray photoelectron spectroscopy (XPS) of the valence region of the wafers. Figure 2.10 shows the valence region of a Cu_2O wafer cleaved in situ. More details on the preparation of this sample are presented in Chapter 4. In XPS the sample is in equilibrium with the sample stage because they must be in electrical contact to prevent charging disturbing the measurement. This means the value of 0 binding energy is also the Fermi level of the material. Thus the valence band to Fermi level difference can be measured by XPS. As a side note, XPS is a surface sensitive technique, thus if there is band bending at the surface of the sample, the valence band the Fermi level split measured will not be the bulk value, but rather the surface value. The method we used to extract the data on the Fermi level position in the band gap is visualized in the inset in Figure 2.10. We fit lines both to the leading edge of the valence band and to the baseline of the data. The binding energy that the two lines intersect at is also the valence band to Fermi level split. We obtained a value of E_F-E_V= 0.32 eV from analysis of the Cu_2O wafer.

We also calculated what we would theoretically expect the difference in valence

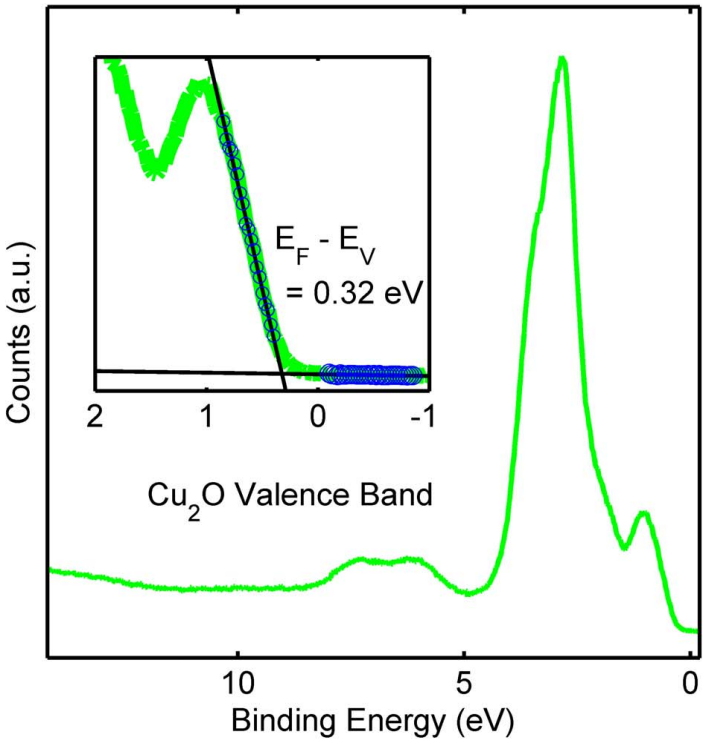

Figure 2.10: High-resolution X-ray photoelectron spectroscopy data of valence band of Cu_2O is shown above. The sample must be in good electronic contact with the stage to prevent charging from the loss of photoexcited electrons. This also means the Fermi level sits at 0 binding energy. Thus the edge of the valence band in XPS can be used to find the difference between the valence band and the Fermi level at the surface of a sample. We calculate this by fitting a line to the leading edge of the valence band and to the baseline, as shown in the inset above. The intersection of the two fit lines is the valence band to Fermi level difference.

band and Fermi level to be given we know the carrier concentrations are between 10^{13} and 10^{14} from Hall measurements. The Fermi level to valence band split will be 0.3-0.4 eV given that $N_V(300\ K) = 1.11*10^{19}$ [10, 55]. This aligns nicely with the value measured by XPS.

2.3.4 Overview of Bulk Characterization

Using this very simple growth procedure, were we able to transform copper foils directly into phase pure Cu_2O wafers that had lateral grain sizes on the order of hundreds of microns. Furthermore, the large value for mobility, at 100 $cm^2V^{-1}s^{-1}$, indicates that the lifetime of carriers is adequate for producing efficient photovoltaic devices [55]. All of these values are also consistent with values previously reported for Cu_2O. Additionally, we thoroughly investigated the band gap of Cu_2O and believe that the optical band gap at 1.9 eV is the most significant energy level transition for calculating the thermodynamic limits of Cu_2O photovoltaic devices.

2.4 Growth of Thin, Bulk Wafers

Cu_2O devices are often limited by series resistance through the wafers, which we will detail in Chapter 6. Therefore we have also looked in to making very thin Cu_2O. We can synthesize Cu_2O with a thickness down to about 40 µm simply by following a similar procedure to that outlined above. The synthesized wafers are extremely fragile and can't be handled by tweezers until a significant amount of metal is deposited on them. They do become somewhat flexible, as is common in extremely thin, flat semiconductors. However, because the synthesized Cu_2O is not single crystalline, if too much force is applied to the wafer, it will fracture along the grain boundaries, which are points of decreased mechanical strength.

Oxidation of thinner Cu_2O by this route proved impossible, so another method was developed to allow for the synthesis of these very delicate wafers. This fabrication method is outlined photographically in Figure 2.11 . This method seeks to allow handling of the extremely delicate 20 µm wafers by using a built-in handle wafer

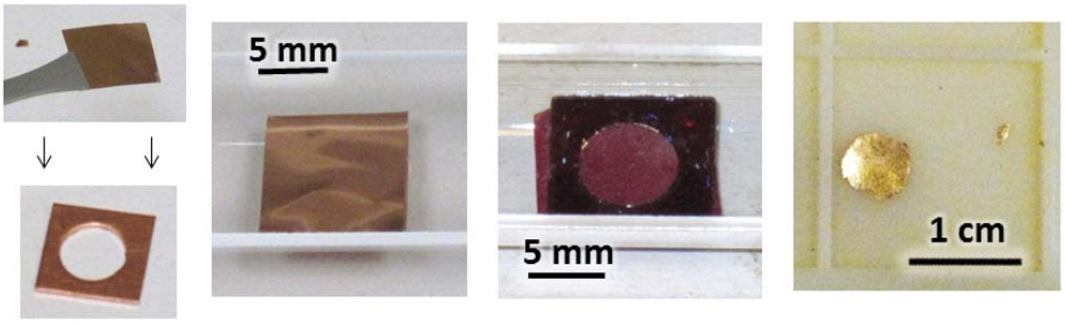

Figure 2.11: Photographic outline of method for fabricating ultra-thin Cu_2O wafers.

that can be reused. Cu_2O oxidizes not by the flux of oxygen into the copper foil, but rather by the diffusion of copper to the wafer's surface, due to the much larger diffusion coefficient of Cu in Cu_2O [70]. This leads to both the frequent formation of voids in the material and also the tendency of Cu_2O to fuse to whatever the copper foil is touching during oxidation [42]. We took advantage of the fact that Cu_2O fuses to what it is in contact with during oxidation by using this to fuse the very thin Cu_2O to thicker handle wafers. 2 mm thick copper wafers with 1 cm diameter holes drilled into them were oxidized in order to serve as handle wafers. The resulting Cu_2O wafers had an area of approximately 4 cm^2 with a 1 cm diameter hole through the middle. The top and bottom surface of the sample were lapped flat to allow the thin copper foils to lay in contact with the surface of the handle wafer.

12 µm thick copper foils that were 99.99% pure were purchased from ESPI for the experiment. These foils were cut to approximately 1.5 cm by 1.5 cm to completely cover the hole in the Cu_2O handle wafer, as shown in the first image in Figure 2.11. The thin copper foil and the thick Cu_2O handle wafer were then placed into the furnace as a stack shown in the second image in 2.11. The sample was usually balanced on an alumina or quartz boat. During oxidation the copper foil fused with the thicker Cu_2O handle wafer, leaving a thin film of Cu_2O that was approximately 20 µm thick, as shown in the third image in Figure 2.11. The thickness of the wafers was verified by scanning electron micrographs (SEM), which can be seen in Figure 2.12 . That image also shows the near formation of some pin holes in the film, especially at

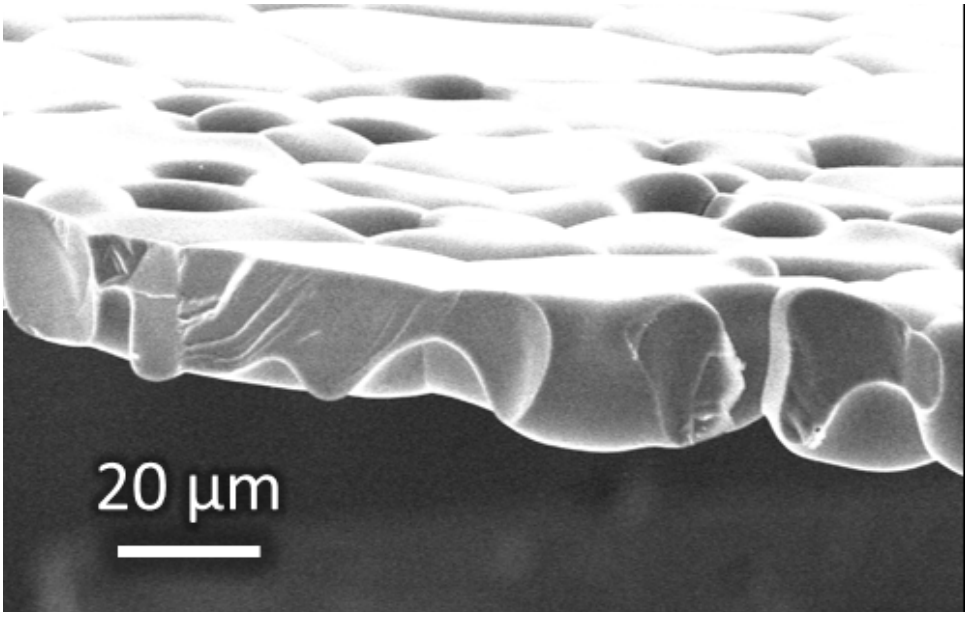

Figure 2.12: Scanning electron micrograph of cleaved edge of 20 µm thick wafer.

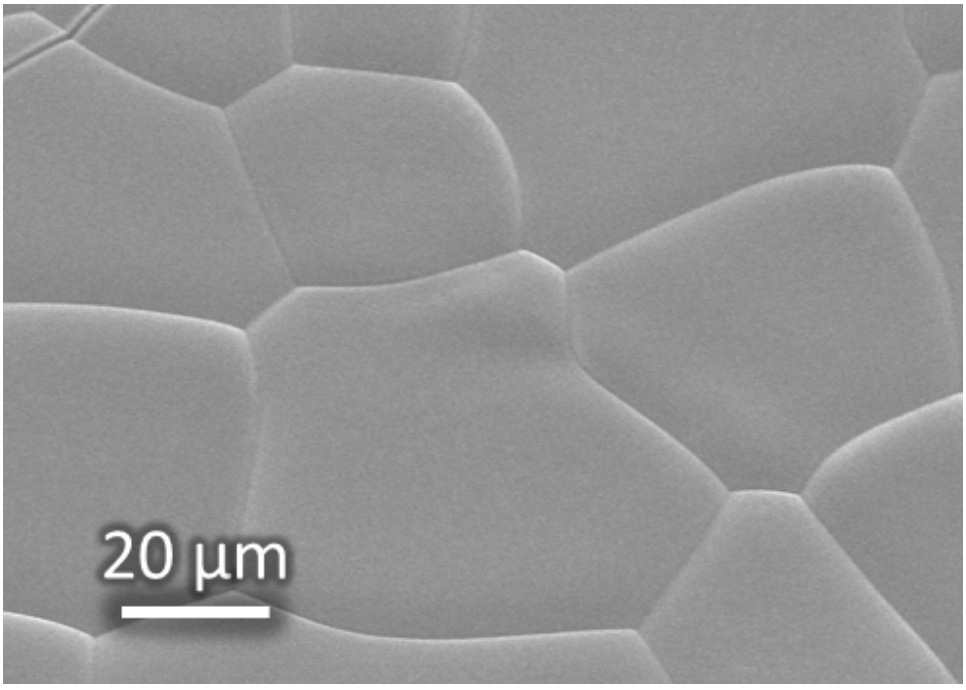

Figure 2.13: Another scanning electron micrograph of thin Cu_2O wafers showing the lateral grain structure. The grains are on the order of 50 µm wide.

the grain boundaries. Cu_2O is oxidized at temperatures where sublimation of Cu_2O is significant. We expect some amount of evaporation of material during growth, and it appears that it happens significantly from the grain boundaries. When making very thin wafers care must be taken with the oxidation procedures to ensure that oxidation time is limited to allow for full oxidation of the wafer, but is not so long that evaporation becomes significant.

The thin Cu_2O was also phase pure and had identical electronic properties to the thicker Cu_2O. The only structural difference was that the grains were much smaller and the surface was rougher. An optical micrograph of the thin Cu_2O is shown in Figure 2.6.

The foils were released from the handle wafer after several microns of metal were deposited onto the back of the thin Cu_2O. The metal stabilized the 20 µm wafer and we were able to pick up the metal coated foils with tweezers. The thin wafer that is stabilized by the metal is shown in the final image of Figure 2.11. This metal was also able to serve as a back contact during electronic testing, which is further detailed in Chapter 6.

2.5 Summary of Growth of Cu_2O Wafers

Cu_2O is distinct from other semiconductors like silicon in that there is a simple and low cost method of producing phase pure bulk wafers with long minority carrier lifetimes. Additionally, this process is vacuum free, giving it an advantage over thin film technologies, especially CIGS, which is generally sputtered. The low capital process is also easily scalable, as the size of the wafer produced corresponds directly to the scale of the copper foil that was oxidized. There are also no cutting or polishing steps, greatly simplifying solar cell device production. Solar cell technologies that rely on wafer growth, primarily silicon, are thought of as intrinsically higher cost than thin films, but the simple route towards bulk Cu_2O production belies that simplification.

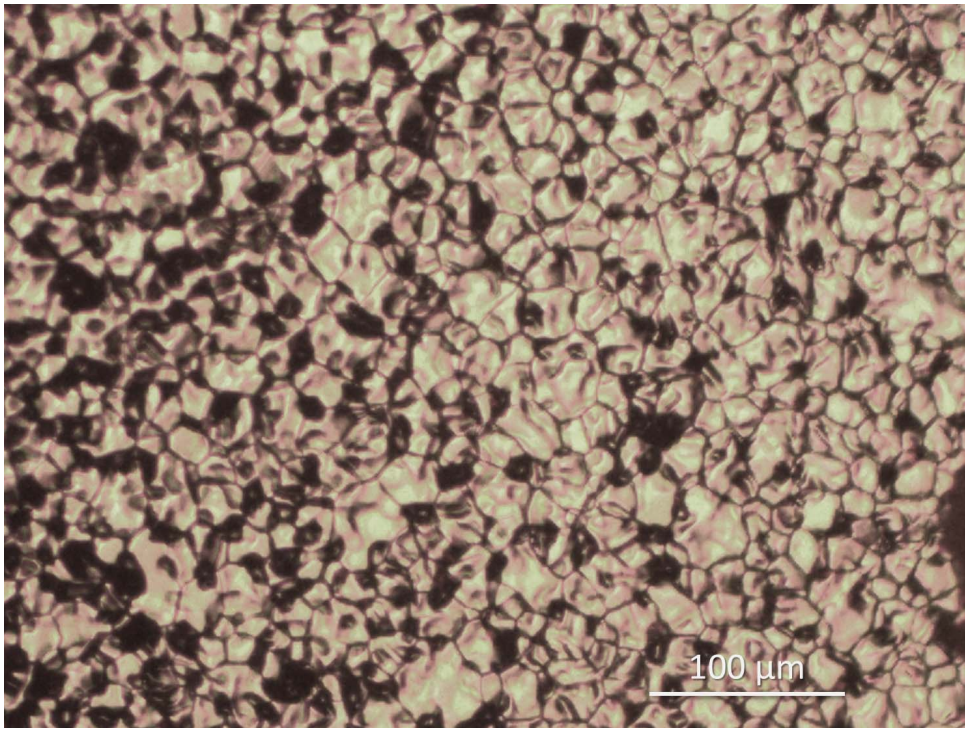

Figure 2.14: Optical microscope image of 20 µm thick Cu_2O. The lateral grain size is 30-50 µm, much smaller than the grains in the thicker wafers shown in Figure 2.6. The thin wafer is also noticeably rougher.

Chapter 3

Growth and Characterization of Zn-VI Thin Films

The fabrication of photovoltaic cells from Cu_2O requires a heterojunction partner because Cu_2O is not capable of being doped n-type [10, 11, 50]. This restriction led us to investigate Zn-VI thin films as potential earth-abundant heterojunction partners. The thin films were grown by various means, including sputtering and molecular beam epitaxy, and the specific materials studied were ZnO, ZnSe, ZnS and Zn(O,S). We chose this set of materials after a careful analysis of the enthalpy of formation of the solid oxide for every element in the periodic table with available data. This analysis indicted that Zn should have favorable chemistry with Cu_2O.

This chapter will describe the specific growth parameters and the characterization done on each film type. Characterization performed include, composition analysis by X-ray photoelectron spectroscopy, structure analysis by X-ray diffraction, and optical analysis by transmission and reflection.

3.1 Why Study Zn-VI Materials?

Even the most cursory review of Cu_2O photovoltaic literature will reveal that ZnO is the most studied heterojunction partner in Cu_2O photovoltaics [10, 25, 38, 36, 39, 42, 48, 45, 66, 60, 28, 33]. We believe there is cause for this beyond the obvious fact that ZnO is a well-known, n-type, wide-band gap conducting oxide [47]. We conducted an in depth review of common and uncommon oxide materials in order to develop a better understanding of what elements would be favorable components of a Cu_2O heterojunction partner. We evaluated all possible materials on several quantitative parameters including, abundance, heat of formation, and more qualitative parameters like stability in atmospheric conditions. We set a slightly arbitrary cut-off for necessary abundance at > 1 ppm in the earth's crust. We also evaluated all potential elements based on the heat of formation of the solid oxide. We did not include any more complex oxides in this analysis because that was deemed unnecessary. For instance, $SrTi_2O_3$ may be a good emitter material to evaluate, but if either strontium or titanium have oxide phases with large enthalpies of formation, $SrTi_2O_3$ is disqualified. Many elements, including copper, form multiple stable solid oxides. If there was more than one heat of formation to choose from, the largest heat of formation was used. Heat of formation numbers were sourced from the NIST chemical webbook [14]. Data for elemental abundance was found on the US Geological Survey website [4]. The raw data is presented in Appendix A, while a graphical visualization of the data is given in Figure 3.1 .

We used 500 kJ/mol and below as a slightly arbitrary definition of a small heat of formation for the solid oxide. There are 16 elements that have heats of formation less than 500 kJ/mol besides Cu_2O. However, when abundance data is also taken into

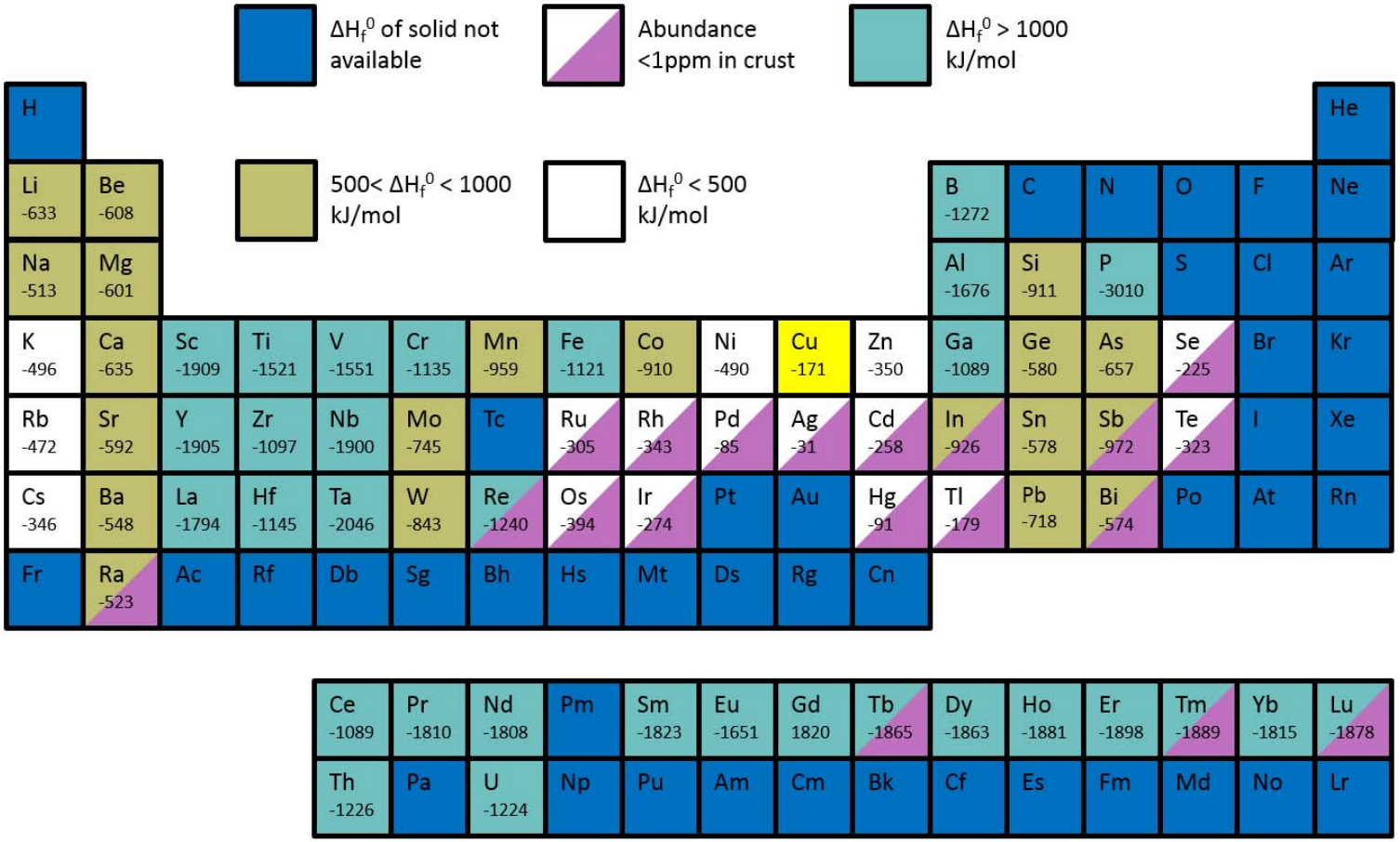

Figure 3.1: Analysis of enthalpy of formation of the solid oxide versus elemental abundance for every element in the periodic table. Copper is highlighted in yellow. This analysis clearly highlights the fundamental advantages of ZnO as a heterojunction partner for Cu_2O. ZnO is wide band gap, has a low enthalpy of formation, and only a single oxide phase.

account, we are only left with 5 materials. K_2O_2, Rb_2O_2, and Cs_2O were disqualified as materials of interest due to their corrosive nature and tendency towards violent reactions with water, according to their Material Safety Data Sheets. This left us with just NiO and ZnO. NiO is a semiconductor, but it is not well studied, and is usually reported as having p-type conductivity [34]. Thus the only element that is both abundant in the earth's crust and has low reactivity with oxygen is Zn. Furthermore ZnO only has the single oxidation state and one oxide phase, which is a remarkably simple chemistry with oxygen. Zn would appear to be the perfect component of a heterojunction partner, and ZnO would be a sensible material to study. We also chose to study the alternative anions S^{-2} and Se^{-2}. The thin films we made were ZnO, ZnSe, ZnS, and Zn(O,S).

3.2 Overview of AJA Sputtering System

All sputtering in these experiments was performed by an AJA sputtering system. The deposition chamber is outfitted with a load lock for rapid loading of samples. There are seven available sputter guns as well as four power supplies. Two power supplies are direct current (DC) and two are radio-frequency (RF), thus simultaneous deposition from up to 4 sample targets at once is possible. Material is sputtered from 2" diameter targets with a thicknesses of either 0.25" or 0.125" with a 0.125" copper backing plate to improve electronic contact. Pressure in the chamber is measured during deposition by a capacitance monometer and is usually held to between 3 and 10 mTorr. Ar is used as the working gas and is inlet in the sputter gun. Several reactive gases that inlet near the substrate can also be used, including pure O_2, N_2, and 10% O_2 in Ar. Distance from the substrate to the target is fixed at 35 cm. The substrate is rotated continuously during deposition at a rate of 10 rpm. Typical base pressure is on the order of $5*10^{-7}$ Torr. All thin films were deposited at room temperature.

3.3 Overview of Experimental Equipment and Methods for Characterization

We used very similar methods to characterize the thin films, so I will briefly review them here.

3.3.1 Phase Analysis by X-ray Diffraction

We used a PANalytical X'Pert MRD to perform all X-ray diffraction (XRD) measurements. Due to the geometry of our X-ray diffractometer the substrate was mounted vertically, usually with double-stick tape, onto a glass slide. The glass slide was used to avoid the diffraction peaks from the substrate holder, but did contribute its own amorphous peak around 20°, typical of amorphous SiO_2. Two different scanning geometries were used: the first is the more common theta-2theta geometry and the second is a grazing angle scan. In a theta-2theta scan the detector is rotated around the substrate at twice the rate in which the substrate is rotated (the X-ray source is fixed in position in our diffractometer). This geometry is appropriate for thick substrates, like Cu_2O, or oriented thin films, like the sputtered ZnO.

To analyze the amorphous and nano-crystalline thin films we used a grazing angle scan geometry. In the grazing incidence X-ray diffraction (GIXRD) the omega angle, or the angle between the sample and the X-ray source, was held at 1°. A detector, or 2theta, scan was performed while the sample was held fixed. In a theta-2theta scan only diffraction from the "symmetric" planes, or those planes parallel to the surface, can be seen. In grazing incidence the vector which defines the planes being probed rotates around the surface of the sample. Thus this method is only appropriate for thin films with randomly oriented grains or those that are amorphous. The benefit of this geometry is that because omega is held at a shallow angle, the scan is more sensitive to thin layers. From these two scans it can be seen that the GIXRD scan is much more sensitive to the thin film versus the substrate [16].

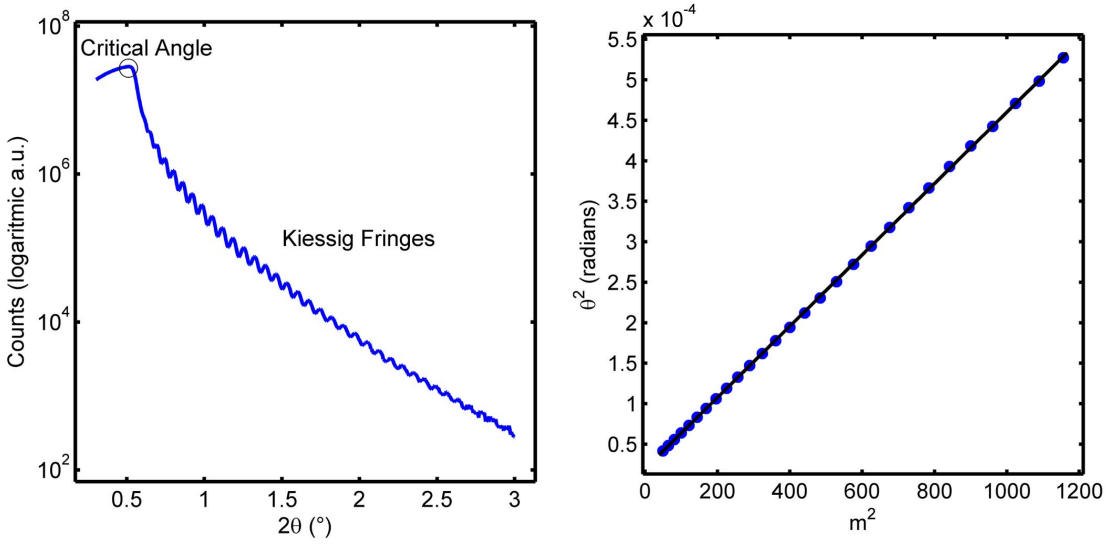

Figure 3.2: Raw data from an X-ray reflectivity measurement is shown at left. The processed data from which the film thickness is derived is shown at right.

3.3.2 Thickness Analysis by X-ray Reflectivity

X-ray reflectivity (XRR) is a useful optical technique for determining thickness of films by analyzing the Kiessig fringe pattern in a very low angle symmetric X-ray diffraction scan. There are several requirements of a good sample. First, the surface of the thin film and the interface between the thin film and the substrate must be smooth (rms $<$ 1 nm). Otherwise the background scattering will be too large to get a reasonable signal to noise ratio. Furthermore the thickness of the sample should not exceed ~200 nm. As the film gets thicker the interference fringes grow closer together, and thus the resolution of the instrument dictates that the sample must be less than 200 nm. Also, in order to obtain a strong signal there must be sufficient refractive index contrast between the film and the substrate. A maximum signal is achieved if the refractive index of the film is larger than that of the substrate. For these reasons we used polished fused silica wafers obtained from MTI for these experiments. They have a small refractive index and a very smooth surface, making them ideal XRR substrates. The basic shape of an XRR scan is shown in Figure 3.2 . The critical angle, the point at which the intensity suddenly decreases, is marked in the figure.

It is the point at which the beam is no longer entirely reflected by the surface of the sample and starts to penetrate into the sample. Beyond the critical angle the fringes start to appear. The 2-theta position of the peaks can be extracted using the following equation:

$$\theta^2 - \alpha_c^2 = m^2 \left(\frac{\lambda}{2d}\right)^2$$

where ϑ is the angle, α_c is the critical angle, m is the index of the peak, λ is the wavelength of the X-rays, and d is the thickness. The peak position in radians is squared and plotted versus an arbitrary index, shown in Figure 3.2. The slope of this line contains the thickness of the sample. We fit the index of the first peak by making sure that the value given for the critical angle was close to the actual value in the scan, and additionally that the fit to the plotted data minimized the value of r^2. Frequently the first fringe to appear will not have an index of 1. The fringe with the index of 1 will be obscured by the critical angle of the film. The thickness is derived from the slope of the fitted line [16].

We used this method because if the sample was sufficiently smooth and thin, we could extract the thickness of the sample without knowing any of the material's optical properties. We also found this to be easier than profilometry because we did not need a sharp step edge to determine the sample thickness.

3.3.3 Composition Analysis by X-ray Photoelectron Spectroscopy

X-ray photoelectron spectroscopy (XPS) is a compositional analysis method that looks at the energy distribution of electrons scattered from a sample surface by an X-ray beam. A more detailed discussion of XPS is given in Chapter 4. To determine sample composition of the Zn(O,S), the pure sputtered ZnO film was used as the standard. The ratio of the area of the Zn 2p peak was compared to the ratio of the area of the O 1s peak in order to determine the fraction of the sample that was ZnO versus ZnS or $ZnSO_4$. The ZnO phase was chosen as the standard due to its great overall simplicity, and the ease with which the oxygen bound with Zn can be separated from oxygen bond as SO_4^{-2} or OH^-.

In order to differentiate the composition of ZnS versus $ZnSO_4$ in the $Zn(S,SO_4)$ films, the S 2p peak was used with the ZnS sample serving as a standard. The ratio of sulfur bound as S^{-2} versus SO_4^{-2} was directly compared to make composition measurements [15].

3.3.4 Optical Analysis by Transmission, Reflection, and Ellipsometry

The transmission and reflection measurements were performed by a Cary 5000 UV-Vis-NIR spectrophotometer with an integrating sphere to capture diffuse light. All samples used for transmission and reflection measurements were deposited onto large fused silica wafers. Absorption was calculated from the transmission and reflection data according to the following equation:

$$\alpha = -\frac{1}{d}\ln\left(\frac{T}{(1-R)}\right)$$

where α is absorption, d is thickness, T is transmission, and R is reflection. The thickness was usually calculated by an XRR measurement performed on the same film that the transmission and reflection measurements were performed on.

Once absorption is calculated, a Tauc plot can be constructed according to the equation:

$$(h\nu\alpha)^n = A\,(h\nu - E_g)$$

where h is Planck's constant, ν is wavelength, E_g is band gap, and A is a proportional constant. The nature of the transition being observed defines the value of n. For a direct allowed transition n = 2, for a direct forbidden transition n = 2/3, for an indirect allowed transition n = 1/2, and for an indirect forbidden transition n = 1/3. Because ZnO and ZnS both have direct allowed transitions at the absorption edge, we have used n = 2 for all alloys. A Tauc plot is constructed by plotting $(h\nu\alpha)^2$ versus $(h\nu)$. The band gap can then be derived from this plot by extrapolating the linear

portion of the curve to 0 energy [56].

Spectroscopic ellipsometry measurements were performed by a J.A. Wollam alpha-SE ellipsometer. Refractive index data was derived from fitting the delta and epsilon ellipsometry parameters to a Cauchy model. All thin films used for ellipsometry were deposited on SiO^2 coated silicon.

3.3.5 Electronic Analysis by Four Point Probe and Analysis of Valence Band Data

The electronic properties proved to be the most difficult parameter to measure. Hall measurements of all samples proved impossible because the mobilities of all the materials were too low to detect a Hall effect. We were able to take 4-point contact measurements on ZnO, but the other samples proved too resistive to pass enough current for a 4-point contact measurement. Thus we mostly used XPS measurements of the valence band to gain some insight about the Fermi level position in the sample, particularly if the sample was n- or p-type. This is very similar to how we calculated the Fermi level position of Cu_2O in the previous chapter. This is a somewhat less accurate technique because we are unable to take into account the instrument broadening error, or the shape of the valence band, but it will give us a general idea of the Fermi level position with an error of around 0.2 eV.

3.4 Manufacture of ZnO and Zn Thin Films by Sputter Deposition

ZnO for studies were fabricated by radio-frequency magnetron sputter deposition of Zn or ZnO directly onto an untreated Cu_2 O surface at room temperature. The sputtering source was a 2" diameter and 0.125" thick ceramic target mounted on a 0.125" thick Cu backing plate. The sputtering sources were purchased either from AJA or Kurt Lesker. ZnO films were deposited at 100 W substrate power. The total pressure in the chamber was 5 mTorr whenever depositing directly onto a Cu_2

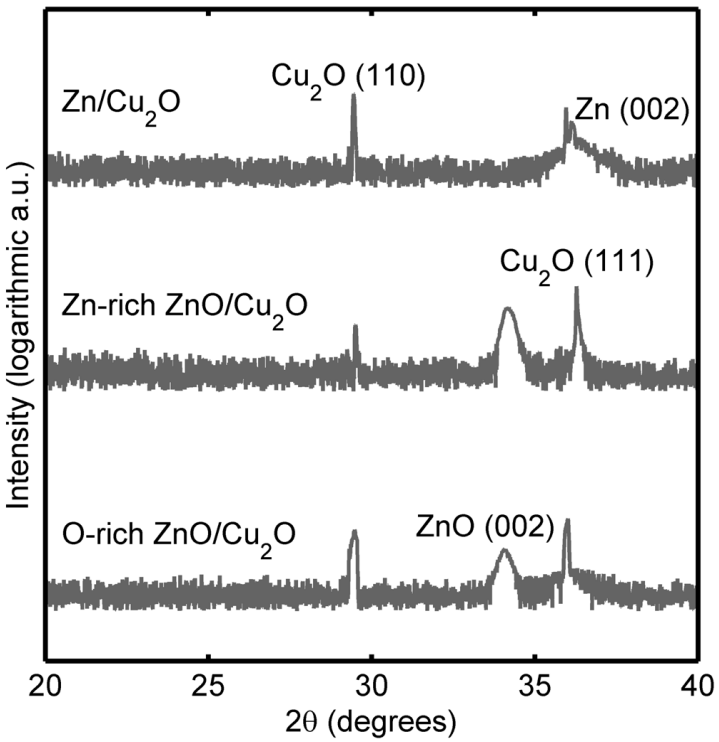

Figure 3.3: XRD data for ZnO/Cu_2O heterostructures. ZnO films were oriented along the (001) orientation and are phase pure. Zn film is also phase pure.

O surface. ZnO was sputtered under both a pure Ar atmosphere and a 0.25 mTorr partial pressure of O_2 in Ar. The ZnO sputtered with O_2 was O-rich as indicated by its resistivity (ρ>1000 Ω-cm), while the ZnO sputtered in pure Ar was Zn-rich (ρ~1 Ω-cm). Zn was sputtered only under a pure Ar atmosphere. ZnO films were characterized by XRD, XPS, transmission, and reflection. XRD of the ZnO and Zn films on Cu_2O can be seen if Figure 3.3 . Both the O-rich and Zn-rich ZnO are phase pure. Additionally, the sputtered ZnO thin films were always oriented along the c-axis with the only XRD peak visible being the (001) peak. This is a common orientation for sputtered, nano-crystalline ZnO thin films [47]. Pure zinc films were also used for some experiments. The zinc was deposited by RF magnetron sputtering from an elemental zinc target.

Optical data for ZnO is presented in the discussion of Zn(O,S).

3.5 Growth of ZnS and ZnSe Thin Films by MBE

ZnS and ZnSe thin films were grown by collaborator Jeffrey Bosco on untreated Cu_2O surfaces by compound-source molecular-beam epitaxy. Standard Knudsen effusion cells loaded with ZnS (6N) and ZnSe (6N) were employed. All depositions were performed at room temperature with a beam pressure of around $1*10^{-6}$ Torr (ZnS and ZnSe source temperatures of 825 °C and 850 °C respectively). The details of ZnS and ZnSe growth are reported in several references [12, 13]. The films were undoped, electrically resistive, and phase pure according to XRD.

3.6 Growth of Zn(O,S) and Related Alloys by Sputter Deposition

We attempted several different sputtering methods for Zn(O,S) and as a result we obtained a family of alloys with different physical properties depending on deposition method and composition. The material characteristics were particularly sensitive to the concentration of oxygen in the growth atmosphere. The growth methods and characterization of the thin films have been divided by growth method.

3.6.1 Growth of Zn(O,S) by Co-Sputter Deposition

Zn(O,S) has emerged in recent years as a Cd free alternative to CdS buffer layers in CIGS solar cells [49]. It has developed rapidly into a commercial electronic material and is already being deployed in Solar Frontier CIS solar cells [2]. Because it was developed to replace the CdS layer, which is traditionally deposited by chemical bath deposition (CBD), most Zn(O,S) studied is also deposited by CBD [49]. It can also be synthesized by atomic layer deposition [46], pulsed laser deposition [23], chemical spray pyrolysis [58], and sputtering [22, 44, 68]. We have decided to study sputtered Zn(O,S) because of our success with sputtered ZnO thin films.

The Zn(O,S) used in these experiments was primarily grown by co-sputter de-

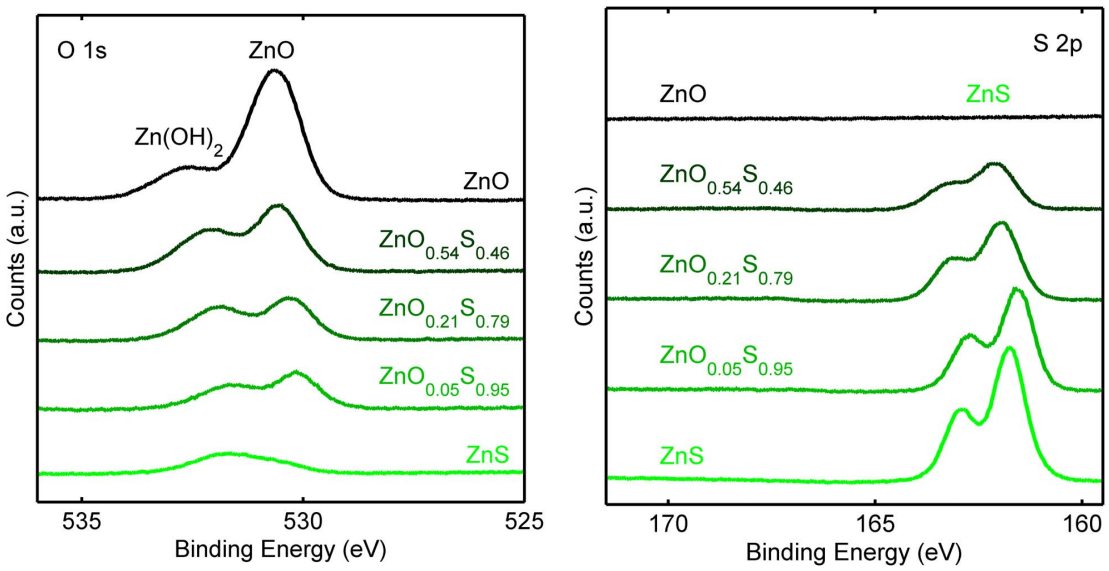

Figure 3.4: X-ray photoelectron spectroscopy data for Zn(O,S) of indicated composition. High-resolution scans were taken of the S 2p and O 1s peaks in order to determine the ratio of oxygen to sulfur and also the chemical state the elements. Sulfur is present as S^{2-} while oxygen is O^{2-}. There is also some adventitious $Zn(OH)_2$ due to the surface being exposed to air.

position after the method proposed by Grimm et. al. [22]. For the Zn(O,S) an aluminum-doped ceramic ZnS target was used. The target was 0.1% aluminum by weight and was mounted on a 0.125" thick copper backing plate to ease striking a plasma. The oxygen source was an aluminum doped ZnO target, from here on out referenced as AZO. The target was 2% Al_2O_3 by weight. The materials were co-sputtered, and during deposition the ration of power on the targets was varied to access different compositions of Zn(O,S). The sputtering ambient was pure Ar and the overall deposition pressure was maintained at 5 mTorr.

The composition of the Zn(O,S) was determined by XPS according to the procedure outlined above. The data is shown in Figure 3.4. Compositions are listed in Table 3.2 along with all relevant characterization data. Composition varied fairly linearly with target power, which is also listed in Table 3.1. These XPS scans also give us some chemical information about Zn(O,S). We call this alloy Zn(O,S) pre-

Composition	Power on Al:ZnS Target	Power on Al:ZnO Target	Band Gap	(Fermi Level) - (Valence Band)
ZnO	0 W	100 W	3.22 eV	2.96 eV
$ZnO_{0.54}S_{0.46}$	50 W	100 W	3.11 eV	2.23 eV
$ZnO_{0.21}S_{0.79}$	100 W	100 W	2.96 eV	1.98 eV
$ZnO_{0.05}S_{0.95}$	100 W	50 W	3.21 eV	1.50 eV
ZnS	100 W	0 W	3.33 eV	1.63 eV

Table 3.1: This table reviews all of the chemical, electronic, and optical data recorded for Zn(O,S). By comparing the band gap data to the energy difference between the Fermi level and the valence band, we determined that the films were either intrinsic or n-type.

cisely because the high resolution data for the S 2p peak indicates that most of the sulfur in material is characteristic of the S^{2-} anion bound as ZnS. Analysis of the O 1s peak shows additionally that most of the oxygen is bound as O^{2-} bound as ZnO. XPS measurements of the valence band were also used to extract some information about the Fermi level of the. The valence band data is shown in Figure 3.5

and the Fermi level position is listed next to the band gap data in Table 3.1. The Fermi level for ZnS sits right in the middle of the band gap. ZnS is known as an easily compensated material, so given our room temperature growth conditions, this Fermi level position is expected. As the oxygen concentration in the Zn(O,S) increased, the Fermi level shifted closer to the valence band. Also the Fermi level indicates that the Zn(O,S) were all n-type materials.

The phase of the films was characterized by XRD. We employed a GIXRD scan rather than a more traditional symmetric scan geometry because the films that we were looking at were very thin, on the order of 100 nm. The GIXRD scans can be seen in Figure 3.6 . These scans indicate that the Zn(O,S) material is amorphous for intermediate compositions. The single broad peak in grazing incidence is indicative of an amorphous material. Furthermore, we see no evidence of crystalline inclusions of

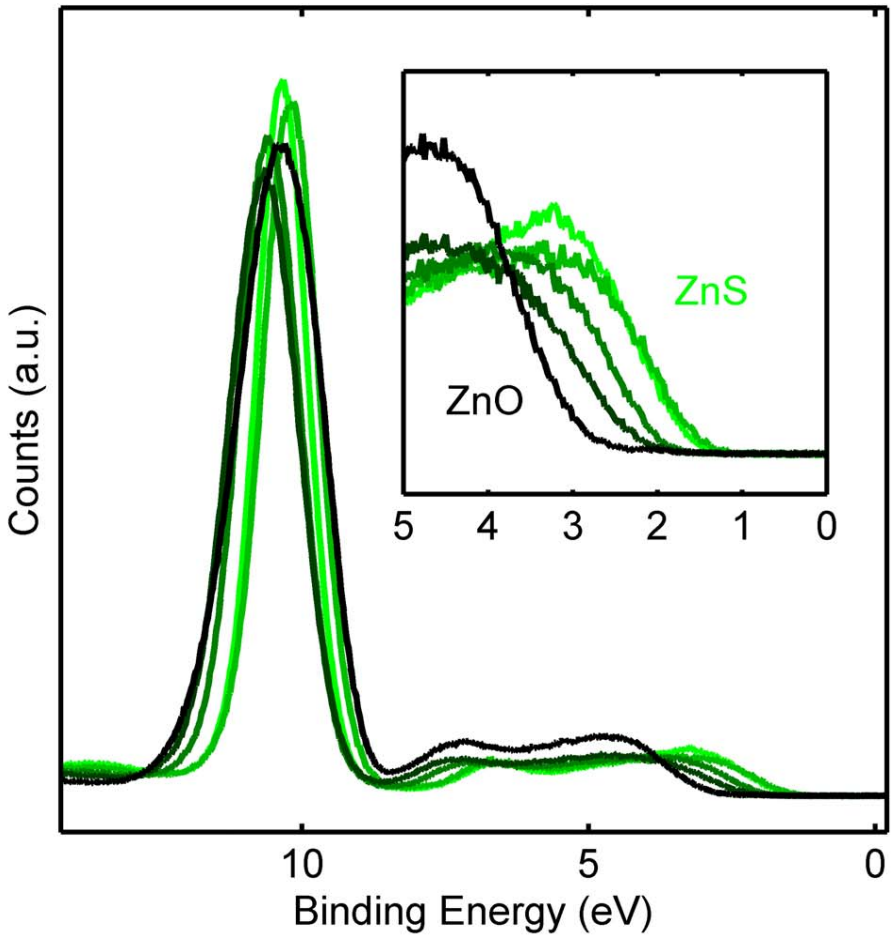

Figure 3.5: High-resolution X-ray photoelectron spectroscopy of the valence band for the indicated Zn(O,S) compositions. All materials appear to be n-type, with the concentration of oxygen in the sample increasing along with carrier concentration.

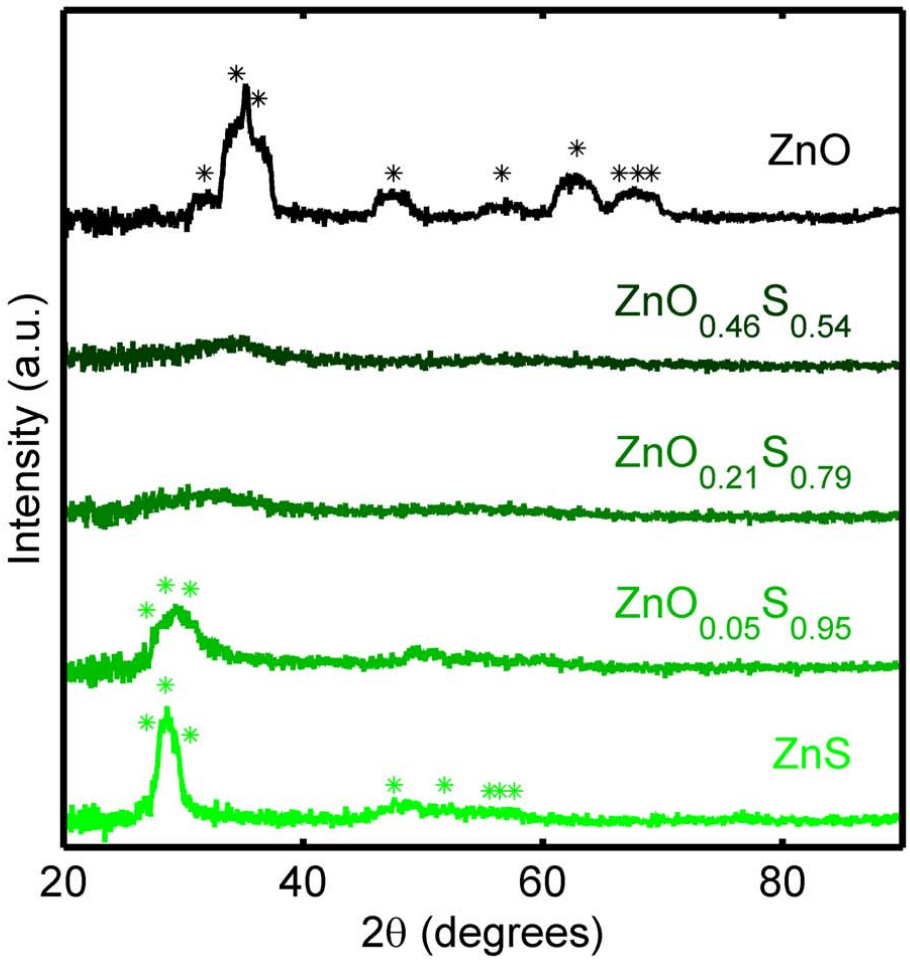

Figure 3.6: Grazing incidence X-ray diffraction spectra for Zn(O,S). Peaks indexed as ZnO are indicated by black stars, while peaks indexed as ZnS are indicated by green stars. The composition of the Zn(O,S) is indicated. The ZnO and ZnS films were nano-crystalline and phase pure. The Zn(O,S) films were amorphous at intermediate compositions, while the sulfur-rich film had some crystalline ZnS present.

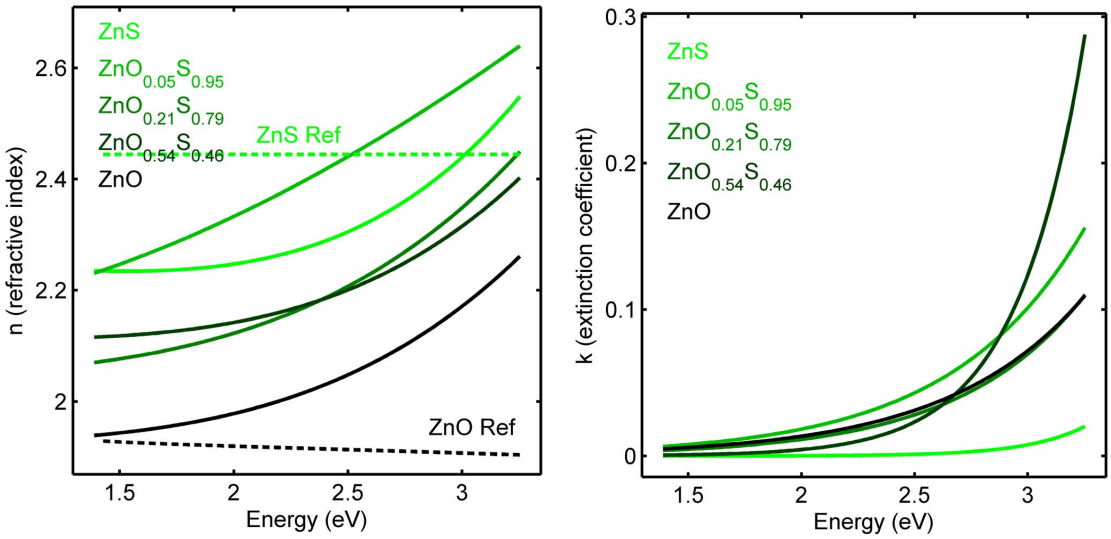

Figure 3.7: Spectroscopic ellipsometry measurements were fit to a Cauchy model to extract the real and imaginary parts of the refractive index. The composition of the Zn(O,S) is indicated. Refractive index data for pure ZnO and ZnS are marked for reference. The Zn(O,S) values fall between ZnO and ZnS.

ZnO or ZnS, confirming that we have indeed manufactured a novel material, different from crystalline ZnO or ZnS.

The optical properties were characterized both by ellipsometry and by transmission and reflection measurements. The ellipsometry data is shown in Figure 3.7

I have plotted the data collected from our films as well as some reference data for bulk ZnS and ZnO. The shape of the data deviates from the reference data at higher energies, probably due to the poorer fit by the Cauchy model when absorption is larger. The Cauchy model is more appropriate when k can be assumed to be nearly zero. The ZnO and ZnS data lines mostly fell between ZnS and ZnO, indicating Zn(O,S) has intermediate optical properties. The extinction coefficient data shows evidence of band bending as the alloy nears 50% sulfur, for which Zn(O,S) is well known [35].

Transmission, reflection, and absorption data are shown in Figure 3.8. The fringes are caused by thin film interference. Tauc plots, shown in Figure 3.9, were built from the absorption data once the thickness of the films was derived from XRR measure-

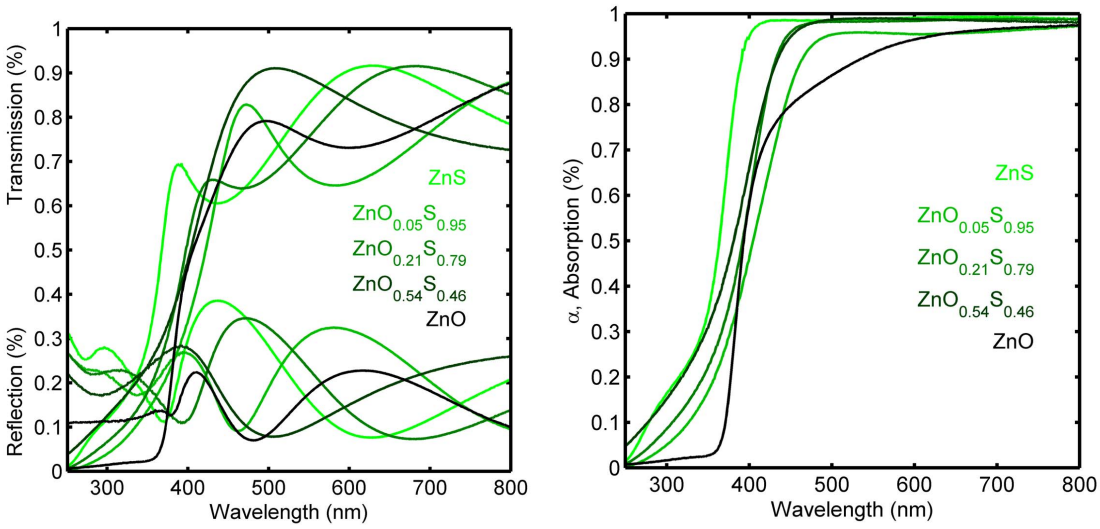

Figure 3.8: Transmission and reflection data for Zn(O,S) are shown on the left, composition is indicated. The fringes are due to thin film interference. Absorption is calculated from this data and shown on the right.

ments. Once the Tauc plot is constructed, the optical band gap can be obtained according to the procedure outlined above. In order for a Tauc plot to be accurate, you must know at least the order of magnitude of the absorption coefficient around the band gap, otherwise the extrapolating line is incorrectly fit to the curve. The Zn(O,S) optical properties are not entirely settled, so we chose to look at absorption in the range of 10^5, which is what the absorption coefficient at the band gap is for ZnO and ZnS. We also assumed a direct allowed gap and used 2 as our Tauc coefficient. For ZnO we saw a band gap of 3.22 eV which is right in line with what is reported in literature [47]. By contrast, we saw a somewhat smaller band gap than typically reported with for ZnS. We calculated the band gap as 3.3, which is slighly less the the typically reported value of 3.5 eV [55]. We speculate this difference is due to some amount of ZnO in the sputtered ZnS, but we could not confirm this experimentally. The Zn(O,S) band gaps showed evidence of band bending, meaning that all the alloys actually had much smaller band gaps than the bulk materials. This is commonly reported in Zn(O,S) alloys, though we did not see band gaps on the lower end of reported values, which reached as low as 2.5 eV [35]. Band gaps are reported

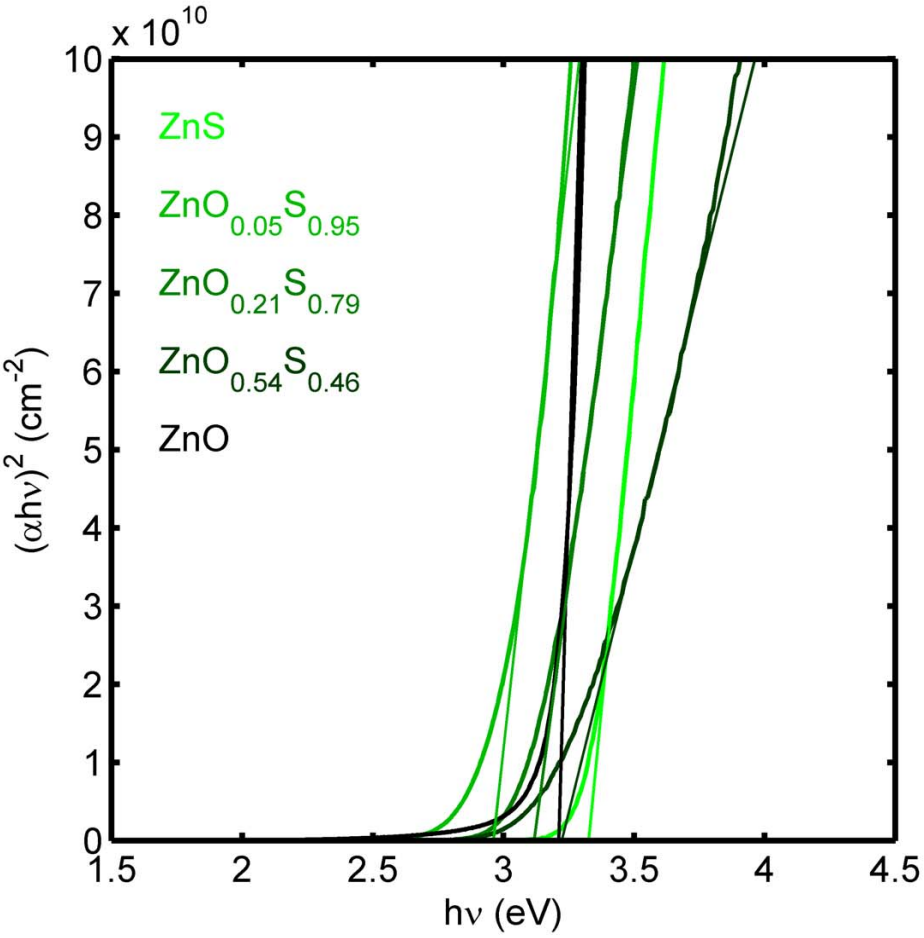

Figure 3.9: Tauc plot constructed from absorption data and thickness data according to the procedure outlined above. The band gap can be extracted from a Tauc plot by extrapolating the linear region to zero; the fit lines are also plotted. Band gaps derived from this figure are shown in Table 3.1.

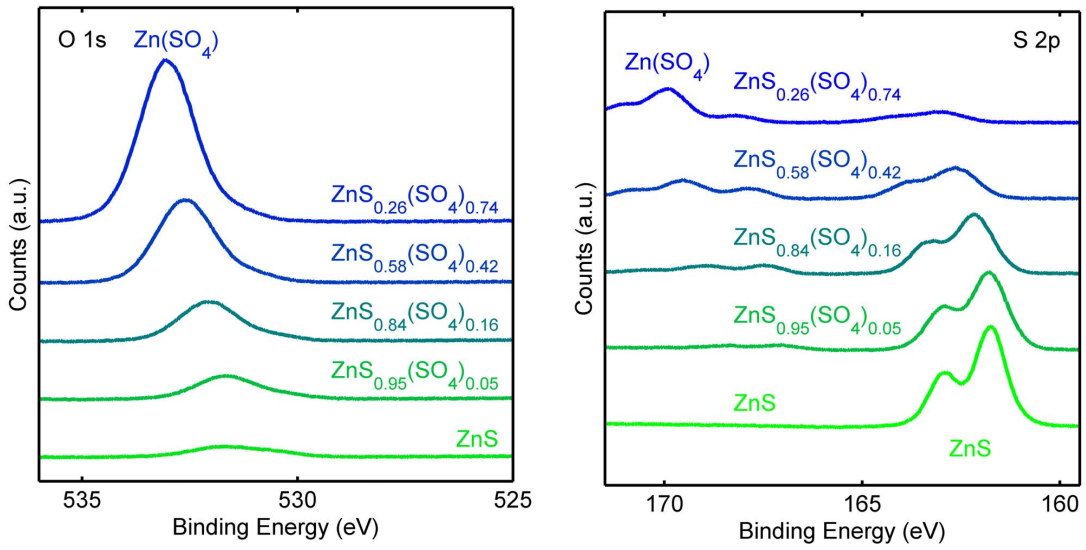

Figure 3.10: High resolution X-ray photoelectron spectroscopy of the S 2p and O 1s regions of $Zn(S,SO_4)$ thin films deposited on Cu_2O. The O 1s peak is the result of oxygen bound as SO_4^{2-}, which has a larger binding energy than oxygen bound as the O^{2-} ion. Additionally, SO_4^{2-} formation can also bee seen in the S 2p peak as it shifts from near 162 eV, characteristic of S^{2-}, to 170 eV, which is characteristic of SO_4^{2-}.

in Table 3.1.

3.6.2 Growth of $Zn(S,SO_4)$ by Reactive Sputter Deposition

We also attempted growth of a Zn-O-S alloy by reactive sputter deposition of Al:ZnS in an oxygen-containing ambient. The same Al:ZnS target containing 0.1% aluminum was employed as the source of Zn and S. The oxygen source was a flux of 10% O_2 in Ar that was inlet into the sputtering chamber near the substrate. The power on the Al:ZnS target was fixed at 100 W and the overall deposition pressure was kept constant at 5 mTorr. The Ar sputtering gas that was inlet near the target was flowed at 10 sccm. The flow rate of the reactive oxygen mixture was controlled from 0 to 10 sccm, which related to a change in the partial pressure of O_2 from 0.0 to 0.25 mTorr.

Once again the chemical composition of the material was assessed by XPS. The data for the O 1s and S 2p peaks are shown in Figure 3.10. In this case the S 2p peak

Composition	Ar/O_2 Gas Flow	Partial Pressure O_2 in Deposition Ambient	Band Gap	(Fermi Level) - (Valence Band)
ZnS	0.0 sccm	0.00 mTorr	3.33 eV	1.63 eV
$ZnS_{0.95}(SO_4)_{0.05}$	1.0 sccm	0.05 mTorr	3.46 eV	1.65 eV
$ZnS_{0.84}(SO_4)_{0.16}$	2.5 sccm	0.10 mTorr	3.74 eV	2.14 eV
$ZnS_{0.58}(SO_4)_{0.42}$	5.0 sccm	0.17 mTorr	4.18 eV	2.74 eV
$ZnS_{0.26}(SO_4)_{0.74}$	10.0 sccm	0.25 mTorr	5 eV	3.53 eV

Table 3.2: This table reviews all of the chemical, electrical, and optical data for $Zn(S,SO_4)$. The power on the Al:ZnS target was fixed at 100 W for all depositions. The films were determined to be n-type by comparing the band gap data to the Fermi-level to valence band difference.

shows that as the films became more oxygen rich, the chemical state of the sulfur atoms shifted from primarily S^{2-} to SO_4^{2-}. The O 1s peak shows that all oxygen was bound not as O^{2-}, but as primarily SO_4^{2-}. For this reason, this alloy was referred to as $Al:Zn(O,SO_4)$. The ratio of S^{2-} to SO_4^{2-} was determined by analyzing the area of the S^{2-} peaks versus the area of the SO_4^{2-} peaks. This stands in contrast to the Zn(O,S) alloy, where there was never evidence of SO_4^{2-} formation in the XPS data.

XPS measurements were also used to derive some electronic information about the samples, since the samples proved too resistive for 4-point electronic characterization.

The valence band XPS data is shown in Figure 3.11. As the SO_4^{2-} character of the thin films increased, the difference between the Fermi level and the valence band increased dramatically. The exact difference in eV between the valence band edge and the Fermi level was determined according to the method outlined above. Additionally this information was compared the the band gaps, also listed in Table 3.2, to determine that all the films were n-type.

The phase of the films was characterized by XRD. We employed a GIXRD scan rather than a more traditional symmetric scan geometry because the films that we were looking at were very thin, on the order of 100 nm. The GIXRD scans can be seen

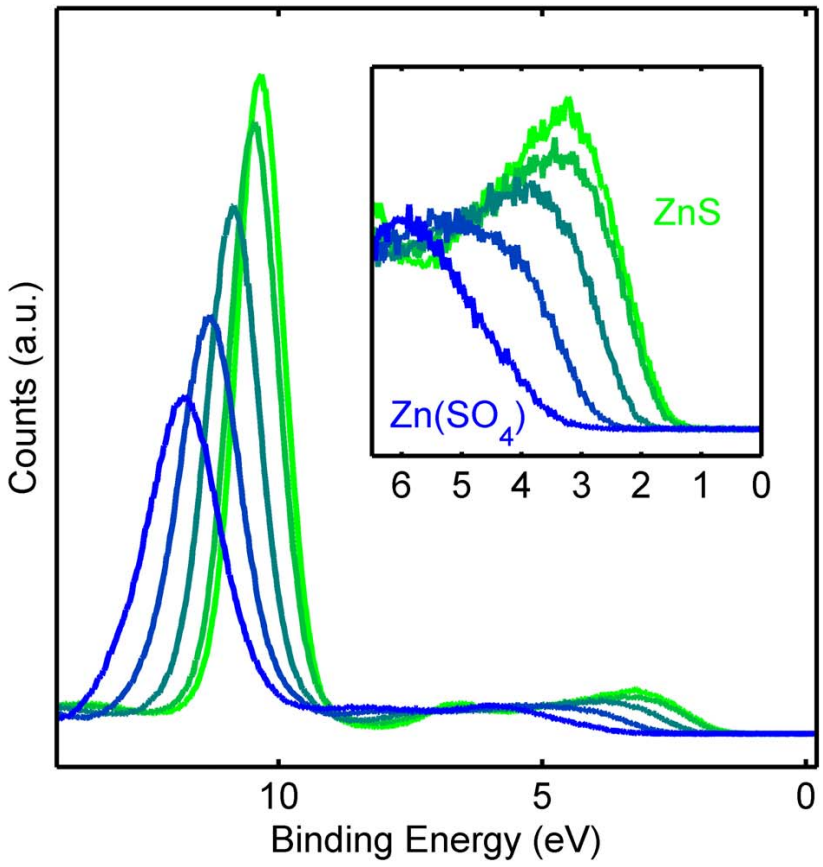

Figure 3.11: High-resolution X-ray photoelectron spectroscopy data of the valence band for $Zn(S,SO_4)$ deposited on Cu_2O. All films analyzed were at least 100 nm thick. The Fermi level to valence band split was measured by extrapolating the valence band edge to the baseline. Values for Fermi level to valence band split are listed in Table 3.2 and show that all the films are n-type.

in Figure 3.12 . The single, broad peak at intermediate compositions indicates that the $Zn(S,SO_4)$ material is amorphous. There is some evidence of formation of ZnS at S^{2-} rich compositions, but intermediate compositions show no evidence of ZnO or ZnS, confirming that we have indeed manufactured a novel material. Also, the final composition of $Zn(S,SO_4)$ was misplaced before XRD measurements could be taken, so there is no data for $ZnS_{0.26}(SO_4)_{0.74}$.

The optical properties of the thin films were studied both by spectroscopic ellipsometry and transmission and reflection measurements. The raw ellipsometry data was fit to a cauchy model and the resultant real and imaginary parts of the refractive index are shown in Figure 3.13. The data linearly shifts from a refractive index near the ZnS reference to a smaller near the $ZnSO_4$ reference as the $SO_4{}^{2-}$ character of the film increases. The extinction coefficient also linearly decreases with increasing SO_{42-} concentration, and the material displays none of the band bending that characterized Zn(O,S) thin films.

Transmission and reflection data, as well as absorption data calculated from transmission and reflection, are shown in Figure 3.14. Unfortunately there is no data for the $ZnS_{0.26}(SO_4)_{0.74}$ composition, as that sample was misplaced before measurements could be taken. The fringes in the transmission and reflection data are a typical thin film interference pattern. The absorption data shows a fairly linear decrease in absorption with increasing $SO_4{}^{-2}$ concentration with no evidence of band bending. Tauc plots were constructed for the Al:$Zn(S,SO_4)$ system in the same manner as described above and are shown in Figure 3.15. The band gap data from analyzing the Tauc plots is given in Table 3.2. The data shows that as the concentration of $SO_4{}^{-2}$ increases in the alloy, the band gap dramatically increases. Thus similarly to Zn(O,S), $Zn(S,SO_4)$ is an amorphous, n-type material. However, $Zn(S,SO_4O)$ shows a linear increase in band gap as the $SO_4{}^{2-}$ concentration increases, while Zn(O,S) shows a band gap smaller ZnO or ZnS at intermediate compositions.

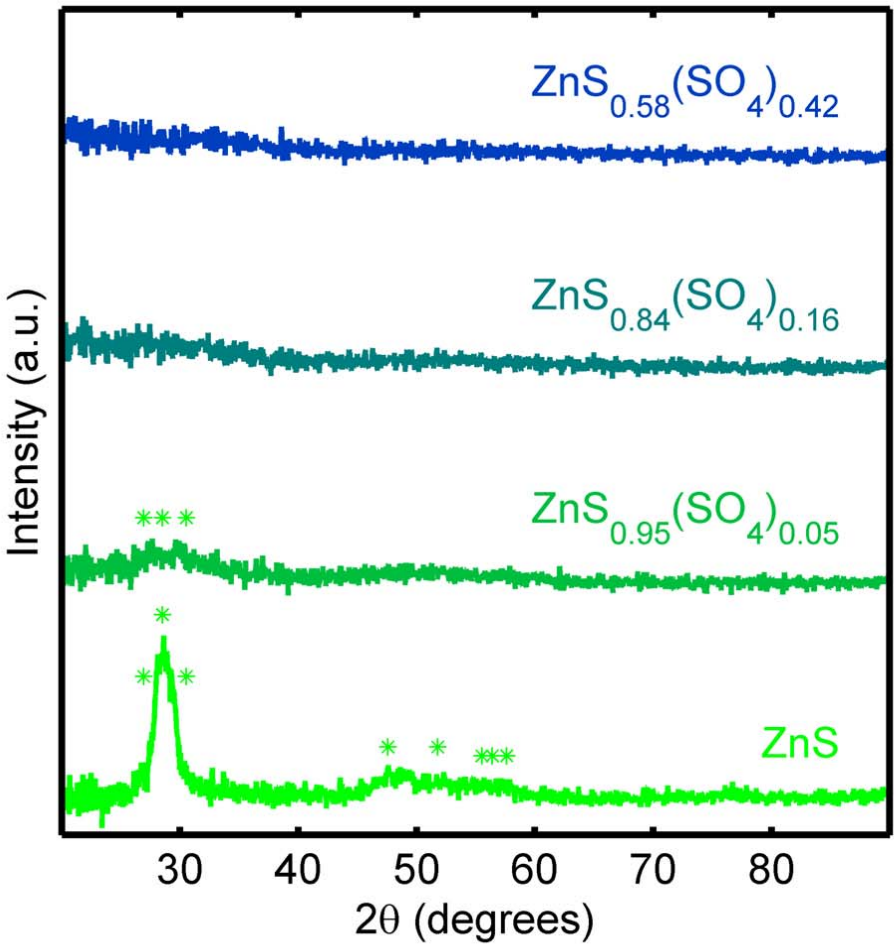

Figure 3.12: Grazing incidence X-ray diffraction spectra for $Zn(S,SO_4)$. Peaks indexed as ZnS are indicated by green stars. The composition of the $Zn(S,SO_4)$ is indicated. The ZnS films is nano-crystalline and phase pure. The $Zn(S,SO_4)$ films were amorphous at intermediate compositions, while the sulfur-rich film had some crystalline ZnS present.

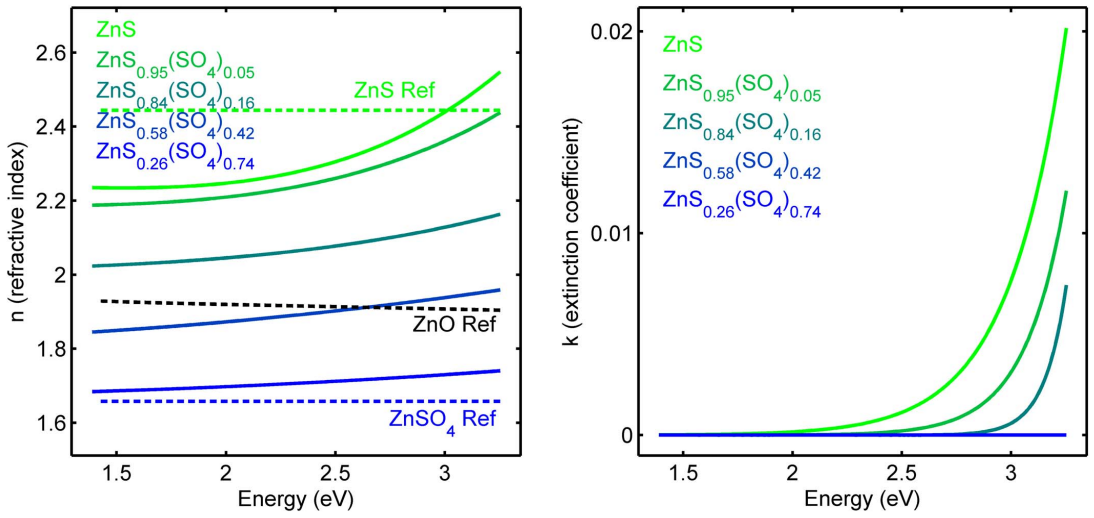

Figure 3.13: Spectroscopic ellipsometry data were fit to a Cauchy model to produce the real and imaginary parts of the refractive index plotted above. Reference data for bulk, crystalline ZnO, ZnS, and $ZnSO_4$ were also marked on the plot.

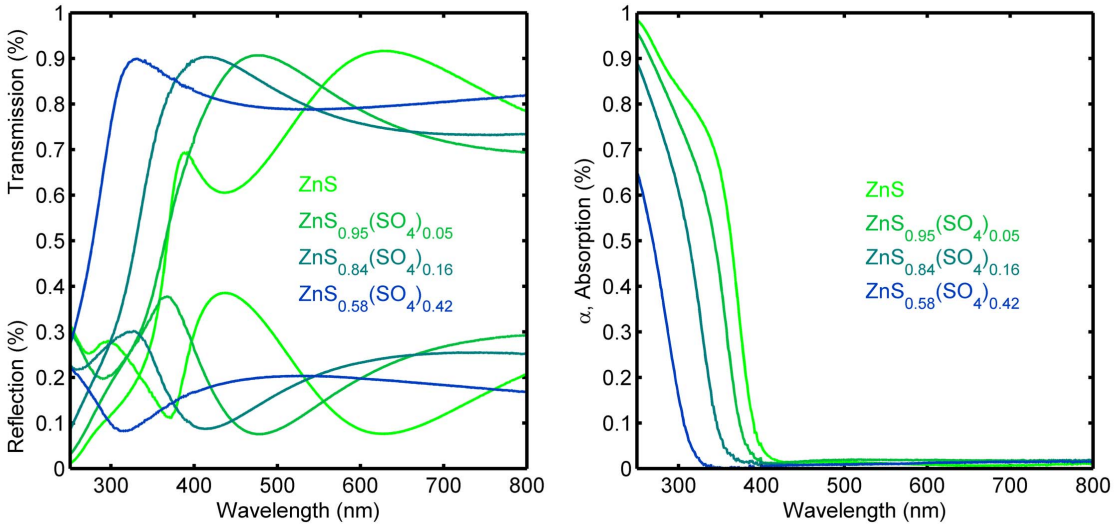

Figure 3.14: Transmission, reflection, and absorption data for $Zn(S,SO_4)$ deposited on fused silica. The fringes were the result of thin film interference.

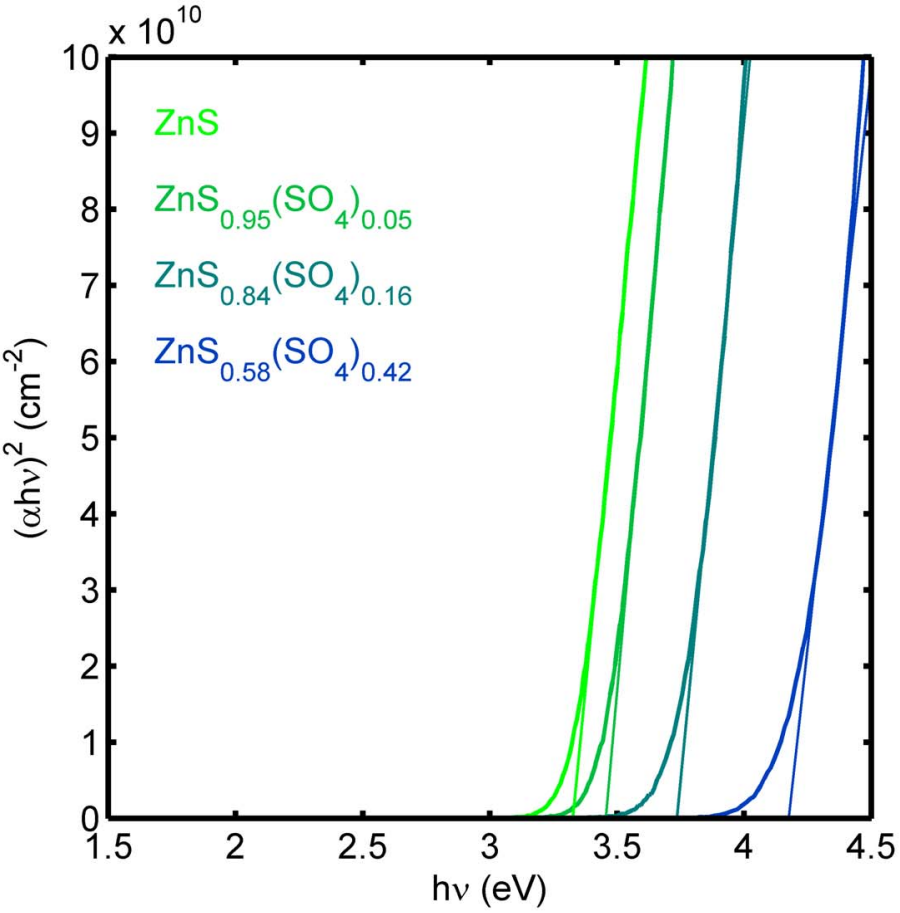

Figure 3.15: The Tauc plot was constructed from the absorption and thickness data according to the procedure outlined above. The linear regions have been fit with lines and extrapolated to zero to determine the material's band gap.

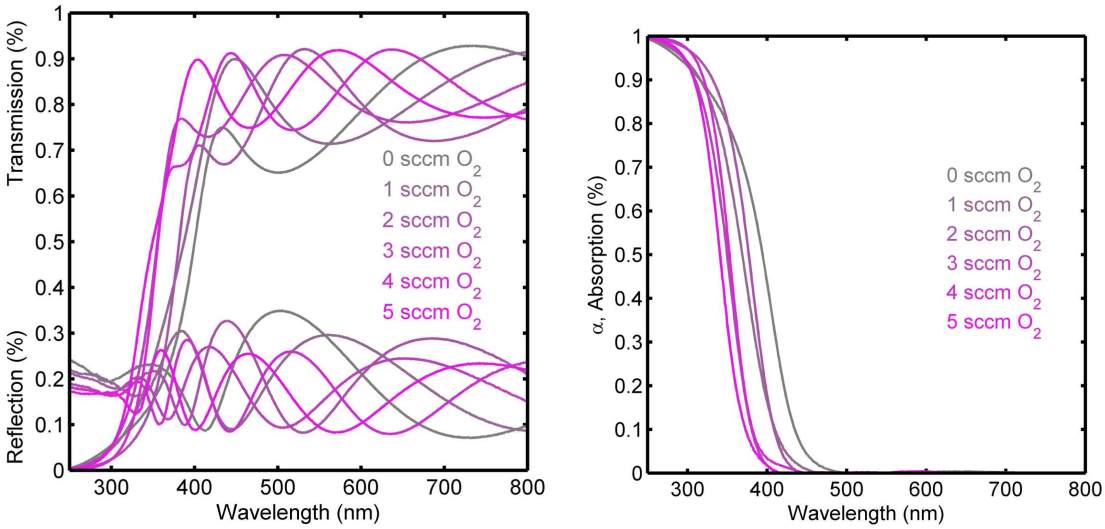

Figure 3.16: Transmission, reflection, and absorption data for $Zn(O,S,SO_4)$ deposited on fused silica. The fringes were the result of thin film interference.

3.6.3 Growth of $Zn(S,O,SO_4)$ by Reactive Co-Sputter Deposition

One final Zn-O-S alloy was briefly studied. This alloy was grown by the reactive co-sputter of AZO and Al:ZnS targets in an ambient containing oxygen. The Al:ZnS and AZO powers were held fixed at 100 W. The total pressure of the chamber was still restricted to 5 mTorr. The reactive oxygen source was a flow of 10% O_2 in Ar which was varied from 0 sccm to 10 sccm. Reflection and transmission data are shown Figure 3.16 and the Tauc plot is shown in Figure 3.17 . Similarly to the $Zn(S,SO_4)$ material, as the oxygen flow rate was increased the band gap increased.

3.7 Summary of Zn-VI Thin Film Growth

We chose to study Zn-VI materials as emitters in Cu_2O photovoltaics devices due to their favorable thermodynamics with copper compounds, the chemical simplicity of zinc, and the ease by which most Zn-VI materials can be doped n-type. Additionally, even a superficial glance through Cu_2O literature will reveal that ZnO is the most

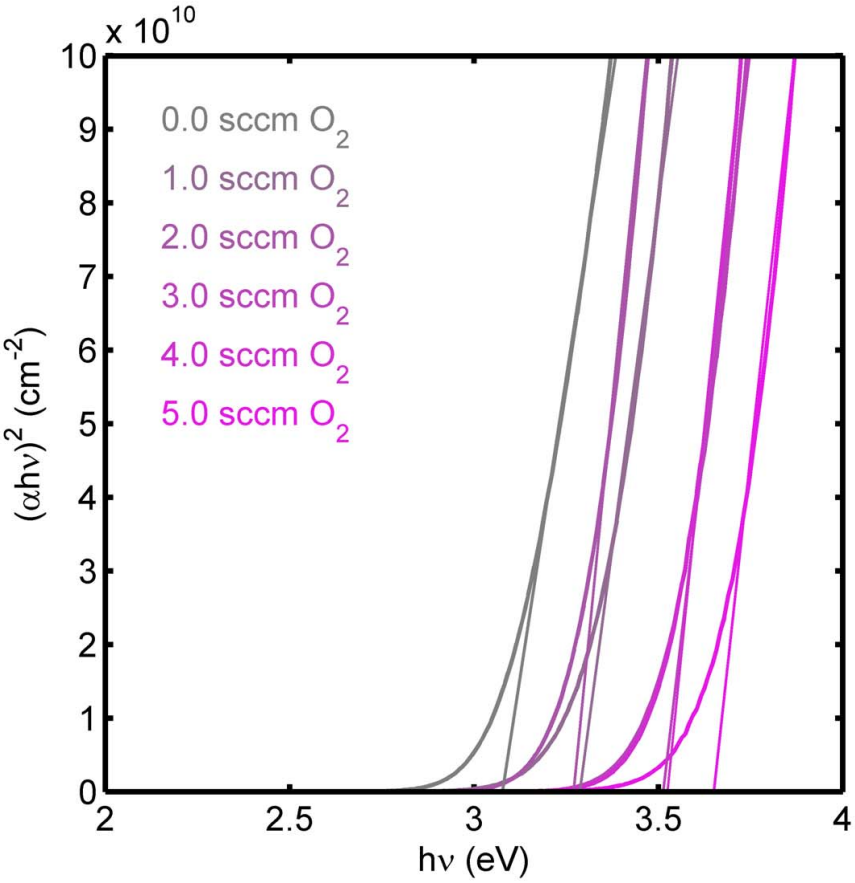

Figure 3.17: The Tauc plot was constructed from the absorption and thickness data according to the procedure outlined above. The linear regions have been fit with lines and extrapolated to zero to determine the material's band gap. Composition was not determined for these alloys, and thus O_2 flow rate during growth is used as a proxy for SO_4^{2-} content. Similarly to $Zn(S,SO_4)$, the band gap linearly expands with an increasing O_2 flow rate.

studied emitter material in Cu_2O. We believe this is due not only to the ease of deposition of zinc thin films, but also to the favorable properties listed above. Thus Zn-VI materials were grown in a number of different ways. ZnO and Zn(O,S) and related alloys were grown by sputter deposition, and ZnS and ZnSe were grown by molecular beam epitaxy. The optical, electronic, and structural characteristics were described by extensive analysis.

Chapter 4

Interface Stoichiometry Control in Zn-VI/Cu_2O Heterojunctions

One of the challenges to Cu_2O photovoltaic device fabrication is the reactivity of Cu_2O, which is a result of the material's small enthalpy of formation (ΔH_f^0 = -170.7 kJ/mol) [14]. The enthalpy of formation for Cu_2O is compared to the enthalpy of formation for most stable, solid oxide materials in Chapter 3 and also in Appendix A. After reviewing the enthalpy of formation data, it becomes obvious that Cu_2O will be reduced by nearly every elemental material. Indeed, the formation of copper at the Cu_2O heterojunction interface is a well understood phenomenon, and previous literature on the reduction of Cu_2O to Cu at interfaces will be reviewed later in the

chapter. However, copper is not the only material that can form at the Cu_2O interface as there is another stable phase of copper oxide: CuO [69]. The conditions in which CuO forms at the interface have not been explicitly studied previously.

In this chapter we will present work on the controlled modification of the Cu_2O surface stoichiometry by differing the ratio of Zn:O in the growth atmosphere. These results suggest an interesting mechanism by which the CuO surface layer on a Cu_2O wafer reacts with the deposited ZnO thin film according to the ratio of Zn:O in the deposition ambient. We demonstrate the ability to reproducibly tune the interface from O-rich, to stoichiometric, to Cu-rich solely by modifying the ratio of Zn:O in the growth atmosphere. We also studied the reaction chemistry of ZnSe, ZnS, and Zn(O,S) with Cu_2O [65].

The surface stoichiometry was primarily characterized by X-ray photoelectron spectroscopy (XPS), so we will provide an introduction to analysis of the Cu_2O surface by XPS. To put this work in the proper context, we will review the previous literature on the formation of reactive species at heterojunction and Schottky junction interfaces. Additionally, we will review previous literature on ex situ and in situ surface preparation, particularly methods that purport to give a phase pure, or stoichiometric, Cu_2O surface. All of this previous work highlights the importance of our research as a novel and highly reproducible method for the preparation of a stoichiometric Cu_2O interface.

4.1 Differentiating Cu, CuO, and Cu_2O by X-Ray Photoelectron Spectroscopy

X-ray photoelectron spectroscopy (XPS) is a surface sensitive characterization technique which provides information on the composition of a sample as well as the chemical bonding state of the sample's constituent atoms. In XPS the sample is inundated with X-rays, which elastically scatter both free and bound electrons from the sample. Signal from Auger scattering is detected as well. The escape depth of the electrons

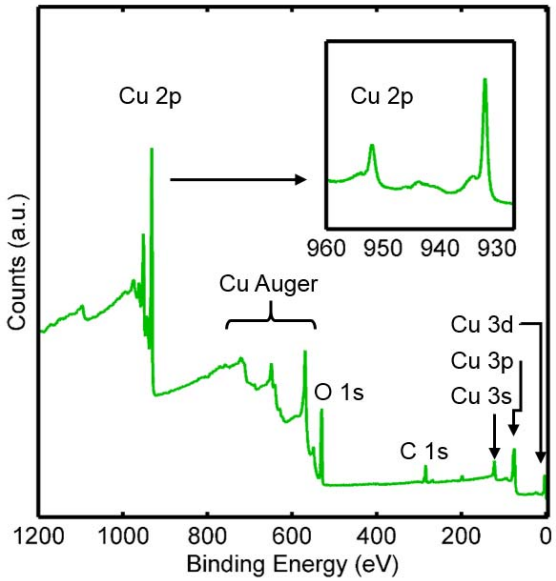

Figure 4.1: Typical low-resolution X-ray photoelectron spectroscopy data for Cu_2O is plotted in the main figure. The Cu 2p, Cu Auger, O1s, and low energy Cu peaks are labeled. The inset figure shows a typical high-resolution scan of the Cu 2p peak.

ranges from 1-10 nm depending on the properties of the sample. The number of scattered electrons at a particular energy is collected as a number of counts. This gives rise to a characteristic peak profile of counts versus binging energy for different elemental materials [61]. All XPS experiments detailed herein were performed using a Kratos Ultra XPS system. The sample chamber was maintained at $<2\times$10-9 Torr. The Al Kα line (1486.6 eV) was used as a monochromatic X-ray source and the excited photoelectrons were collected by a hemispherical analyzer at 0° from the surface normal. Low-resolution survey spectra were acquired between binding energies (B.E.) of 1–1200 eV. Higher-resolution, detailed scans (detection line width of $<$0.20 eV), were collected on individual XPS features of interest.

A typical low-resolution scan of Cu_2O is shown in Figure 4.1. The low-resolution spectra shows the general shape of a spectrum of an air-exposed Cu_2O surface. The main peaks we will be investigating are all labeled and are the Cu 2p, Cu Auger, O1s, and Cu 3s peaks. The peaks are named for the orbital the scattered electrons originate from. The electrons can also be scattered by an Auger process as opposed

to a direct process, giving rise to a series of Auger peaks. We will be looking at the main Auger peak, which we will simply refer to as Cu Auger. Most of the XPS spectra we will be looking at will be high-resolution scans of individual peaks like the Cu 2p inset in Figure 4.1. The Cu 2p peak is actually comprised of two peaks due to spin-orbit splitting. The smaller peak is the Cu $2p_{1/2}$ and the larger peak is the Cu $2p_{3/2}$. Both peaks contain the same information, so occasionally we will only look at the Cu $2p_{3/2}$ peak [15].

XPS is a particularly powerful technique for evaluating surfaces because the bonding state of the material can shift the peak positions, and thus high resolution scans of individual material peaks can give information about the chemical state of the constituent atoms. For example, the oxidation state of Cu can easily be assessed by XPS because the Cu 2p and the main Cu Auger peak undergo large peak shifts depending on the oxidation state of the sample. The XPS positions of the Cu 2p and Cu Auger peaks for several copper compounds have previously been reviewed by Chawla et. al. [15]. They found that CuO can be differentiated from Cu and Cu_2O by looking at the Cu 2p peak. If CuO is present, the Cu 2p peak shifts to a higher binding energy. Similarly, Cu can be differentiated from Cu_2O and CuO by observing the position of the Cu Auger peak. If elemental Cu is present, the peak shifts to a smaller binding energy. If the Cu 2p peak is sitting at a low energy position, and the Cu auger peak is high energy, then the material is Cu_2O. Thus, by looking at high resolution scans of these peaks, you can separate the concentrations of Cu atoms on the surface bound as elemental Cu, Cu_2O, and CuO. All of this information is summarized in Figure 4.2. which is copied from reference Chawla et al. [15].

We also measured a series of standard samples to confirm that we could resolve these peak shifts on our samples. Figure 4.3 shows high-resolution XPS spectra of an air-exposed Cu_2O surface and a Cu_2O surface that has been cleaved in situ and has never been exposed to air. The cleaved sample has a single low binding energy peak in the Cu 2p scan as well as a high binding energy Cu Auger peak. These are the relative peak positions we would expect for phase pure Cu_2O in XPS based on Figure 4.2. The air-exposed Cu_2O XPS data is slightly more complicated because Cu_2O

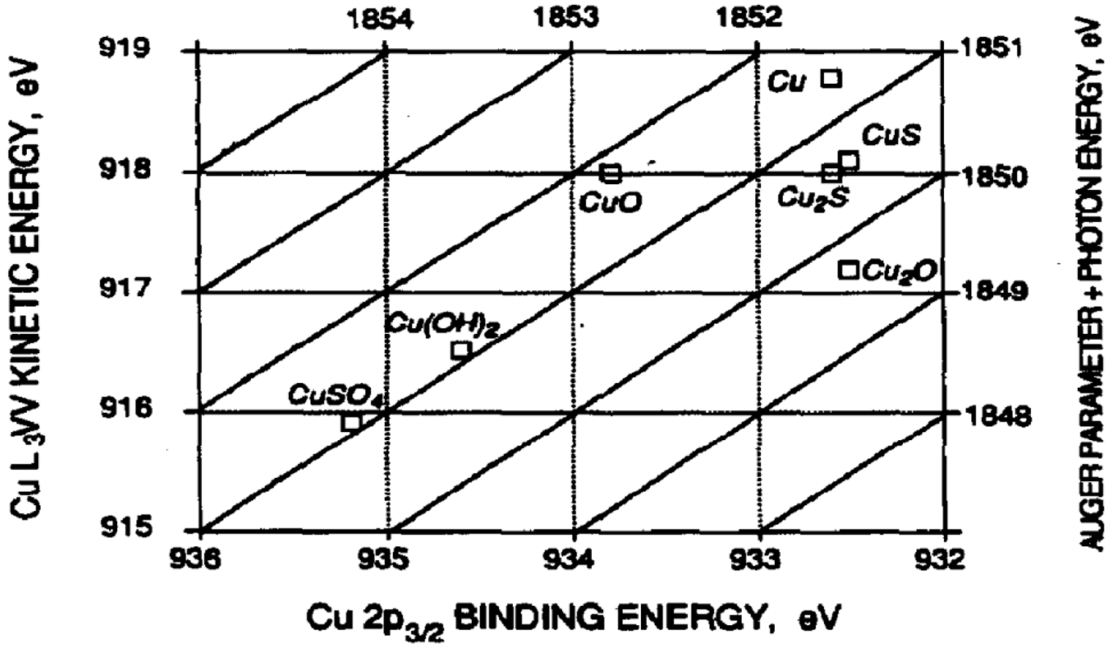

Figure 4.2: Chemical state plot for the Cu-O-S-H system copied from reference[15]. This plot describes the peak position for the Cu 2p and main Cu Auger peaks in both binding energy (or kinetic energy for Auger scattering) and total energy. Measuring the position of these two peaks is sufficient for differentiating most Cu-O-S-H compounds.

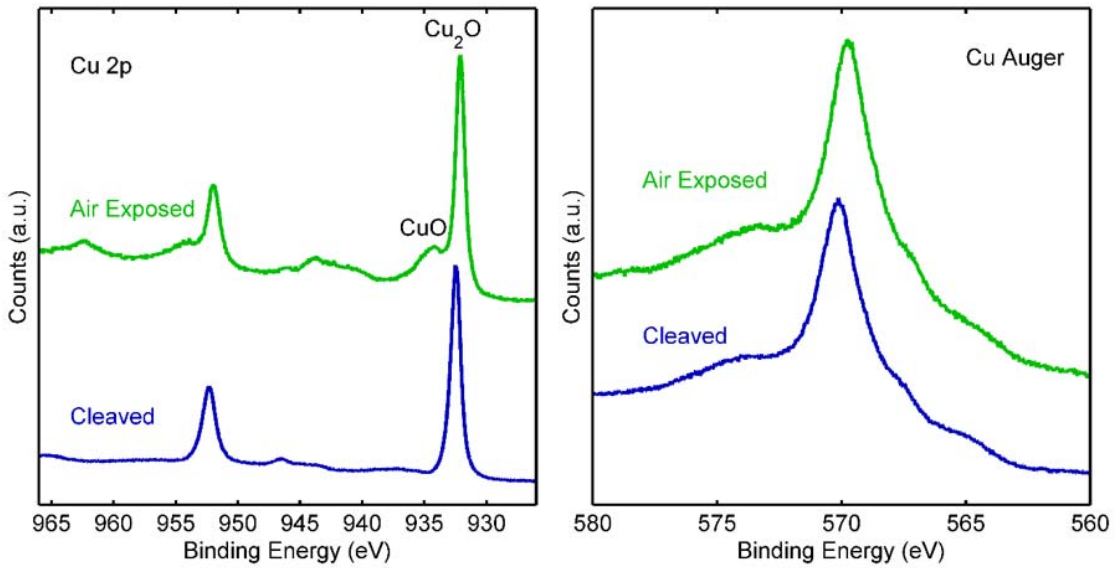

Figure 4.3: Comparison of surface of Cu_2O that has been exposed to air and the freshly exposed edge of a wafer cleaved in situ. The cleaved surface has never been exposed to air and shows no evidence of oxidation. This sample served as our standard for phase pure Cu_2O.

is not the stable phase of copper oxide at room temperature and pressure [69]. We would expect some formation of CuO on the surface even though Cu_2O is kinetically stable at room temperature and pressure [30]. Indeed, the shoulder in the Cu 2p peak of the air-exposed sample is evidence of the formation of another chemical bonding state of copper. We identify this shoulder as CuO due to the known peak location of CuO from Figure 4.2 and the expectation that the Cu_2O surface is oxidized due to air exposure. The Auger peak location for both samples is very similar, as CuO and Cu_2O have very similar Auger peak positions according to Figure 4.2. If Cu were present we would expect to see a secondary peak around 568 eV.

4.2 Literature Review of Reactions at Cu_2O Interfaces

There have been several previous studies characterizing reactions at the Cu_2O interface with both metal and semiconductor contacts. Olsen et al. [43] researched the interface of Cu_2O Schottky junctions to try to determine the cause of low barrier heights in junctions made with the low work function metals Yb, Mg, Al, Cu, Cr, Au, and Mn. They found Cu at the metal/Cu_2O interface in every case except with Au, which made nearly every device tested a Cu/Cu_2O device. The formation of Cu was found to cause the low barrier height of the Schottky devices due to the low barrier height of Cu/Cu_2O contacts. While the Au devices did not form Cu at the interface, the contact was ohmic in character as opposed to Schottky. The Cu content of the junctions was assessed by Auger surface analysis and sputter profiling.

Papadimitriou et al. [45] also conducted a study detailing the reactivity of Cu_2O with several common emitter materials, including In_2O_3, SnO_2, CdO, and ZnSe. The materials were deposited by sputtering or evaporation. Formation of species at the interface was assessed by Auger surface analysis. It was found that all reactions at the interface were enhanced by heating the sample during deposition. Additionally, the only sample that was found to not be reactive with Cu_2O was CdO. Given that the heat of formation of CdO is the smallest of the listed materials (see appendix A), it is not surprising that the interfacial reactions were minimal. The junction was probed by sputter etching of the heterojunction thin films.

Thus it is well known in the literature that there is reactivity at the Cu_2O heterojunction interface, but a method for controlling the reaction has not been suggested. Additionally, all previous studies involved sputter profiling of interfaces, which can confound chemical changes due to reactions at the interface with damage due to the sputter etching.

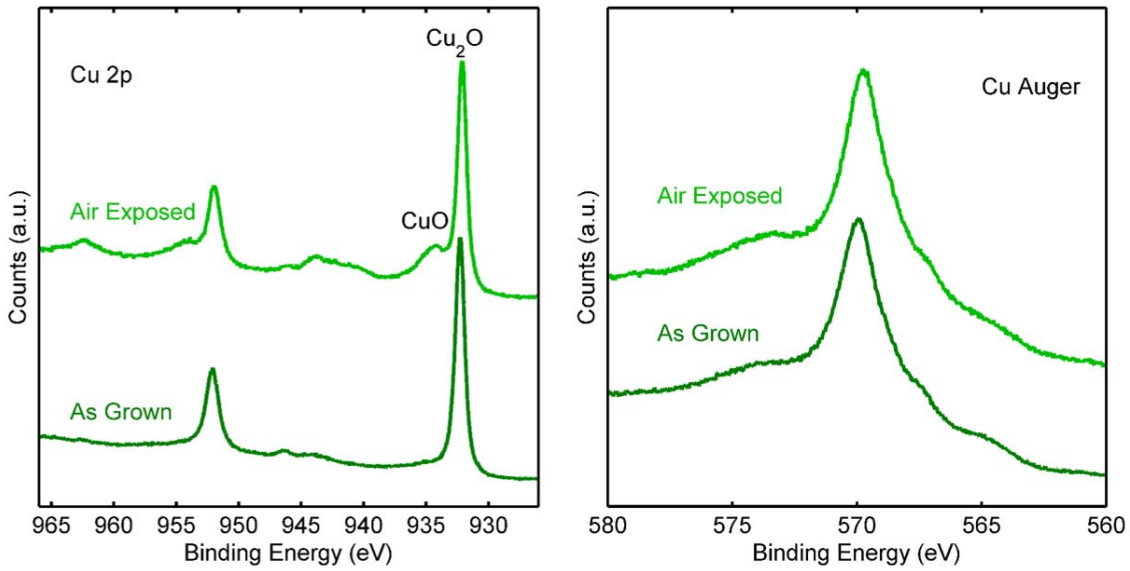

Figure 4.4: Comparison of surface of Cu_2O wafers directly from the furnace, or as-grown, and after ~1 week of air exposure. The coverage of CuO on the surface slowly increased with air exposure, and is the more relevant surface as most experiments could not be performed on freshly grown wafers.

4.3 Studies of Surface Preparation

Several surface preparation techniques for Cu_2O have been reported in literature. This section will review the surface preparation literature as well as provide an overview of our own attempts at surface preparation.

4.3.1 The As-Grown and Air-Exposed Surfaces

Before analyzing how to change the surface, I'll first review what the as-grown surface looks like. Figure 4.4 shows the surface both immediately from the furnace and after several days of exposure to air. It can be seen from the figure that the surface of the Cu_2O was nearly phase pure when directly from the furnace, but slowly grew a thicker layer of surface oxide when exposed to air. The growth of CuO is to be expected based on the phase diagram, which can be seen in Figure 2.1. Because of the impossibility of only experimenting with freshly made Cu_2O nearly all experiments were performed

on air-exposed Cu_2O. Thus most Cu_2O surface preparation revolves around removing the CuO layer from the surface.

4.3.2 The Nitric Acid Etch

The most commonly reported surface preparation in literature is a nitric acid etch or a hydrochloric acid etch followed by a nitric acid etch. In fact, we have tried this etch as well and have found variable results. The details of our work with a nitric acid etch at Caltech were published by C. Xiang et al. [67]. Using a precisely timed, dilute nitric acid etch we were not able to remove the surface oxide according to XPS. In fact according to the XPS data published by C. Xiang et al., there is actually more CuO on the surface of the as-grown samples shown in Figure 4.4. It would appear the nitric acid does not remove CuO, but rather slightly oxidizes the surface. However, we will show later in this chapter that a slightly oxidized surface can be used to make a high voltage device.

There is a long history of using nitric acid in the most efficient photovoltaic devices in Cu_2O literature [10, 42, 48]. A nitric acid etch is also used by Mittiga et al. [39] before the deposition of the emitter material. The device made was a ZnO/Cu_2O device with an efficiency of 2%, which was the world record at the time. Additionally, this practice of using nitric acid as an etchant was first used to make the a high efficiency solar cell by Olsen et al. [42] in the 1970's.

4.3.3 Ammonium Persulfate as a Final Etch Step

The surface preparation of Minami et. al. [36, 37, 38] was reported in private correspondence as follows:

1. $FeCl_3$ + H_2O
2. HNO_3 + NaCl
3. $(NH_4)_2S_2O_8$ + H_2O

This procedure is unique because the final treatment is with ammonium persulfate (APS) diluted in water. Additionally the Minami et al. reports the highest efficiency

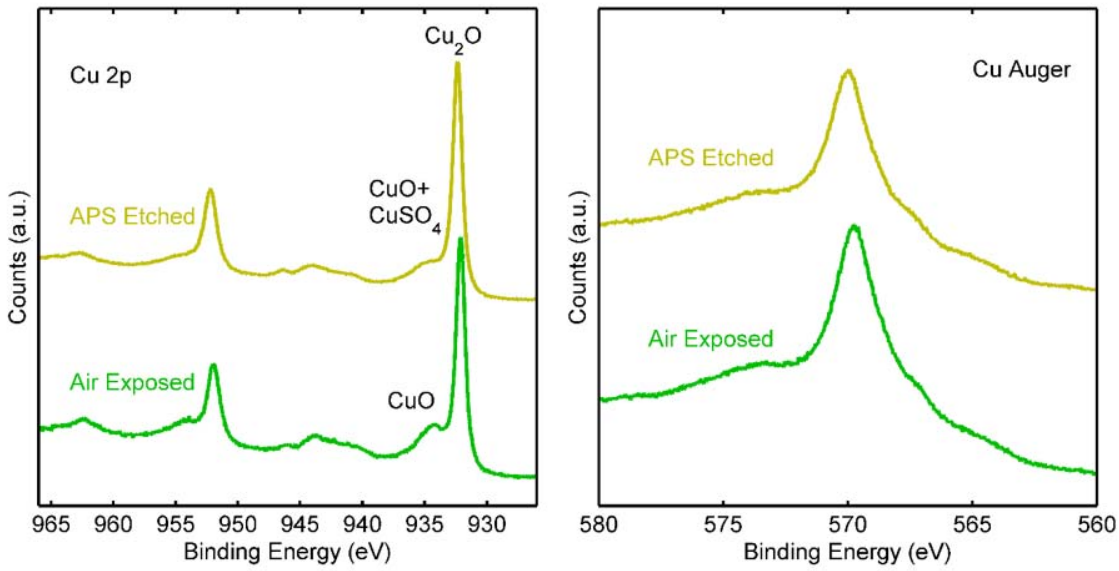

Figure 4.5: Comparison of surface of Cu_2O wafers after exposure to air, and air-exposed wafers that have been etched in APS. Formation of $CuSO_4$ is evident from the broadened shoulder on the Cu_2O peak. No formation of Cu is evident in the Auger data.

Cu_2O devices currently [37], so the surface preparation they use is worth additional study. APS is primarily used as a chlorine free alternative to $FeCl_3$ for Cu etching. Cu_2O is highly reactive with chlorine [10, 11], thus this etch step is probably necessary for removing the chlorine left by the previous etch in $FeCl_3$. We did our own evaluation of APS as a Cu_2O etchant by XPS. We made a solution of 1% APS by volume in water and etched the air-exposed Cu_2O wafers for 60 sec while stirring continuously. The wafers were then thoroughly rinsed in water and dried under a nitrogen flow. The Cu 2p and Cu Auger data are shown in Figure 4.5 and the S 2p data is shown in Figure 4.6 . It is evident from the Cu 2p data that the APS did not remove the surface oxide. In fact, it appears to have reacted with the surface and formed $CuSO_4$. Additionally, the shape of the shoulder has changed to be broader and flatter. According to Figure 4.2, CuO and $CuSO_4$ will both have a higher binding energy peak then Cu_2O, thus the shape change of the shoulder is most likely due to the formation of $CuSO_4$. The presence of $CuSO_4$ is corroborated by the high binding energy S 2p peak.

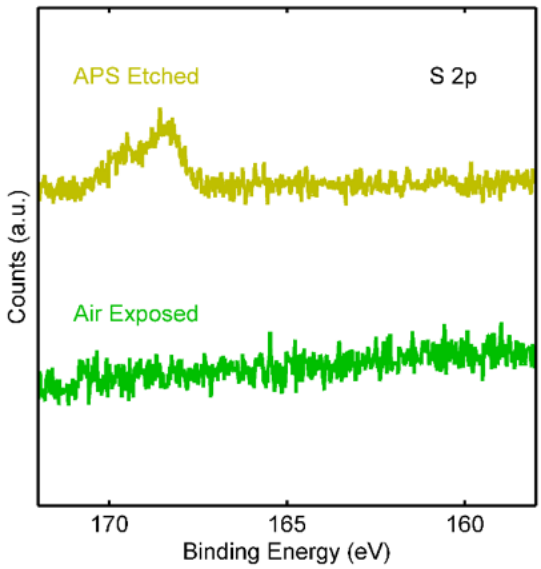

Figure 4.6: Comparison of surface of Cu_2O wafers after exposure to air and air-exposed wafers that have been etched in APS. Formation of $CuSO_4$ is evident from the high binding energy S 2p peak.

4.3.4 Annealing Cu_2O in Vacuum to Remove Surface CuO

We also attempted to remove the CuO from the surface by annealing in vacuum. These studies were conducted using an in situ heating element in the XPS. The samples were ramped up to 200 °C, 400 °C or 600 °C at a rate of 30 °C/min. The samples were then annealed at the set temperature for 1 hour and then ramped back to room temperature at the same rate. The samples could then be moved into the analysis chamber of the XPS without breaking vacuum. The Cu 2p and Cu Auger peaks are shown in Figure 4.7 . The Cu 2p peaks lose the shoulder characteristic of CuO at every anneal temperature including 200 °C. The Auger peaks show no evidence of Cu formation. Thus annealing is the only surface preparation in which we successfully created stoichiometric surfaces.

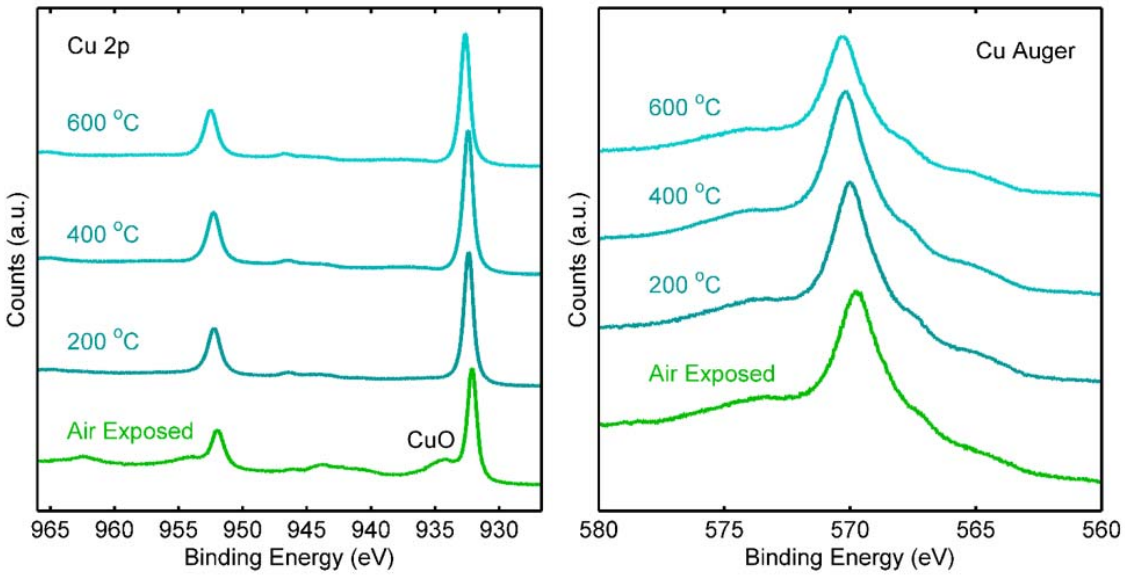

Figure 4.7: Comparison of surface of Cu_2O wafers after air exposure and annealing in vacuum at the indicated temperature. After annealing at each temperature the CuO was reduced and the Cu_2O wafer was left with a stoichiometric interface.

4.3.5 Summary of Surface Preparation

In this section we reviewed our work on chemical surface preparation as well as some of the relevant literature, particularly surface preparations used for high efficiency Cu_2O devices. We reviewed the effects of air exposure, nitric acid etching, APS etching, and annealing in vacuum. Both air exposure and the nitric acid etch leave the surface slightly oxidized, as CuO is evident in XPS measurements. This is interesting because nitric acid is the most widely reported surface preparation step in Cu_2O literature, and it does not leave a stoichiometric Cu_2O surface. APS, the final etch step used on the most efficient reported photovoltaics devices, not only left the surface oxidized, but also left $CuSO_4$ on the surface. The only surface preparation step that resulted in a stoichiometric surface was annealing in vacuum, for which temperatures from 200 °C through 600 °C left a pristine surface.

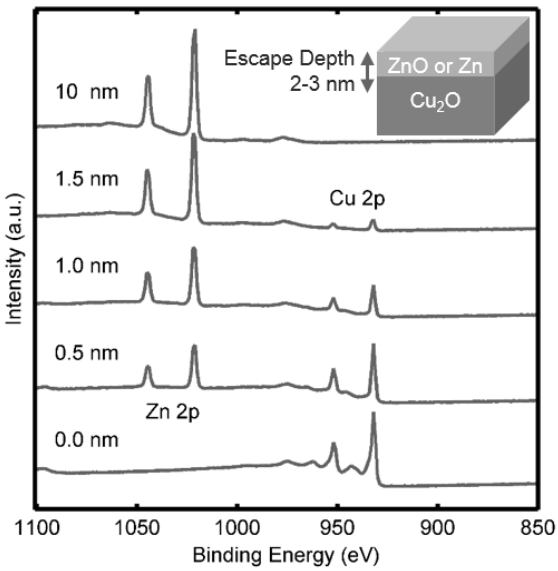

Figure 4.8: X-ray photoelectron spectroscopy of ZnO/Cu_2O heterojunctions for indicated thickness of ZnO. Both Cu and Zn peaks are visible, meaning the interface is being effectively probed.

4.4 Analysis of Thin ZnO/Cu_2O Heterostructures by X-ray Photoelectron Spectroscopy

Now that we have reviewed relevant surface treatments, we will go on to studying interfaces. XPS is known primarily as a surface technique, but if thin films are confined to less than the escape depth of the electrons, which can range from 1-10 nanometers, then interfaces can be observed as well.

4.4.1 ZnO/Cu_2O Interfaces Made with Air-Exposed Cu_2O

XPS survey scans of several thickness of ZnO on Cu_2O are shown in Figure 4.8 . Both the Zn 2p and Cu 2p peaks are visible, thus we are successfully analyzing the interface of the ZnO/Cu_2O heterostructures. The ZnO or Zn was deposited by sputter deposition, the details of which are described in Chapter 3.

High-resolution XPS scans of these samples are shown in Figure 4.9 . All Cu_2O used for the thin heterojunctions in Figure 4.9 was exposed to air. The heterojunc-

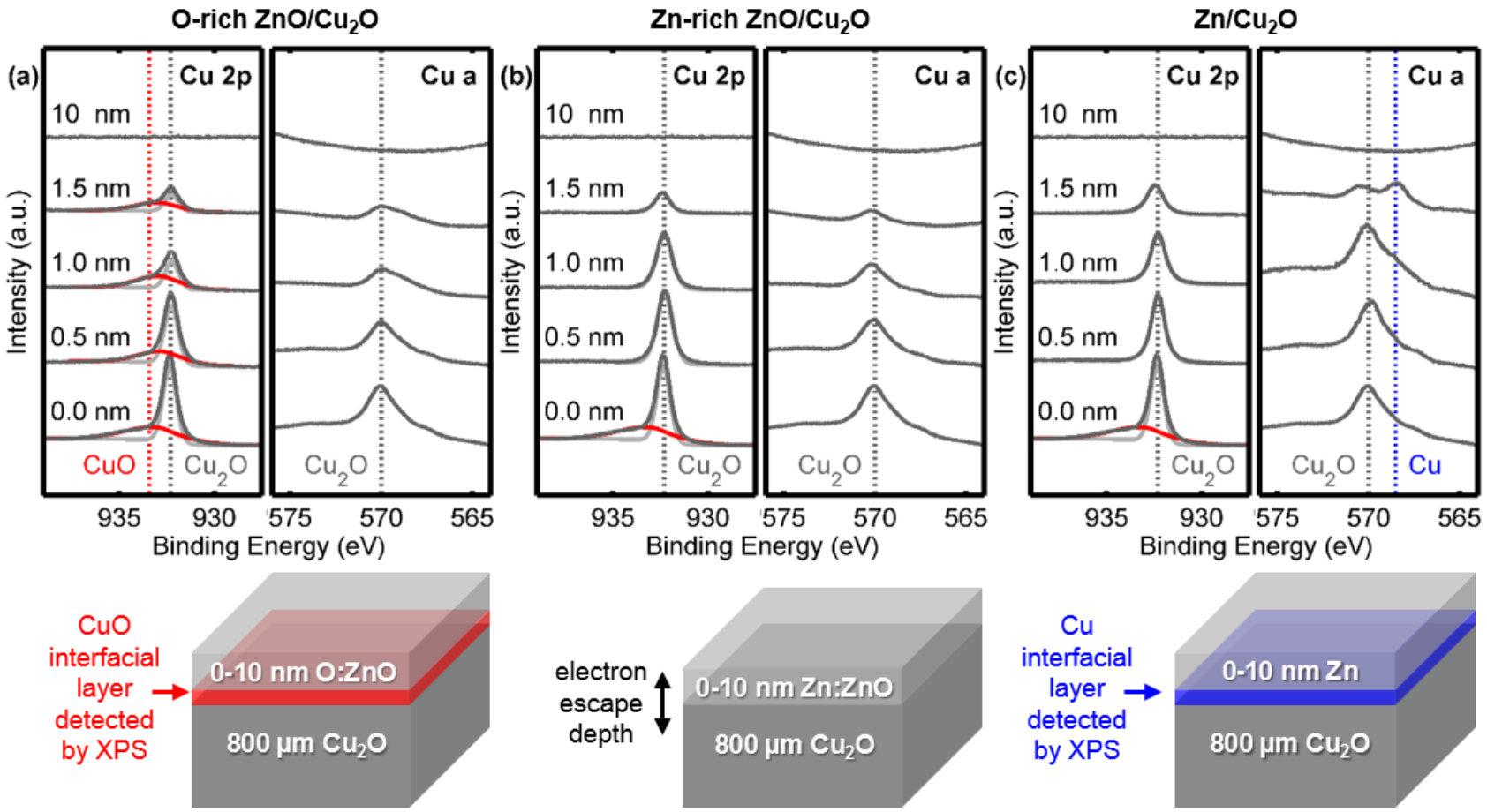

Figure 4.9: High-resolution X-ray photoelectron spectroscopy of the Cu $2p_{3/2}$ and main Cu Auger peak for Cu_2O heterointerfaces made with (a) O-rich ZnO, (b) Zn-rich ZnO, and (c) elemental Zn. The thickness of the deposited ZnO or Zn is indicated. The heterojunctions made with Zn-rich ZnO have a stoichiometric interface while the samples made with O-rich ZnO and Zn have CuO and Cu present, respectively. The schematics show our interpretation of the structure of the samples.

tions are made with various thicknesses of (Fig. 4.9a) O-rich ZnO, (Fig. 4.9b), Zn-rich ZnO, or (Fig. 4.9c) elemental Zn. The XPS spectra for the bare Cu_2O wafer (0.0 nm) shows a shoulder in the Cu 2p peak in all samples, consistent with air-exposed samples measured previously. As mentioned above, this surface oxide is expected. When O-rich ZnO is deposited onto the slightly oxidized Cu_2O surface (Fig. 4.9a), the shoulder in the Cu 2p peak continues through all thicknesses of ZnO. This result is expected since O-rich ZnO should have no elemental Zn available to react with the surface of the Cu_2O. Thus by depositing O-rich ZnO directly onto the slightly oxidized Cu_2O surface, we can produce a mixed phase surface with both CuO and Cu_2O.

When Zn-rich ZnO is deposited instead of O-rich ZnO (Fig 4.9b) we expect the wafer surface to be reduced due to the availability of elemental Zn. The data shows that as Zn-rich ZnO is deposited onto Cu_2O the shoulder in the Cu 2p peak disappears, indicating that the CuO layer is reduced. Furthermore, analysis of the Cu Auger peak shows no Cu_2O is reduced since no low binding energy peak is present, thus the reaction terminates at the Cu_2O surface. The reaction appears to be highly selective, which could be due to the slightly higher formation enthalpy (ΔH_f^0) of Cu_2O versus CuO[chase]. Additionally, the activation energy for the reduction of Cu_2O is twice that of CuO [30], thus kinetics may also play a role in terminating the reaction at Cu_2O. This selective reduction was also found to be highly reproducible and all deposited thicknesses showed the same trend. Thus depositing Zn-rich ZnO onto a slightly oxidized Cu_2O surface yields a stoichiometric ZnO/Cu_2O interface.

Elemental Cu was formed at the interface by sputtering elemental Zn onto Cu_2O (Fig 4.9c) because it was found to be impossible to reduce Cu_2O to Cu by sputtering ZnO alone. This is probably due to the low thermodynamic driving force for Zn to reduce Cu_2O, as ZnO also has a fairly low enthalpy of formation [14]. The Cu 2p data shows that Zn, similarly to Zn-rich ZnO, reduces the CuO on the surface. However, the Cu Auger peak shows a second lower binding energy peak, indicating Cu is forming at the interface.

Therefore, solely by altering the partial pressures of Zn and O_2 during deposition,

we were able to create Cu_2O heterointerfaces that were stoichiometric, or had elemental Cu or CuO present at the interface. Additionally, the process window in which a stoichiometric interface forms appears to be large, as it was difficult to actually find conditions in which non-ideal interfaces were created. For example, in order to reduce the surface to copper, we had to sputter elemental Zn.

4.4.2 ZnO/Cu_2O Interfaces Made with Annealed Cu_2O

We also studied ZnO deposited onto Cu_2O that had been annealed in situ in order to compare deposition onto substrates with and without CuO on the surface. The samples were annealed in the sputter chamber under vacuum of 10^{-7} Torr. The Cu_2O wafers were ramped to 600 °C at 30 °C/min and annealed at the set point for 1 hour. The samples were then cooled to room temperature under vacuum. ZnO was deposited on the Cu_2O wafers under different ambient O_2 pressures. The results of this study are shown in Figure 4.10 . When the CuO layer was removed from the surface by annealing, the same conditions that led to stoichiometric interfaces in the previous study led to reduced interfaces with Cu present. The conditions labeled as "Zn-rich ZnO/Cu_2O" in Figure 4.9 are identical to those labeled "0.00 mTorr O_2" in Figure 4.10. As the partial pressure of O_2 is increased in the deposition ambient, the interface becomes more stoichiometric. This is also in contrast to previous studies with air-exposed Cu_2O. The ZnO deposition conditions labeled "0.25 mTorr O_2" in Figure 4.10 are identical to the ZnO deposition conditions labeled "O-rich" in Figure 4.9. O-rich deposition conditions for ZnO leave CuO at the interface when using an air-exposed sample. However, the same O-rich deposition conditions leave a stoichiometric interface when using an in situ annealed sample.

We also looked at the differentiated Cu Auger data in order to more clearly resolve the presence of reactively formed Cu. In Figure 4.11 we directly compare the differentiated data from ZnO/Cu_2O interfaces made from Cu_2O with and without a surface layer of CuO. It can be seen clearly that no Cu forms in interfaces that begin with some CuO. However, Cu is present in the interfaces without CuO until

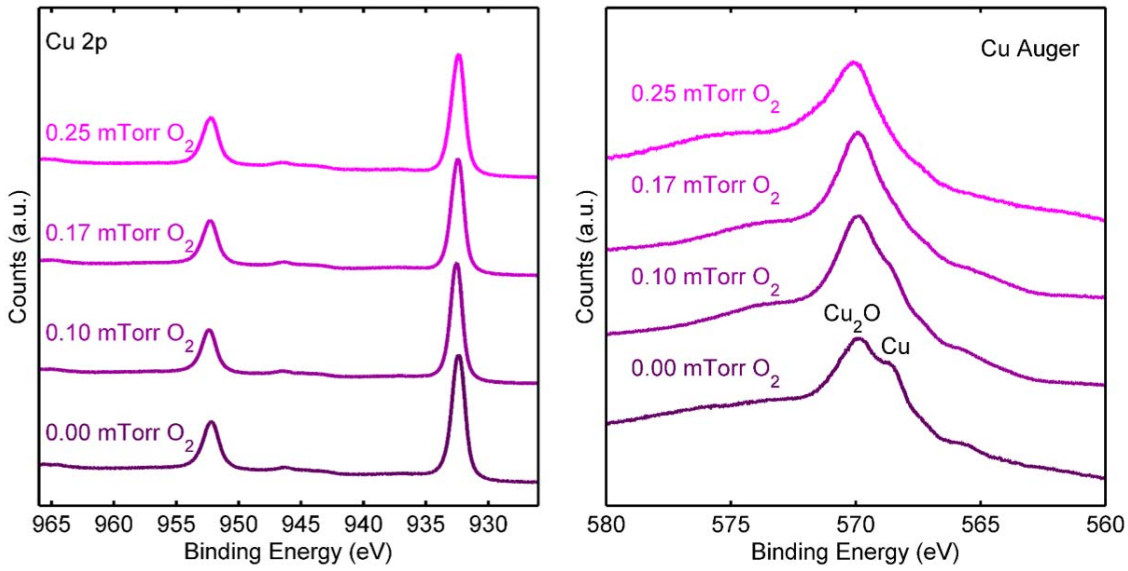

Figure 4.10: High-resolution X-ray photoelectron spectroscopy of the Cu 2p and main Cu Auger peak for ZnO/Cu_2O heterointerfaces made on Cu_2O annealed at 600 °C. The O_2 partial pressure during ZnO sputter deposition is indicated. Zn-rich ZnO conditions (0.0 mTorr O_2) led to Cu at the interface in contrast with results from heterojunctions made with air-exposed Cu_2O.

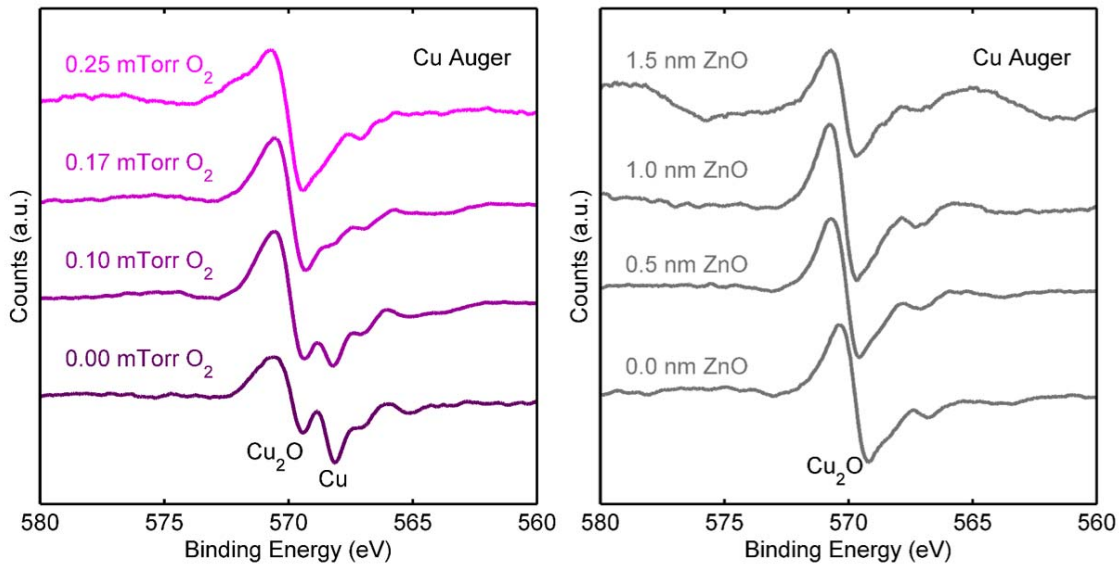

Figure 4.11: Differentiated spectra of high-resolution X-ray photoelectron spectroscopy of the main Cu Auger peak for ZnO/Cu_2O heterointerfaces. The junctions on the left are made on Cu_2O annealed at 600 °C. The ZnO/ Cu_2O junctions on the right are made with air-exposed Cu_2O. O_2 partial pressure during ZnO sputter deposition is indicated on the left with ZnO thickness fixed at ~ 1 nm. Thickness of ZnO on the right is indicated with Zn-rich ZnO conditions (0.00 mTorr O_2) being used for all thicknesses. Cu is only completely removed from the interface when the O_2 partial pressure reaches 0.25 mTorr. There is no Cu present in the right for all thicknesses.

reaching an O_2 partial pressure of 0.25 mTorr. The very conditions that lead to CuO remaining at the interface, labeled "O-rich" conditions in the previous section, leave a pristine interface when there is no CuO on the surface. This is significant because for both cases, the so-called O-rich conditions represent the pressure of O_2 you have to achieve for the deposited ZnO to not react with the surface. Essentially this is the pressure at which there is no Zn available to react with CuO or Cu_2O.

4.4.3 Conclusions from Study of ZnO/Cu_2 Interfaces

The ZnO thin films were sputtered on to Cu_2O using two different surface preparations: the air-exposed surface and the annealed surface. We found that stoichiometric interface formation was so simple as to be nearly unintentional when we were using the air-exposed Cu_2O surface. This is in contrast to the more difficult formation of stoichiometric interfaces when using the annealed interfaces. Indeed, when the CuO is removed from the surface, the same conditions that lead to perfect interfaces then lead to Cu formation at the ZnO/Cu_2O heterojunction. We concluded from this that the presence of some CuO on the surface before heterojunction deposition is actually not only beneficial, but necessary in some deposition conditions. These results also give us some insight into the reported surface preparation techniques used in the highest efficiency Cu_2O devices in literature. Both nitric acid etching and APS etching left CuO or $CuSO_4$ on the surface. Given our results that some CuO on the surface can lead to stoichiometric interface formation, it is not surprising that these surface preparations lead to the highest efficiency devices. Some amount of CuO on the surface seems to facilitate stoichiometric interface formation.

4.5 Analysis of MBE Grown ZnS and ZnSe

The stoichiometry at the interface of the MBE grown ZnS/Cu_2O, the MBE grown ZnSe/Cu_2O, as well as the sputtered ZnO/Cu_2O were investigated. The results for are compared in Figure 4.12 . The growth of ZnSe and ZnS by MBE is discussed in detail Chapter 3, and the Cu_2O used was exposed to air and untreated. The

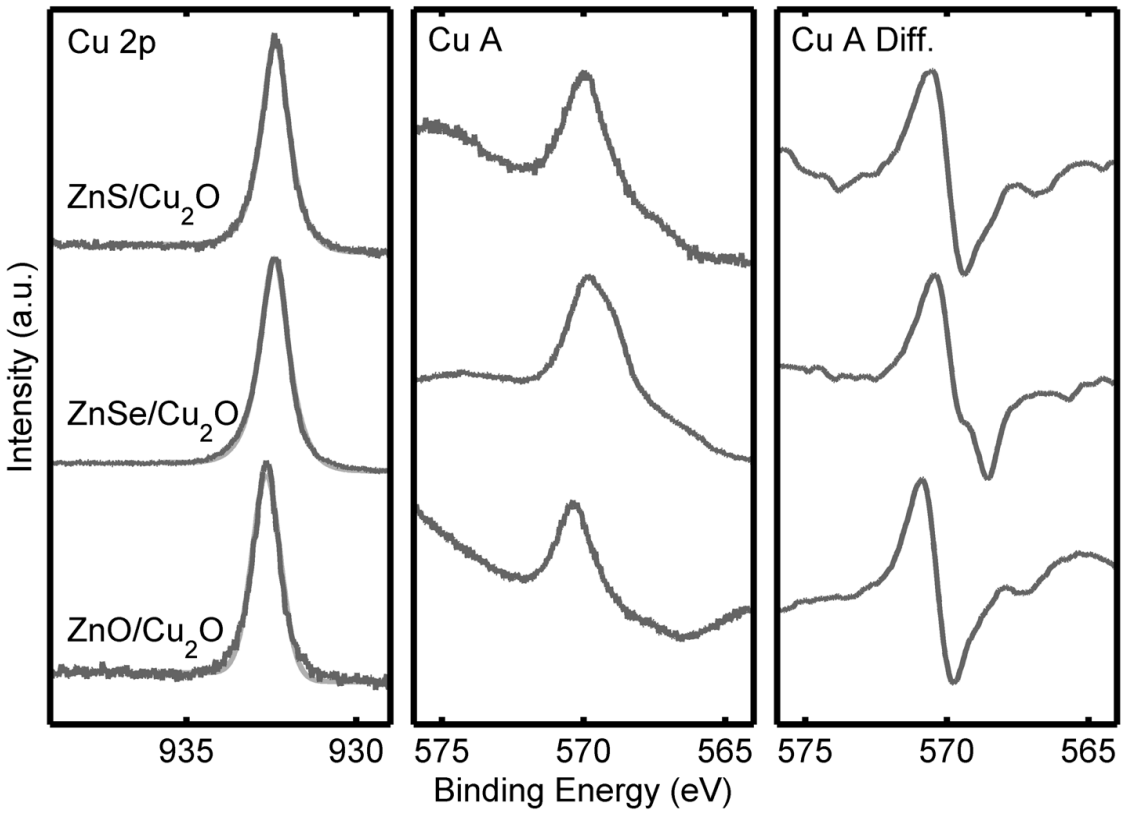

Figure 4.12: High-resolution X-ray photoelectron spectroscopy of the Cu $2p_{3/2}$ and main Cu Auger peak for Zn-VI/Cu_2O heterointerfaces made on air-exposed Cu_2O. The composition of the Zn-VI/Cu_2O heterojunction is indicated. Both the ZnO/Cu_2O and ZnS/Cu_2O interfaces look stoichiometric. The ZnSe/Cu_2O interface shows evidence of a reaction in the differentiated Cu Auger data.

Material	Enthalpy of Formation (kJ/mol)
Cu_2O	-168.6
CuO	-157.3
$CuSO_4$	-771.4
CuS	-53.1
Cu_2S	-79.5
ZnO	-350.5
$ZnSO_4$	-980.1
ZnS	-192.6

Table 4.1: List of enthalpy of formation for all common Cu-O-S and Zn-O-S compounds[14]. $ZnSO_4$is the most likely to form based on the values given, which is likely why Cu_2O does not react with ZnS.

ZnO/Cu_2O interface is made by sputtering ZnO onto air-exposed Cu_2O in Zn-rich conditions. ZnS shows very similar reactivity to ZnO, and is why we believe Zn(O,S) is an eligible emitter material. ZnSe also reduced the CuO at the interface, but the Cu Auger peak shows the formation of another species of bonded copper. We are unable to deduce which phase of copper formed, but is most likely Cu_2Se. The heats of formation for the different possible Zn-O-S and Cu-O-S species are listed in Table 4.1.

4.6 Analysis of Sputtered Zn(O,S)/Cu_2O Heterojunctions

Thin Zn(O,S) was sputtered onto air-exposed Cu_2O wafers according to the parameters outlined in the Chapter. A composition of $ZnO_{0.21}S_{0.79}$ was used to make the thin heterostructures for the work shown in Figure 4.13 . It is evident from analysis

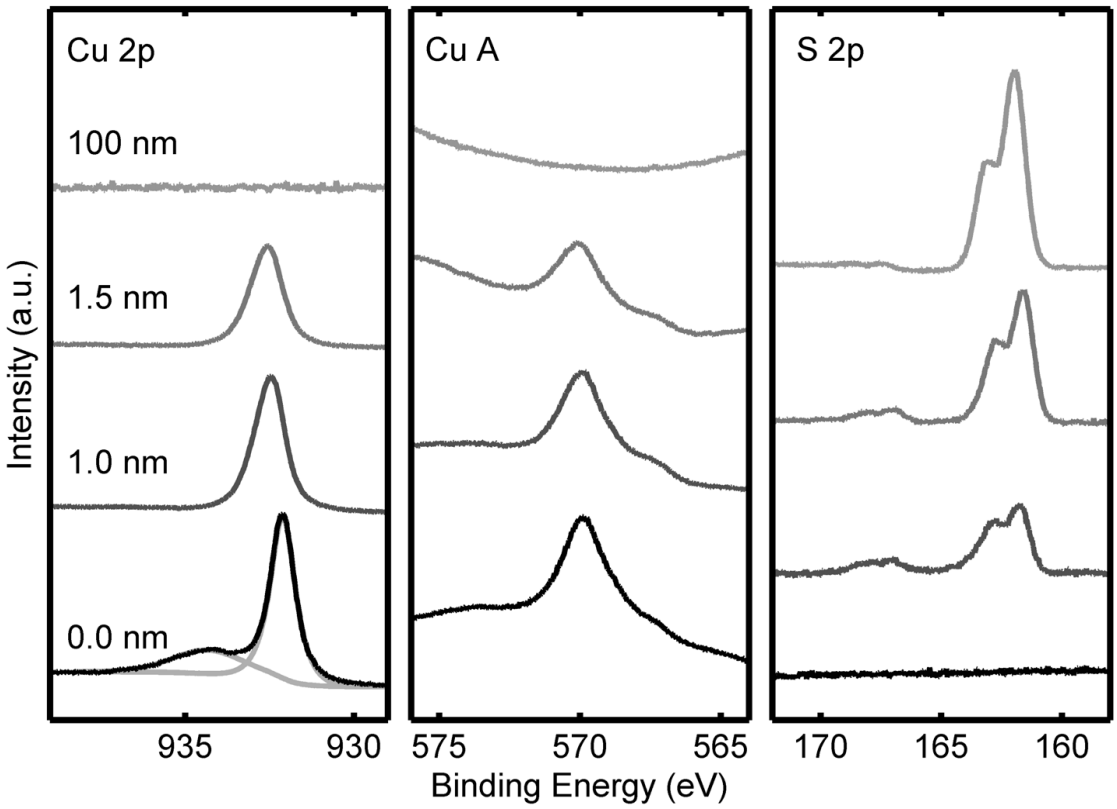

Figure 4.13: High-resolution X-ray photoelectron spectroscopy of the Cu $2p_{3/2}$, main Cu Auger peak, and S 2p peak for Zn(O,S)/Cu_2O heterointerfaces made on air-exposed Cu_2O. The thickness of Zn(O,S) on Cu_2O is indicated. The Cu_2O looks stoichiometric at the interface, but the S 2p peak indicates the formation of SO_4^{-2}. Thus there is likely formation of $ZnSO_4$ at the interface.

of the Cu 2p and Cu Auger peaks that the Cu_2O at the interface is stoichiometric, as we would expect given the previous results for the ZnO/Cu_2O interface and the ZnS/Cu_2O interface. However, the interface chemistry can no longer be fully understood solely by analyzing the Cu peaks. There are some additional interesting features of this interface due to the fact that the emitter no longer only has one possible phase. With the addition of sulfur to the ZnO, the number of phases possible in the emitter at the interface greatly increases (see Table 4.1). As we described before, we believe that excess reducing species in the deposition ambient, such as elemental Zn, react with the surface. With the addition of sulfur, the species that can be formed include ZnO, $ZnSO_4$, and ZnS. We have previously shown that the ratio of SO_4^{2-} to S^{-2} in the deposited material greatly affects its optical properties. Given that the deposited material at the interface must be reacting with a large amount of oxygen, it is important to understand what species is forming at the interface. Thus we also analyzed the S 2p peaks for the thin Zn(O,S) heterostructures on Cu_2O. There is evidence of SO_4^{2-} formation close to the interface. Because we see no shoulders in the Cu 2p and Cu Auger data, we know $CuSO_4$ is not forming [15], therefore it must be $ZnSO_4$ at the interface. From optical studies detailed in Chapter 3, we know formation of $Zn(SO_4)$ as opposed to ZnS increases the band gap of the material. Thus we expect some band bending effects right at the interface due to the change in band gaps.

4.7 Development of a Novel Surface Preparation Technique

Cu_2O is a uniquely reactive semiconductor due in part to its low enthalpy of formation. Most wafer based solar cells have ex situ surface preparation steps that remove surface oxides and impurities before the formation of a heterojunction. However, we could find no suitable heterojunction partner that was not reactive with the surface. Additionally, removal of the surface oxide through techniques such as annealing actually lead to an enhancement of reduction of the Cu_2O surface. The Cu_2O that

was air-exposed and was untreated still reproducibly resulted in stoichiometric interfaces under certain heterojunction deposition conditions. It seems that the slight abundance of reducing materials such as elemental Zn in the deposition atmosphere leads to a preferential reaction with the CuO on the surface. This chemistry is highly reproducible. Therefore we believe that though surface cleaning will probably be a necessary step for removing impurities on the sample surface. The ideal surface preparation would result in a slightly oxidized layer on the surface, at least when making an interface with a Zn compound. Additionally ZnS and Zn(O,S) formed stoichiometric interfaces when sputtered onto slightly oxidized Cu_2O.

Chapter 5

Valence Band Offset Measurements by X-ray Photoelectron Spectroscopy

Cu_2O has an unusually small electron affinity at 3.2 eV [59]. This means that Cu_2O will form a "conduction band cliff" with most common heterojunction materials. A conduction band cliff defines an energy band alignment in which the valence band offset between the two materials is extremely negative. This alignment limits device voltage by providing a low barrier recombination path for carriers and limiting the possible work function difference between the two materials [18]. The physical link between band alignment and device efficiency will be further elucidated in Chapter 6. Thus band alignment must be evaluated when considering a material's suitability

as a heterojunction partner. Traditionally this is done by building an Anderson band diagram based on the bulk properties of the two materials forming the junction [5]. However, this bulk model fails to capture the chemical and physical nuances of interface formation and often results in a non-physical alignment [18].

We have instead endeavored to measure rather than model the band alignment between Cu_2O and several Zn-VI materials, including ZnO, ZnS, and ZnSe. Kraut et al. [31] proposed a method in 1980 by which X-ray photoelectron spectroscopy (XPS) can be used to measure the valence band offset at an interface. We have performed valence band offset measurements by XPS for Zn-VI/Cu_2O interfaces in order to evaluate the suitability of each Zn-VI material for use in Cu_2O photovoltaic devices. Both the deposition of ZnS and ZnSe and the analysis of the valence band data was done in collaboration with Jeff Bosco.

5.1 Heterojunction Alignment by Anderson's Rule

New students to device physics are always taught to draw heterojunction band alignments in using Anderson's rule, also known as the electron affinity rule [5]. This method describes a way understand the energy band alignment of two materials simply by comparing the electron affinities (χ) of the two bulk materials, where electron affinity is defined as the energy required to remove an electron from the conduction band. An example of an Anderson band alignment for bulk ZnO and Cu_2O is given in Figure 5.1. In this method the conduction band offset (ΔE_C) and valence band offset (ΔE_V) are defined by the bulk electron affinity (χ) and the band gaps (E_g) of the two materials. The work function (φ) of the two materials, defined as the distance from the Fermi level to vacuum, is also indicated.

However, as we shall show shortly, alignment at real semiconductor interfaces is never so simple. There are physical and chemical effects at an interface that can change the energy band alignment between two materials. Charged impurities or defects at the interface can modify the band alignment by effecting the interface dipole. Strain in the lattice at the interface due to differences in crystal structure

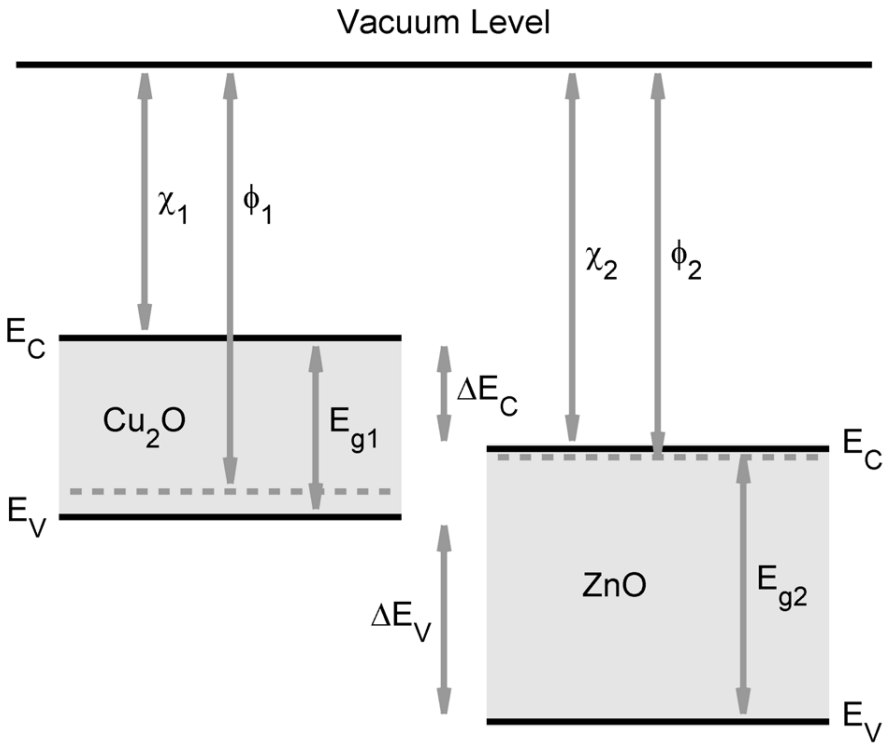

χ_1	3.2 eV	χ_2	4.5 eV
φ_1	4.0 eV	φ_2	4.6 eV
E_{g1}	2.1 eV	E_{g2}	3.2 eV

ΔE_V	-2.4 eV
ΔE_C	-1.3 eV

Figure 5.1: Alignment of bulk Cu_2O and ZnO energy bands as defined by the Anderson band alignment procedure. In this procedure the conduction band offset (ΔE_C) and valence band offset (ΔE_V) are defined by the bulk electron affinity (χ) and the band gaps of the two materials[59, 27].

between the two heterojunction materials can also shift band alignment. In order to accurately determine the band structure, the band offset must be measured [18]. We will describe our method for measuring the valence band offset in the next section.

5.2 Measurement of Valence Band Offset Via the Kraut Method

The "Kraut Method" was first proposed by Kraut et al. in 1980 as a method for measuring the valence band offset experimentally [31]. It involves a series of X-Ray photoelectron spectroscopy (XPS) experiments with both bulk and thin film samples which attempt to solve the following equation:

$$\Delta E_V = \left(E_{CL}^{ZnO} - E_{VB}^{ZnO}\right) - \left(E_{CL}^{Cu_2O} - E_{VB}^{Cu_2O}\right) - \left(E_{CL}^{ZnO} - E_{CL}^{Cu_2O}\right)$$

The goal is to measure the difference in valence band edge between the two materials. The first step is measuring the valence band to "core-level" split for the two bulk materials, or $\left(E_{CL}^{ZnO} - E_{VB}^{ZnO}\right)$and $\left(E_{CL}^{Cu_2O} - E_{VB}^{Cu_2O}\right)$ in the equation above. A core-level is any XPS peak that is a result of emission from a localized electron. When analyzing the ZnO/Cu_2O interface we looked at the Zn 3s peak for ZnO and the Cu 3s peak for Cu_2O. Thus the binding energy difference from the Zn 3s peak to the valence band edge was measured for ZnO and for Cu_2O we measured the energy difference from the Cu 3s peak to the valence band edge. The valence band edge for the bulk materials was determined by convoluting the calculated valence band density of states with the instrument broadening function and then fitting the convoluted function to the measured valence band data.

Once the bulk valence band to core level values are known, a series of heterojunctions are measured to determine the core-level to core-level split at the heterointerface, or $\left(E_{CL}^{ZnO} - E_{CL}^{Cu_2O}\right)$, from the equation above. Because XPS is very surface sensitive, the thickness of the heterojunction must be restricted to less then a few nanometers. Several thicknesses of heterojunction are always used to asses whether or not there

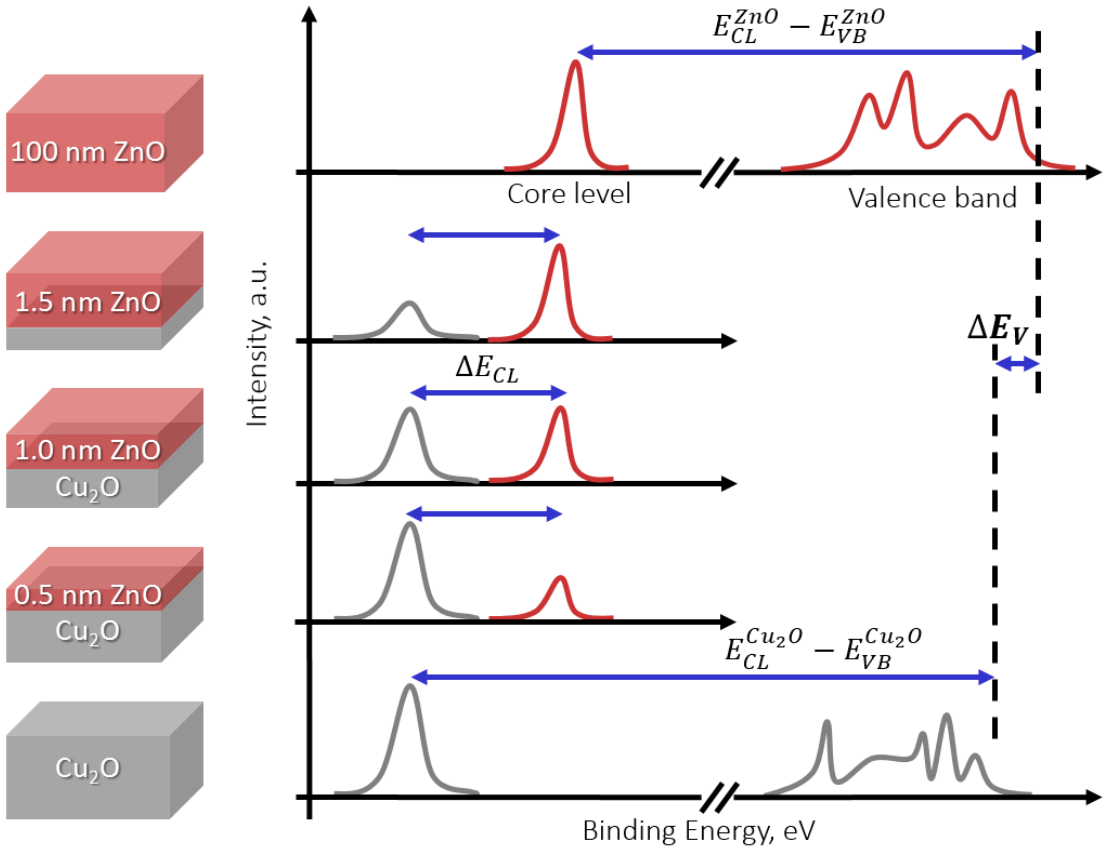

Figure 5.2: Graphical depiction of Kraut method. The valence band difference (ΔE_V) is determined by measuring the valence band edge to core level difference in two bulk samples. A series of thin heterostructures is then measured to determine the core level to core level split. All of these values can then be added together according to the equation above to yield the value of (ΔE_V).

is band bending at the interface. Once all samples are measured and analyzed, the data can be added together to get the desired value of ΔE_V. If the band gaps are known, then ΔE_C can also be determined and a band diagram can be constructed. The sample geometry and data analysis is visually reviewed in Figure 5.2.

5.3 Interface Stoichiometry Versus ZnO/Cu_2O Valence Band Alignment

We measured the valence band offset for the ZnO/Cu_2O system using the Kraut method described above. This system was particularly easy to measure because the perfect samples for a band offset measurement had already been fabricated when analyzing interface and surface stoichiometry, which is discussed in the previous chapter. Details of the XPS system and the thin heterostructures can be found in the previous chapter. A bulk Cu_2O wafer was used as the thick Cu_2O sample while a 100 nm ZnO film on Cu_2O was used as the thick ZnO sample. Films of 0.5, 1.0 and 1.5 nm were deposited on the Cu_2O, and the XPS data is shown in Figure 4.9. The Zn 3s, Cu 3s, and valence band peaks that were used to analyze the valence band offset for the Zn-rich ZnO/Cu_2O heterojunction are shown in Figure 5.3. The Zn 3s, Cu 3s, and valence band peaks that were used to analyze the valence band offset for the O-rich ZnO/Cu_2O heterojunction are shown in Figure 5.4

The ZnO/Cu_2O energy band alignment for the stoichiometric interface is shown in Figure 5.5. We found the stoichiometric interface had a valence-band offset of ΔE_V = -2.4 $\pm$0.1 eV, which is coincidentally identical to the offset predicted by the Anderson band alignment. We added in the previously measured band gap data for ZnO and Cu_2O to get the more useful value of conduction band offset, which was ΔE_C = -1.3 $\pm$0.1 eV. We would expect that this offset would greatly limit the potential voltage of a ZnO/Cu_2O device because a conduction band cliff provides a low barrier recombination path for carriers and decreases the possible work function difference between the two materials. It makes it all the more remarkable to consider that ZnO

is the most widely implemented heterojunction partner for Cu_2O when it is evident that the band alignment will greatly reduce device efficiency.

The ZnO/Cu_2O energy band alignment for heterojunctions with CuO at the interface is also shown in Figure 5.5. We found that CuO at the interface causes the valence-band offsets to shift to 2.0 ±0.1 eV. Combined with the band gap data the conduction band offset then becomes ΔE_C = -0.9 ±0.1 eV. Thus CuO at the interface changes the band alignment between Cu_2O and ZnO. The modification of heterojunction band alignment with the insertion of an interfacial layer has been observed previously in III-V and II-VI material systems [18]. It should be noted that the valence-band offset for the ZnO/Cu_2O heterojunction has been widely studied, with published values ranging from 1.7 to 2.8 eV [17, 25, 26, 33, 66]. However, little attempt has been made to correlate the observed variation in the offset with deviations in interface stoichiometry. The dependence of the band offset on interface composition, which in turn is dependent on the ZnO deposition conditions, is likely responsible for the large variation in reported offset values and emphasizes the need for improved control and understanding of the interface stoichiometry. Additionally, because CuO decreases the conduction band cliff, one would predict that its presence would be beneficial to photovoltaic device performance.

We also compared these ZnO interfaces to the band offset with copper, which is not a value we measured, but rather derived from literature because it is well known [6, 8, 9, 43]. We could not measure the band offset between Cu and Cu_2O via the Kraut method because that technique is only applicable to semiconductor/semiconductor heterojunctions. The alignment of Cu and Cu_2O is also shown in Figure 5.5.

5.4 Alignment to Zn-VI Materials

The alignment between ZnO and Cu_2O is unfavorable for photovoltaics, but we still believe that zinc is an ideal component of a heterojunction partner for Cu_2O. Therefore we also analyzed the valence band alignment for MBE deposited ZnSe and ZnS with Cu_2O. The XPS spectra for the O 1s and Se 3d core-levels for thin ZnSe/Cu_2O

interfaces are shown in Figure 5.6. The XPS spectra for the O 1s and S 2p core-levels for thin ZnS/Cu_2O interfaces are shown in Figure 5.7.

The band alignments for Zn-VI materials and Cu_2O are compared in Figure 5.8. ZnS has a valence band offset of ΔE_V = -0.88 ±0.10 eV and a conduction band offset of ΔE_C = 0.70 ±0.10 eV. It forms a type-I interface in that the band alignment straddles both the conduction band and valence band of Cu_2O. The conduction band alignment is also known as a conduction band spike, as the band offset is very positive. This alignment is generally favorable for surface passivisation, but can be a impediment to the flow of light generated carriers through a junction. If the barrier height is low enough, thermal emission through the junction can be efficient. However, barrier heights greater than about 0.4 eV do not allow for efficient enough thermal emission to make photovoltaic devices with reasonable currents. It is also possible to mitigate a conduction band spike by heavily doping the n-type layer. However, we were never able to attempt this method of allowing current flow because the dopants in the room temperature deposited ZnS were not activated and the material was intrinsic.

After analysis of the XPS data in Figure 5.6 we determined that ZnSe has a valence band offset of ΔE_V = -0.48 ±0.10 eV and a conduction band offset of ΔE_C = 0.12 ±0.10 eV. ZnSe is a possible heterojunction partner, as it has a conduction band spike within the ideal range of 0.0-0.4 eV. However, it should be noted that we found evidence of an interfacial reaction between ZnSe and Cu_2O, as reported in the previous chapter. We previously found that formation of an interfacial layer of CuO altered the band alignment between ZnO and Cu_2O, and thus our reported band alignment may not be entirely accurate.

Neither ZnO nor ZnS have a favorable alignment with Cu_2O, with ZnO forming a conduction band cliff and ZnS forming a conduction band spike. However, this does imply that there is a composition of Zn(O,S) that is aligned to the conduction band of Cu_2O. Zn(O,S) is a n-type material of variable composition that has been recently implemented in CIGS devices as a heterojunction partner with a tunable band alignment [2, 29]. Therefore the valence band alignment measurements indicate that Zn(O,S) and ZnSe are potential heterojunction materials.

5.5 Summary

Heterojunction band alignment is one of the most important parameters for photovoltaic device performance. A large conduction band cliff can decrease device voltage by limiting the work function difference between the heterojunction partners and providing carriers a low barrier path for recombination. However, a large conduction band spike can decrease the device current by preventing the flow of light generated carriers through the junction. Thus the ideal heterojunction material has a conduction band that sits very close to the conduction band of Cu_2O.

We measured the valence band offset between Cu_2O with ZnO, ZnS, and ZnSe due to the difficulty of predicting the band offset theoretically. We found that though ZnO is the most reproduced heterojunction partner in literature, it forms a very large conduction band cliff with Cu_2O which is extremely limiting to device efficiency. ZnS had an appropriate band offset for a surface passivation layer, but not a heterojunction partner, while ZnSe looked more favorable. Additionally, since the conduction bands of ZnS and ZnO straddle the conduction band of Cu_2O, Zn(O,S) is also a potential heterojunction partner.

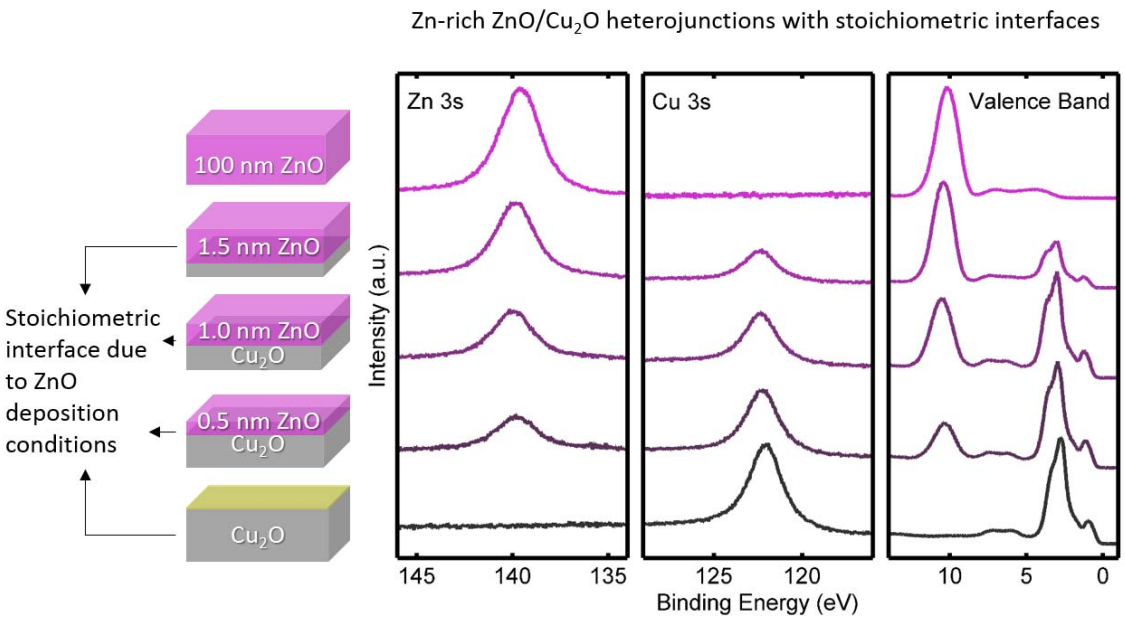

Figure 5.3: High-resolution X-ray photoelectron spectroscopy of the Zn-rich ZnO/Cu_2O interface. These peaks were used to analyze the valence band offset for the ZnO/Cu_2O junction with a stoichiometric interface.

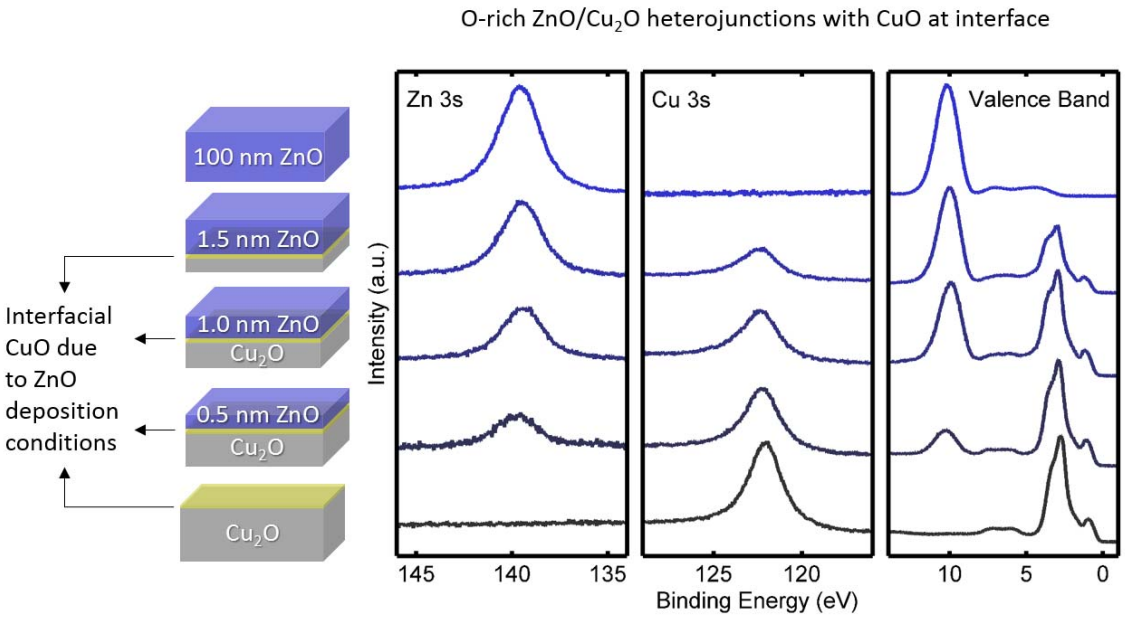

Figure 5.4: High-resolution X-ray photoelectron spectroscopy of the O-rich ZnO/Cu_2O interface. These peaks were used to analyze the valence band offset for the ZnO/Cu_2O junction with CuO present at the interface.

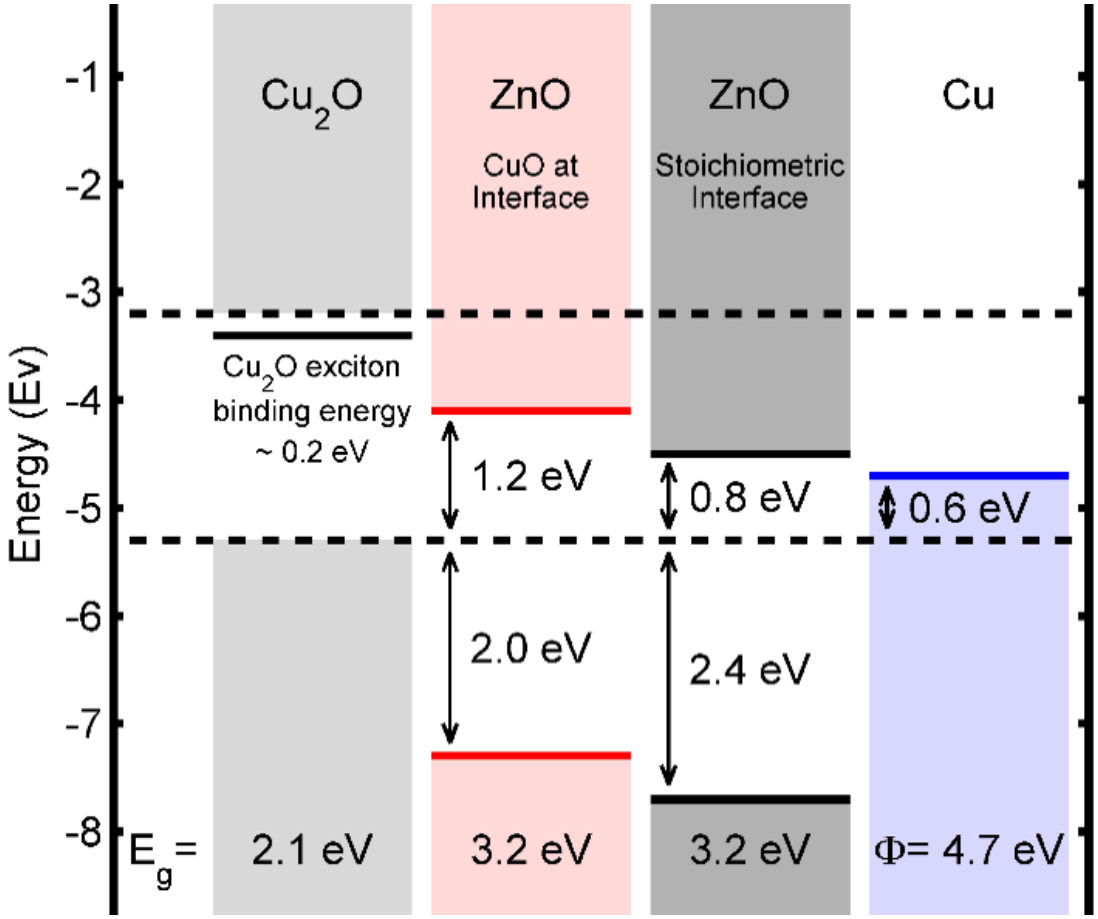

Figure 5.5: The X-ray photoelectron spectroscopy data in Figures 5.3 and 5.4 was analyzed according to the Kraut method outlined above to build the band offset plot. The values for ΔE_V are derived from the XPS data and the rest of the plot is built by inserting the previously measured band gap values.

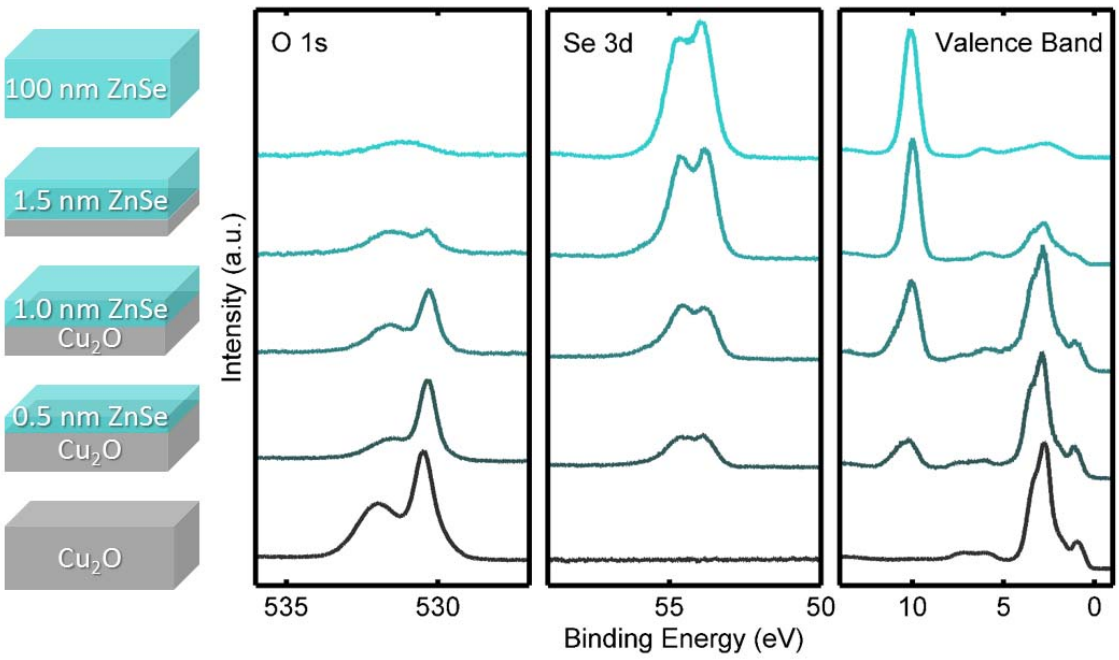

Figure 5.6: High-resolution X-ray photoelectron spectroscopy of the ZnSe/Cu_2O interface. The composition of the samples is indicated by the schematics at the left. These peaks were used to analyze the valence band offset for the ZnSe/Cu_2O junction.

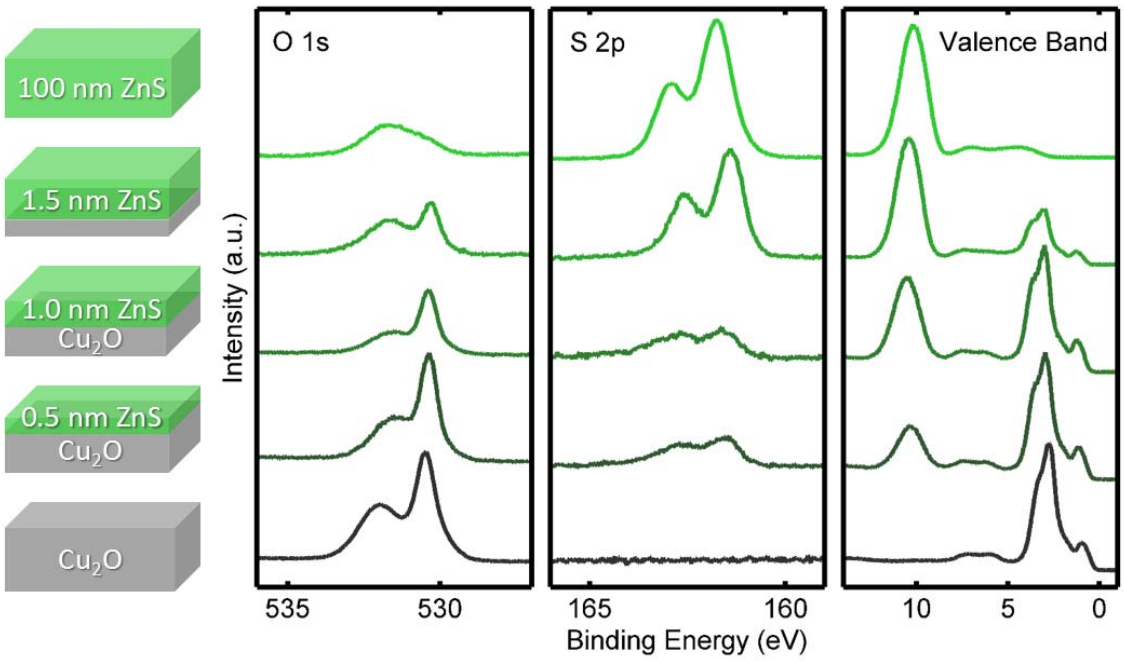

Figure 5.7: High-resolution X-ray photoelectron spectroscopy of the ZnS/Cu_2O interface. The composition of the samples is indicated by the schematics at the left. These peaks were used to analyze the valence band offset for the ZnS/Cu_2O junction.

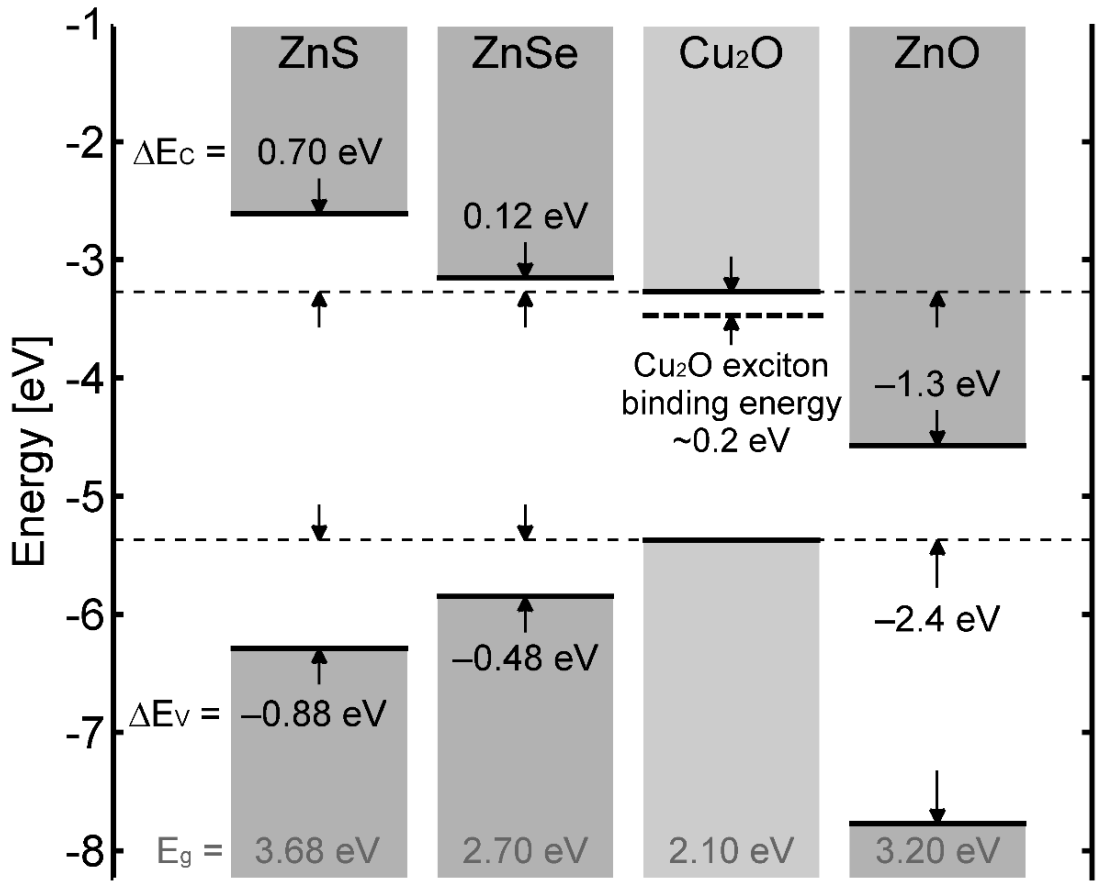

Figure 5.8: The X-ray photoelectron spectroscopy data in Figures 5.6 and 5.7 was analyzed according to the Kraut method outlined above to build the band offset plot. The values for ΔE_V are derived from the XPS data and the rest of the plot is built by inserting the previously measured band gap values.

Chapter 6

Analysis of Zn-VI Heterojunctions as Photovoltaic Devices

After characterization of the bulk materials and then further analysis of the heterojunction formation and properties, ZnO/Cu_2O and Zn(O,S)/Cu_2O photovoltaic devices were fabricated and tested. Unfortunately, we were unable to manufacture ZnSe or ZnS devices from the MBE deposited films because we were unable to dope the materials. The intrinsic materials were impossible to contact and we could not pass measurable current through any of the ZnS or ZnSe devices that were made. We still believe ZnSe is candidate material for a Cu_2O heterojunction due to its favorable band offset and we hope ZnSe/Cu_2O devices will receive further analysis in the future.

In this section we will discuss analysis of current voltage characteristics of ZnO/Cu_2O and Zn(O,S)/Cu_2O, as well as several of the techniques we have used to increase device efficiency including manipulating the stoichiometry of Cu_2O at the interface and better design of contacts, including selecting a new transparent conducting oxide.

6.1 Overview of Analysis of Current-Voltage Characteristics

All the ZnO/Cu_2O and Zn(O,S) Cu_2O devices were fabricated in a similar manner. In brief, the bulk Cu_2O wafers were used as the absorber layer. The heterojunction and contacts were formed by sputter deposition, and the devices were measured in a solar simulator with an AM 1.5 G filter. Analysis of the current density-voltage characteristic was performed both by analyzing trends in significant points on the curve, such as the short-circuit current and open-circuit voltage, as well as by fitting the data to the ideal diode equation. The details of all of these steps are elucidated below.

6.1.1 Overview of Device Manufacture

The devices were fabricated on bulk Cu_2O wafers, the manufacture of which is described in Chapter 2. For most devices we used the 800 μm thick wafers, although we did also experiment with both mechanically thinned wafers and with wafers manufactured from thin copper. The photovoltaic devices were all made using the air-exposed Cu_2O surfaces seen in Figure 4.4. This is due to the success we had making stoichiometric ZnO/Cu_2O interfaces from the air-exposed surfaces, which is detailed in Chapter 4. In fact, our results often became more reproducible when the wafers were air-exposed over the course of several days.

Once the Cu_2O was made and air-exposed, the heterojunction was formed by sputter deposition. We used the same AJA sputter deposition system described in Chapter 3 to deposit all of our thin film contacts. The first layer deposited was a

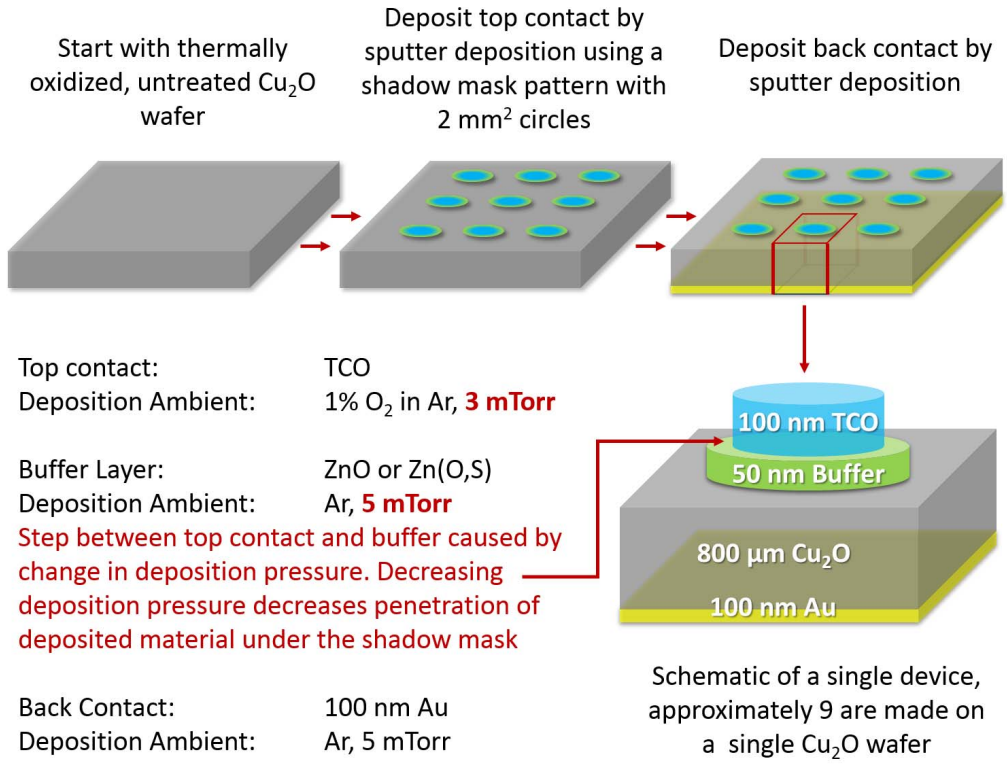

Figure 6.1: Schematic outlining the manufacture process for Zn-VI/Cu_2O devices from Cu_2O wafers. We start with air-exposed Cu_2O wafers. Then we use a shadow mask to isolate round devices with an area of 2 mm^2. We deposit a 50 nm buffer layer followed by a transparent conducting oxide (TCO) layer that is around 100 nm thick. We modulate the ambient pressure between the deposition of the buffer layer and the TCO in order to create a step edge to prevent formation of a shunt path. The back contact is 100 nm of gold, also deposited by sputter deposition.

50 nm buffer layer made of ZnO or Zn(O,S). The film was deposited in a pure argon ambient unless otherwise noted. The sputtering pressure was always kept at 5 mTorr and the layer was always deposited at room temperature.

Next a transparent conducting oxide (TCO) was deposited as a top contact. TCOs used include Sn:In_2O_3 (ITO), Al:ZnO (AZO), and Zn:In_2O_3 (IZO). In this case the deposition ambient was 1% O_2 in argon and the deposition pressure was 3 mTorr. Limited oxygen was added to the deposition ambient to optimize the transparency of the deposited thin films while maintaining high conductivity. Additionally the deposition pressure was lowered to prevent the TCO forming a direct contact with the Cu_2O surface. The devices were electrically isolated using a shadow mask. Because sputtering is a slightly conformal process we would expect some deposition of Zn(O,S) under the shadow mask. By lowering the deposition pressure, we change the mean free path of the sputtered material and decrease the conformal nature of the deposition. Thus we create a step-edge that prevents the TCO from directly contacting the Cu_2O surface and forming a shunt path for current. The TCO layer was directly electrically contacted with probe tips for analysis of the current-voltage characteristic.

The final step was the deposition of the back contact by sputter deposition. Gold was typically used, although some devices were made with platinum. No difference was observed in device performance between the two materials. The gold layer was 100 nm thick and deposited at room temperature in an Ar ambient. The overall pressure was restricted to 5 mTorr. Once the gold was deposited, the device was ready to be tested.

6.1.2 Measurement of J-V Characteristic

In order to analyze device performance, the current density-voltage characteristic for the devices was collected. Measurements were performed both in the dark and under AM 1.5 1-sum simulated illumination. The spectrum was normalized using a silicon reference cell purchased from and calibrated by PV Measurements, Inc. The reference cell is silicon, which has a band gap of 1.1 eV, while Cu_2O only starts

absorbing at 1.9 eV. Thus, additional calibration steps were needed to account for the spectral mismatch in the illumination source. A 670 nm short pass filter was used with the silicon reference cell to restrict the light illuminating the silicon reference cell to below 670 nm. The external quantum efficiency of the silicon reference cell was integrated to 670 nm to give the expected short circuit current at that illumination. This calibration was used with all devices tested.

The TCO served as the top contact and the cell was illuminated through the layer. The top contact was contacted using a standard probe station. The Cu_2O device was adhered to a gold coated substrate holder using conductive copper tape so that the substrate holder was in electronic contact with the back of the sample. The measurements were performed using a Kiethley 236 source measure unit. We contacted the devices in a 2-contact configuration and swept voltage while measuring current unless otherwise indicated.

6.1.3 Fitting J-V Characteristic to Ideal Diode Equation

Photovoltaic cells in the dark are described by the ideal diode equation, which when incorporating both parallel and series resistance can be written as follows:

$$I = I_0 \exp\left(\frac{q\left(V - IR_S\right)}{nkT} - 1\right) + \frac{V - IR_S}{R_{Sh}}$$

Photovoltaic devices are usually better approximated by the dual diode equation which takes into account a change in diode ideality factor (n) with voltage [24, 41]. However, we know that Cu_2O is in high level injection under illumination because its carrier concentration increases under illumination [67]. This indicates Cu_2O is in high level injection and the ideality factor should be 2 throughout the measured voltage range [24]. For all fitting we use a diode ideality factor of 2. We also incorporated parasitic resistances into the model to fit non-idealities with series resistance (R_S) and shunt resistance (R_{Sh}) where series resistance is the resistance in series with the diode and shunt resistance is the resistance in parallel with the diode. I_0 is the final fit parameter in the equation and is also known as the dark current, saturation current,

and reverse saturation current.

Under illumination, the minority carrier populations increases to the point that the current reverses and the equation describing the J-V character becomes:

$$I = I_0 \exp\left(\frac{q\left(V - IR_S\right)}{nkT}\right) + \frac{V - IR}{R_{Sh}} - I_L$$

Both the dark and illuminated I-V curves are plotted in Figure 6.2. The prominent features of the curve, including open-circuit voltage, short-circuit current, and fill factor, are labeled.

Light generated current (J_L) is caused by light-generated minority carriers that travel through the heterojunction. If series resistance is low enough, J_L is also equal to the short-circuit current (J_{SC}). The short circuit-current is the current under illumination at 0 volts and is highlighted in Figure 6.2. It is effected by both material parameters and device design. It can be increased by increasing the minority carrier diffusion length such that more light generated carriers are able to diffuse to the junction. Additionally, the geometry of the transparent layers such as transparent conducting oxides and anti-reflection coatings can be designed to ensure that light is reaching the absorbing layer. Because short-circuit current is so sensitive to both material quality and device geometry, it can be a difficult parameter to parse. For instance, if the TCO deposition is inconsistent and the thickness of the layer varies somewhat, the J_{SC} can also vary in a seemingly random manner.

The voltage at 0 current is known as the open-circuit voltage, or V_{OC}. The V_{OC} is a more sensitive component to actual material quality due to its dependence on the reverse saturation current (I_0), which is described below:

$$V_{OC} = \frac{nkT}{q} \ln\left(\frac{I_L}{I_0} + 1\right)$$

Thus the V_{OC} is not only sensitive to light collected current, but also to the bulk and interface properties of the material. Additionally, because V_{OC} is only sensitive to the logarithmic light collected current, it is less sensitive to small changes in light

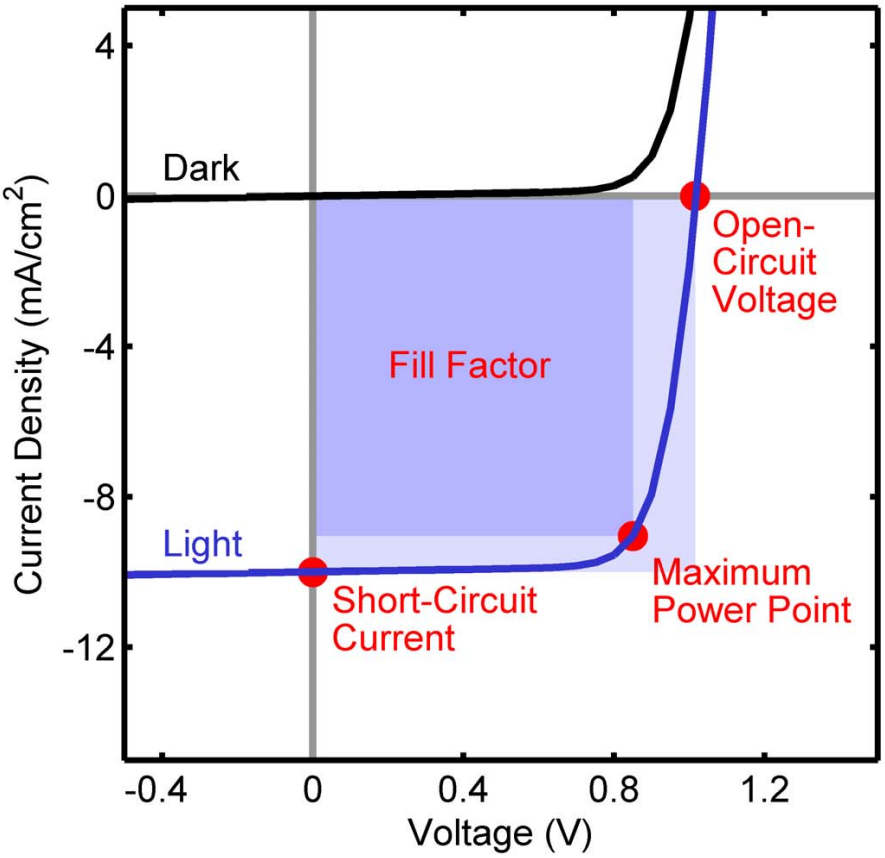

Figure 6.2: A plot of typical current density-voltage ($J-V$) curves for a photovoltaic device in both the light and the dark. The lines are built using typical parameters for a Cu_2O device which are inserted into the ideal diode equation. Several important points on the light curve are labeled including open-circuit voltage, short-circuit current, the maximum power point, and the fill factor. The fill factor is defined as the ratio of the maximum power point to the short circuit current multiplied by the open-circuit voltage. This is visualized on the figure above as the darker blue box divided by the lighter blue box. Fill factor is a percent factor that defines the squareness of the $J-V$ curve.

collected current caused by device design. Thus it is a fair indicator of materials quality. There are two main sources of reverse saturation current: recombination of light generated current and injection of majority carriers through the junction. Because open-circuit voltage is sensitive to recombination, it is considered the best measure of overall device quality.

The last aspect of photovoltaic device curve is called the fill factor, which is a ratio of the current multiplied by the voltage at the maximum power point compared to the current and the voltage at the open and short circuit. It describes that overall squareness of the J-V curve and is greatly affected by parasitic losses due to series and shunt resistances. We will further discuss fill factor later in the chapter.

6.2 Current-Voltage Analysis of ZnO/Cu_2O Devices with Different Interface Stoichiometries

The first set of photovoltaic devices we explored were ZnO/Cu_2O devices made with either stoichiometric interfaces, copper at the interface, or CuO at the interface. These three interfaces were manufactured according to the sputtering procedures outlined in Chapter 4 and displayed in Figure 4.9. In brief, we previously found that by changing the deposition ambient from a partial pressure of 0.00 mTorr O_2 to 0.25 mTorr O_2, the stoichiometry of the interface shifted from containing stoichiometric Cu_2O to containing traces of CuO, respectively. We also found that if we sputtered pure Zn onto the interface that the CuO and Cu_2O at the interface reduced to copper. Presumably the Zn was then oxidized to ZnO. We made devices with these three interfaces in identical TCO/Buffer layer/Cu_2O/Au geometries by taking advantage of these interfacial reactions.

For the devices with stoichiometric interfaces, the 50 nm ZnO buffer layer was deposited in a pure argon atmosphere. The devices with CuO at the interface had a buffer layer deposited in a 0.25 mTorr partial pressure of O_2. The devices with copper at the interface were made by depositing 1 nm of pure Zn followed by 49 nm of ZnO

in an argon ambient. All devices had identical 100 nm ITO top contacts and 100 nm Au back contacts. The details of device fabrication and geometry are outlined above.

The J-V curves for the devices were obtained at AM 1.5 1-sun illumination following the procedure described in section 6.1 and can be seen in Figure 6.3. Open-circuit voltage of photovoltaic devices (Figure 6.3) was used to evaluate the relationship between the interface stoichiometry and the electronic quality of ZnO/Cu_2O heterojunctions. We focused our analysis on device open-circuit voltage because it is more sensitive to interface and bulk defects than other J-V characteristics and is thus considered an appropriate measure of interface quality. The reported open-circuit photovoltages were averaged over a minimum of nine tested devices. The device with the stoichiometric interface demonstrated the highest open-circuit voltages of 530 $\pm$ 4 mV. The devices fabricated with CuO and Cu inclusions at the interface had substantially lower average open-circuit voltages of 109 $\pm$ 11 mV and 347 $\pm$ 30 mV, respectively. The short-circuit current densities and efficiencies of all of the devices were limited by the resistivity (ρ>1500 Ω-cm) and thickness (800 μm) of the Cu_2O substrate, as indicated by the small fill factors.

In order to understand the voltage limits of the stoichiometric devices we modeled the band bending at the ZnO/Cu_2O interface by solving the 1-D Poisson equations, which is shown in Figure 6.4. For this model we chose a Cu_2O doping level of 10^{14} cm^{-3} to reflect the majority carrier concentration of our thermally oxidized Cu_2O wafers under illumination [67]. To calculate the carrier concentration in the ZnO, we made a conservative estimate of mobility in the sputtered thin film of 1 $cm^2V^{-1}s^{-1}$. We then used the measured resistivity of 1 Ω*cm to calculate a carrier concentration of 10^{17} cm^{-3}. Solving the Poisson equation, we calculated a built-in voltage of 480 $\pm$ 100 meV. The error in the estimation comes from the error in the band offset calculation, which has a much larger effect than error in the doping estimates. The built-in voltage is the voltage drop across the space charge region at equilibrium and is also equal to the work function difference between the bulk materials. It also serves as the maximum achievable open-circuit voltage in an ideal device. That the open-circuit voltage and the built-in voltage are so close shows that the stoichiometric

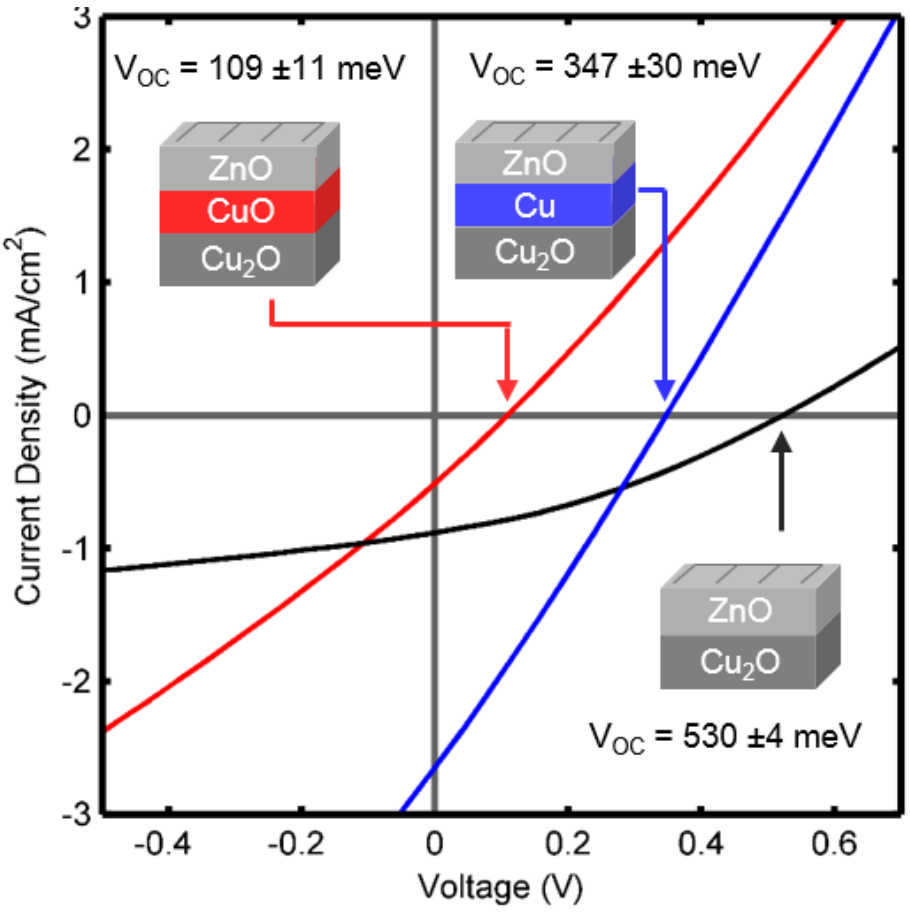

Photovoltaic Device Structure	Open-Circuit Voltage	Short-Circuit Current	Fill Factor
ZnO/Cu_2O	530 ±4 mV	0.69 ±0.46 mA/cm^2	30.4 ±3.85%
$ZnO/CuO/Cu_2O$	109 ±11 mV	0.46 ±0.21 mA/cm^2	25.5 ±0.74%
$ZnO/Cu/Cu_2O$	347 ±30 mV	1.41 ±0.54 mA/cm^2	26.0 ±0.56%

Figure 6.3: The J-V curves for ZnO/Cu_2O photovoltaic devices made with different interface compositions is shown above. The stoichiometric interfaces show the largest open-circuit voltages. The short-circuit currents and fill factors are low due to series resistance.

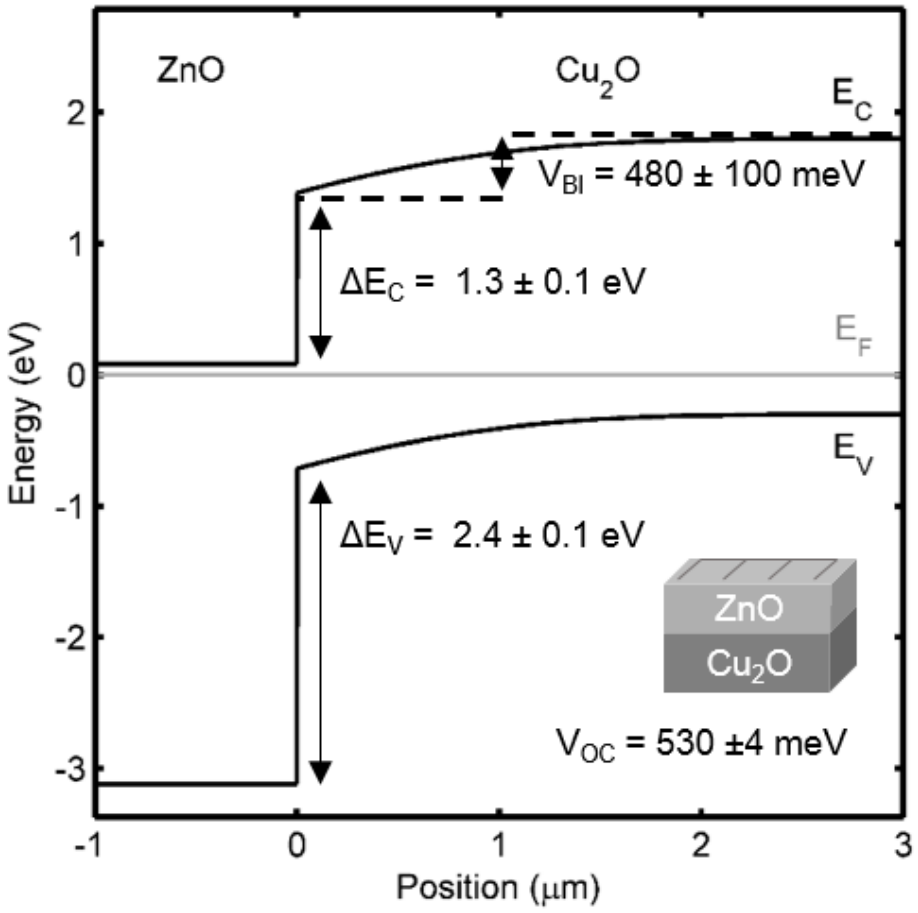

Figure 6.4: The 1-D Poisson equations were solved for a ZnO/Cu_2O junction in order to determine the voltage limits of the device. That the ideal built-in voltage and the measured open-circuit voltage are so similar indicates the formation of a near perfect interface.

interface is approaching its voltage entitlement, meaning the interface recombination must be low. Thus the stoichiometric device performance is limited solely by the heterojunction offset, and the large series resistance contribution of the undoped Cu_2O substrate. If stoichiometry is maintained at the interface and an emitter with a more favorable offset is found, we believe large voltages and high efficiencies are achievable in a Cu_2O device.

The open-circuit voltage observed for the Cu interface is in agreement with the expectation that a Cu/Cu_2O Schottky barrier is formed at the interface. The reactively formed Cu/Cu_2O interface has been explored previously, and the device photovoltages align well with the work of Olsen et. al. and Assimos et al. It is well understood that the device voltage is limited by the small work function difference between Cu_2O and Cu metal, and our photovoltages are identical to those previously achieved in Cu/Cu_2O Schottky devices [6, 43].

Analysis of the $ZnO/CuO/Cu_2O$ devices is slightly less obvious, because according to the valence-band offset measurements, these devices should have a larger built-in voltage and open-circuit voltage than the devices with stoichiometric interfaces. However, the opposite trend was observed from the device measurements. There are several possible reasons for this, including increased recombination at the interface and Fermi level pinning due either to the low band gap of CuO (~1.2 eV) or an increased density of interface states. However, we believe the lower observed open-circuit voltage for the device with CuO at the interface is most likely due to the degenerate nature of CuO. It is difficult to make a rectifying contact to CuO, and its presence would make contact at the junction nearly ohmic [64]. These results show the importance of controlling the emitter deposition conditions in order to control the heterojunction interface composition. Clearly, a stoichiometric Cu_2O interface is desirable for obtaining improved photovoltaic device performance. All devices discussed later in this section have been manufactured with stoichiometric interfaces according to the procedures outlined in Chapter 4.

6.3 Efforts to increase the Fill Factor

The fill factor is simply defined as the ratio of the maximum power point to the open-circuit voltage multiplied by the short-circuit current and is a value that represents the squareness of the IV curve. This ratio is illustrated graphically in Figure 6.2. The more square the IV curve, the larger the power output the device can achieve. There are several obstacles in the way of achieving a high fill factor. For Cu_2O the main impediments are bias dependent collection and high series resistance. Shunt resistance can also decrease the fill factor. Our initial ZnO/Cu_2O devices shown in Figure 6.3 had very low fill factors, which contributed to their low overall efficiencies. In this section we will review our attempts to trace the origin of the low fill factor and our attempts to increase the device fill factor.

The effect of series resistance and shunt resistance on the efficiency of a Cu_2O device is demonstrated by the simulated J-V curves in Figure 6.5. The isoefficiency lines in the figure define the current and voltage requirements needed for device efficiencies ranging from 1% to 25% for 1-sun AM 1.5 G illumination with a standardized power density of 1000 W/m^2. As the series resistance increases, current flow through the device is impeded and the maximum power point drops to lower efficiencies. Once the series resistance is large enough, the short-circuit current also starts to drop. These are the conditions in which the short-circuit current and the illuminated current are not equal. Similarly, as the shunt resistance decreases, more current is diverted around the diode, and fill factor and open circuit voltage start to decrease.

Bias dependent collection is a a non-ideality that is not captured by the ideal diode equation. We shall further explore it later in this section.

6.3.1 Series Resistance versus Thickness of the Absorber Layer

Cu_2O has a unique advantage over most solar materials in that there is a rapid and simple process by which wafers can be manufactured. However, doping of Cu_2O has never been possible and the intrinsic Cu_2O is quite resistive [10]. Thus we have analyzed the impact of thickness of the absorber layer on Cu_2O device efficiency for

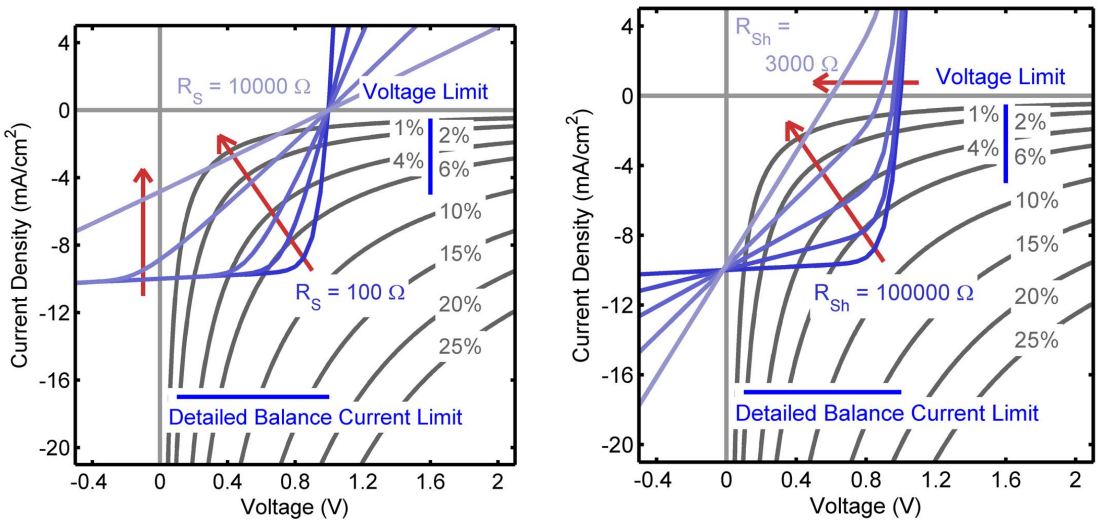

Figure 6.5: Series resistance (R_S)is resistance in series with the diode in a photovoltaic cell while shunt resistance (R_{Sh}) is the resistance parallel to the diode. The effect of series resistance on the J-V character of a photovoltaic device is demonstrated in the image to the left. As the series resistance increases, current flow through the device is impeded and the maximum power point drops to lower efficiencies. Once the series resistance is large enough, the short-circuit current also starts to drop. These are the conditions in which the short-circuit current and the illuminated current are not equal. The effect of shunt resistance on the J-V character of a photovoltaic device is demonstrated in the image to the right. As the shunt resistance decreases, more current is diverted around the diode, and fill factor and open circuit voltage start to decrease. The isoefficiency lines define the current and voltage requirements needed for device efficiencies from 1% to 25% for AM 1.5 G illumination with a standardized power density of 1000 W/m^2.

both the small device geometry that we work with and what we would expect from a 125 cm^2, industrial sized wafer.

The first step we took was measuring the series resistance through the Cu_2O wafer directly. This was done by applying 100 nm gold as a top contact by sputter deposition through a shadow mask using the same parameters we use for gold back contacts. We then also deposited a full gold back contact. Thus we can measure the actual series resistance contribution of bulk Cu_2O to the devices. The data from these measurements is shown in Figure 6.6 and we calculated a resistance of 802 Ω based on the 9 devices we tested.

Next we sought to verify that 802 Ω was a reasonable number based on the hole concentration of between 10^{13} and 10^{14} and the mobility of 100 $cm^2V^{-1}s^{-1}$ based on earlier Hall coefficient measurements. In this case the size of the top contact is much smaller than the bottom contact, and thus current will travel through the device in a conical pattern [51]. The equation resistance through a truncated cone is

$$R = \frac{4\rho h}{\pi D_1 D_2}$$

where R is the resistance, ρ is the resistivity, h is the height of the sample, D_1 is the diameter of the contact pad, and D_2 is the diameter of the back contact. We substituted the mobility and carrier concentration according to the equation for the resistivity of a p-type material,

$$\rho = q\mu p$$

in order to determine the implied carrier concentration. We used a height of 800 μm and a mobility (μ) of 100 $cm^2V^{-1}s^{-1}$, and D_1 was set at 2 mm and D_2 set at 1 cm. This gave us an implied carrier concentration of $4*10^{13}$ cm^{-3} which is analogous to our previous Hall measurements. Therefore 802 Ω is believed to be an accurate measurement of the series resistance contribution of the Cu_2O wafer.

We used this number to make some estimates of fill factor for a device that is solely limited by the series resistance contribution of the bulk wafer. The results of simulating the efficiencies for 2 mm^2 devices with different thickness is shown in

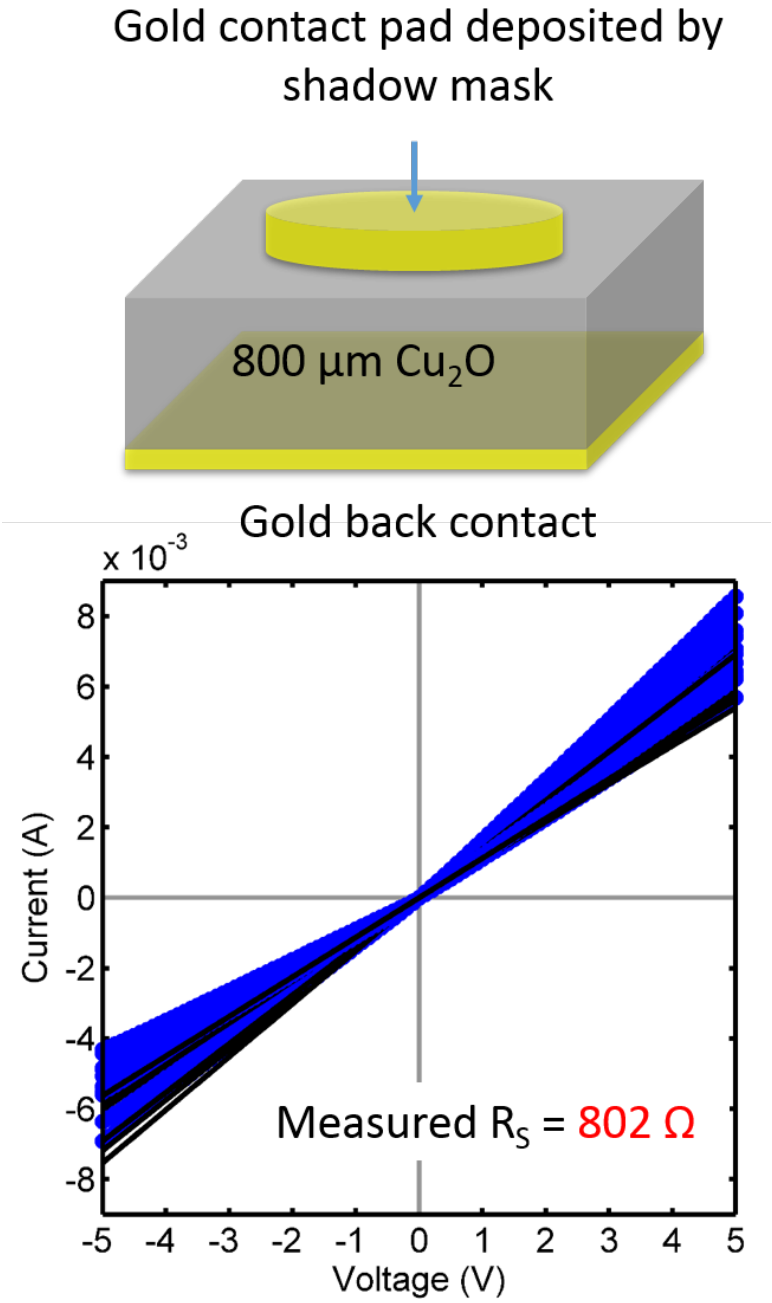

Figure 6.6: The series resistance (R_S) contribution of the bulk Cu_2O was measured by applying ohmic gold contacts to both sides of a Cu_2O wafer in the same geometry used for devices. The measured series resistance contribution of 800 µm thick wafer is $R_S = 802\ \Omega$.

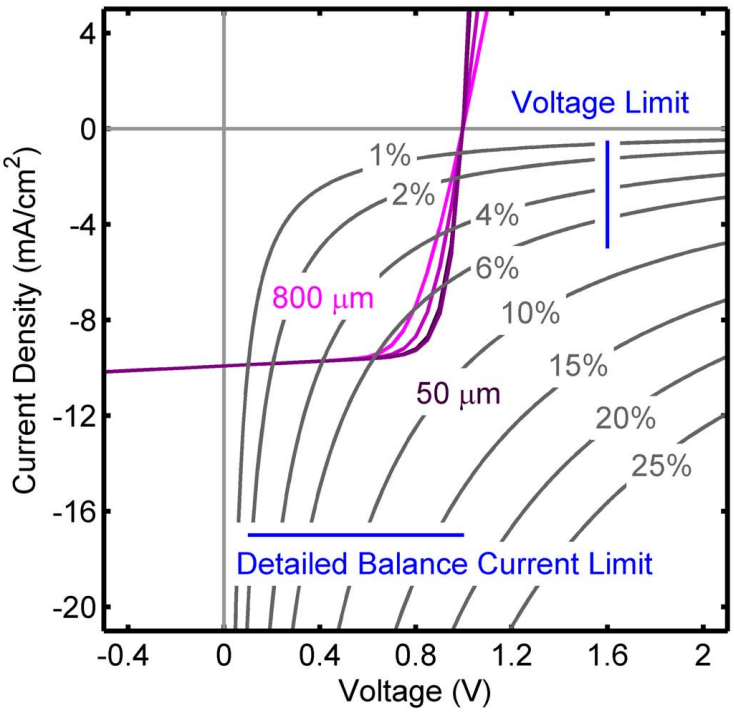

Cu_2O Thickness	R_S	Fill Factor	Power Conversion Efficiency
800 μm	802 Ω	63.9%	6.3%
400 μm	401 Ω	70.1%	6.9%
100 μm	100 Ω	74.5%	7.4%
50 μm	50 Ω	75.6%	7.5%

Figure 6.7: Simulated fill factors were modeled with the ideal diode equation. The bulk series resistance was the only contribution to series resistance. The values for all the curves are listed in the table. If thickness really is the only contribution to series resistance, then it does not seem to be very limiting. Other numbers used for analysis were based on the most efficient Cu_2O devices thus far and were $I_0 = 10^{12}$ A, $I_L = .0002$ A, $R_{Sh} = 100{,}000$ Ω, and the diode ideality factor $n = 2$. It was impossible for the fill factor to reach 80% with a diode ideality factor of 2, but we could not physically justify using a smaller ideality factor.

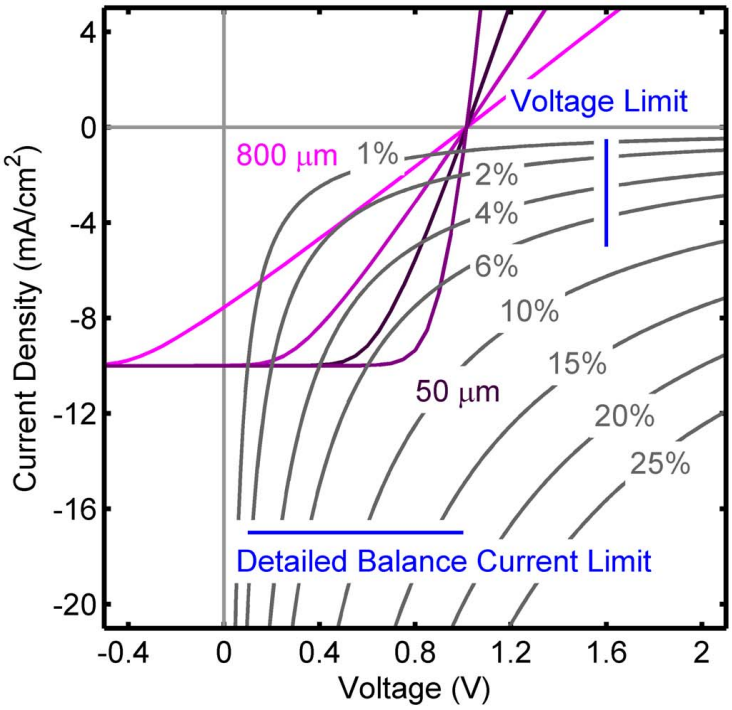

Cu_2O Thickness	R_S	Fill Factor	Power Conversion Efficiency
800 μm	0.998 Ω	26.0%	2.0%
400 μm	0.499 Ω	36.1%	3.6%
200 μm	0.250 Ω	55.4%	5.5%
50 μm	0.062 Ω	74.8%	7.5%

Figure 6.8: Simulated fill factors were modeled with the ideal diode equation. The bulk series resistance was the only contribution to series resistance. The simulated power conversion efficiency and fill factors for all the curves are listed in the table. In this case, thickness is more limiting due to the larger current in the larger devices. Series resistance multiplies with current in the ideal diode equation, and thus has a larger impact on higher current devices. Still it is possible to achieve a fill factor greater than 70% with a Cu_2O thickness that is accessible by bulk growth methods. Other numbers used for analysis were based on the most efficient Cu_2O devices thus far and were $I_0 = 4*10^{-9}$ A, $I_L = 1.25$ A, $R_{Sh} = 100{,}000$ Ω, and the diode ideality factor $n = 2$. It was impossible for the fill factor to reach 80% with a diode ideality factor of 2, but we could not physically justify using a smaller ideality factor.

Figure 6.7. Looking at the above relation between series resistance and thickness, we see that the series resistance will directly scale with the thickness of the wafer. Therefore we simply used an equal ratio to calculate the series resistance values used at different thicknesses. Other numbers used for analysis were based on the most efficient Cu_2O devices thus far and were $I_0 = 10^{12}$ A, $I_L = .0002$ A, $R_{Sh} = 100{,}000$ Ω, and the diode ideality factor n = 2. Based on this analysis, we would only need to get to a thickness of 400 μm to achieve a fill factor greater then 70%. This is quite achievable, thus thickness and bulk series resistance do not appear to be large impediments to high fill factors.

The above analysis is for a photovoltaic device with the structure of the devices described in the previous section. Devices were circular with an area of 2 mm^2 on an approximately 1 cm^2 Cu_2O wafer. Analysis of devices this small isn't necessarily useful, so we ran a similar analysis using a much larger device size. We chose a size of 125 cm^2 for the large wafer as that accurately reflects the size of silicon devices installed in series in silicon modules [53]. We assumed a mobility of 100 $cm^2V^{-1}s^{-1}$ and used the carrier concentration calculated earlier at $4*10^{13}$ cm^{-3}. We used these numbers to calculate that Cu_2O has a resistivity of 1560 Ω*cm. The device was assumed to full occupy the entire area of the wafer, so the bulk contribution to series resistance is given by:

$$R = \frac{\rho h}{A}$$

where h is the thickness of the wafer and A is the device area. The calculated resistivities and simulated J-V curves are shown in Figure 6.8. Other numbers used for analysis were scaled to match the new device size and were $I_0 = 4*10^{-9}$ A, $I_L = 1.25$ A, $R_{Sh} = 100{,}000$ Ω, and the diode ideality factor n = 2. In this case the resistivity still correlates directly to the wafer thickness, but changes in thickness have a much larger effect, as in the same thickness range the fill factor goes from 25% to 75%. This is because series resistance is multiplied by current in the ideal diode equation, thus as the device area gets large, the current gets larger, causing the effect of series resistance to be magnified. However, we also see that fill factors above 70% are still

Transparent Conducting Oxide	Sheet Resistance ($\Omega/\square$)
98% ZnO, 2% Al_2O_3	10,000
90% In_2O_3, 10% SnO_2	300
90% In_2O_3 10% ZnO_2	30

Table 6.1: Sheet Resistance of the transparent conduction oxides we studied. IZO has the smallest sheet resistance, while AZO is quite resistive at room temperature.

achievable with wafer thickness we can easily access using a bulk growth process. Thus we do not believe bulk resistivity is an impediment to efficient, scalable Cu_2O photovoltaics.

6.3.2 Analysis of Series Resistance Contribution of Transparent Conducting Oxides

Another common source of series resistance in photovoltaic cells is sheet resistance in the top contact. For our process, deposition of both the emitter layers and the transparent conducting oxide layers (TCOs) was restricted to room temperature in order to maintain control of the interfacial reactions. These conditions are not ideal for conductivity in traditional TCO materials such as Al:ZnO, (AZO) and Sn:In_2O_3 (ITO). We also tested a less traditional TCO material, Zn:In_2O_3 (IZO), which was developed for its superior conductivity and transparency when deposited at room temperature.

The sheet resistance of the three TCO layers was assessed by 4-point-probe measurements, which directly measure the sheet resistance of a thin film. The results are given in Table 6.1. Based on this, we tried 100 nm of both ITO and 100 nm IZO as TCO layers. A comparison of Au/Cu_2O/ZnO devices with 100 nm of ITO and 100 nm of IZO is made in Figure 6.9. The diodes made with IZO had much lower series resistances, so we choose to use IZO as our transparent conducting layer for future devices.

We performed one final experiment in order to determine that the TCO was no

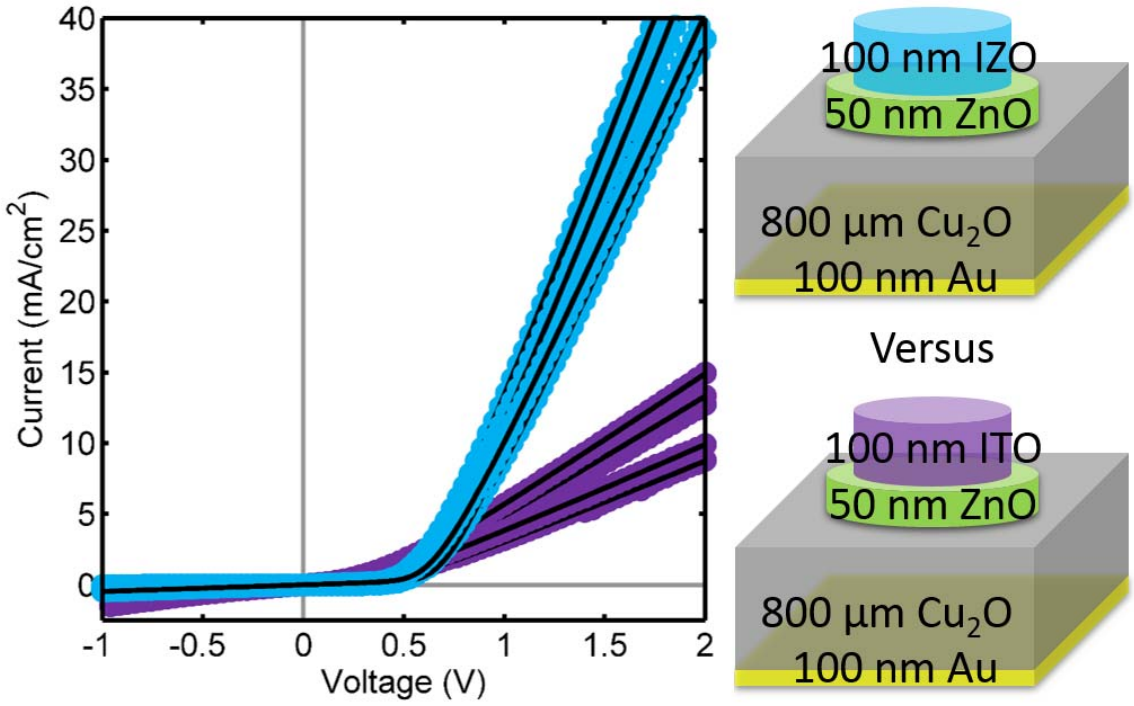

Fitting Parameter	IZO Top Contact,Dark	ITO Top Contact,Dark
I_0	$1.1*10^{-9} \pm 0.6*10^{-9}$A	$2.1*10^{-8} \pm 1.6*10^{-8}$A
R_S	1405 ± 125 Ω	6530 ± 1400 Ω
R_{Sh}	171,000 ± 51,000 Ω	166,000 ± 74,000 Ω
I_L	0 A	0 A
n	2	2

Figure 6.9: A comparison of diodes made with 100 nm of ITO and 100 nm of IZO according to the schematics above. The dark J-V curve was fit to the ideal diode equation and the fitting parameters are given in the table. The devices made with IZO show a clear decrease in series resistance. This does indeed translate to an increase in fill factor shown in Figure 6.11.

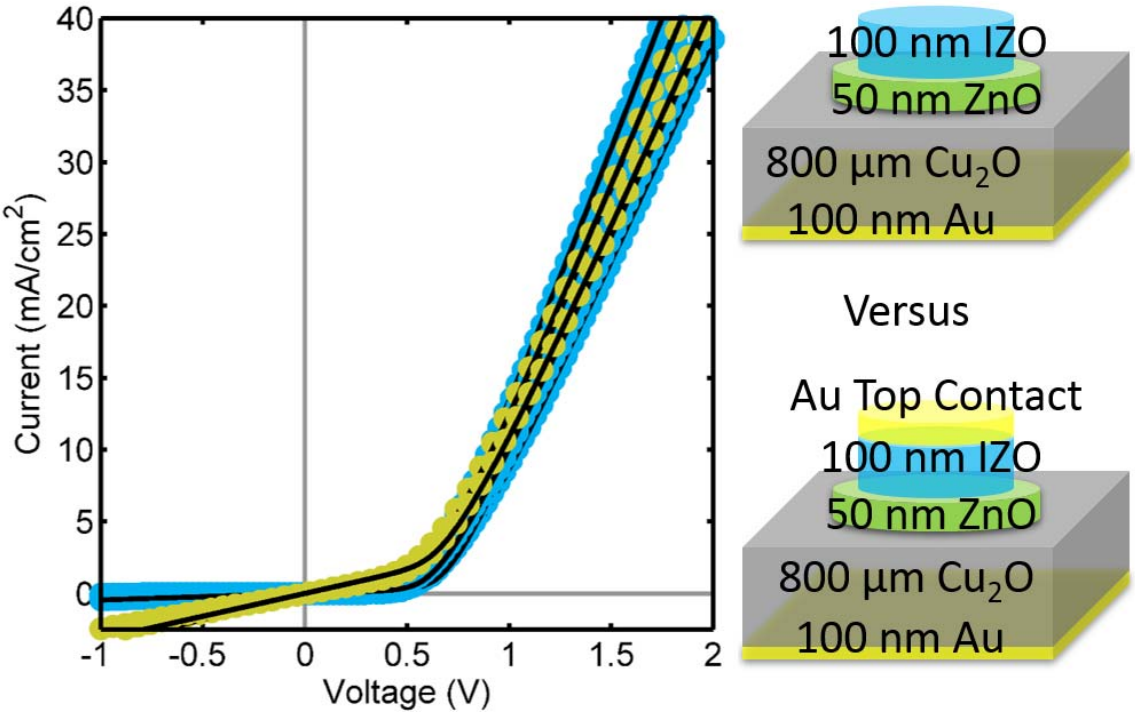

Fitting Parameter	IZO Top Contact, Dark	Au/IZO Top Contact, Dark
I_0	$1.1*10^{-9} \pm 0.6*10^{-9}$A	$6.0*10^{-10}$ A
R_S	1405 ± 125 Ω	1470 Ω
R_{Sh}	171,000 ± 51,000 Ω	13,000 Ω
I_L	0 A	0 A
n	2	2

Figure 6.10: Comparison of the dark diode characteristic for Au/Cu_2/ZnO devices with IZO top contacts, and devices with IZO/Au top contacts. The purpose of the comparison is to confirm that the TCO sheet resistance is not a limiting element in the device series resistance. This is confirmed, as the fitting shows that the devices with Au coating the IZO had the same series resistance as those without gold.

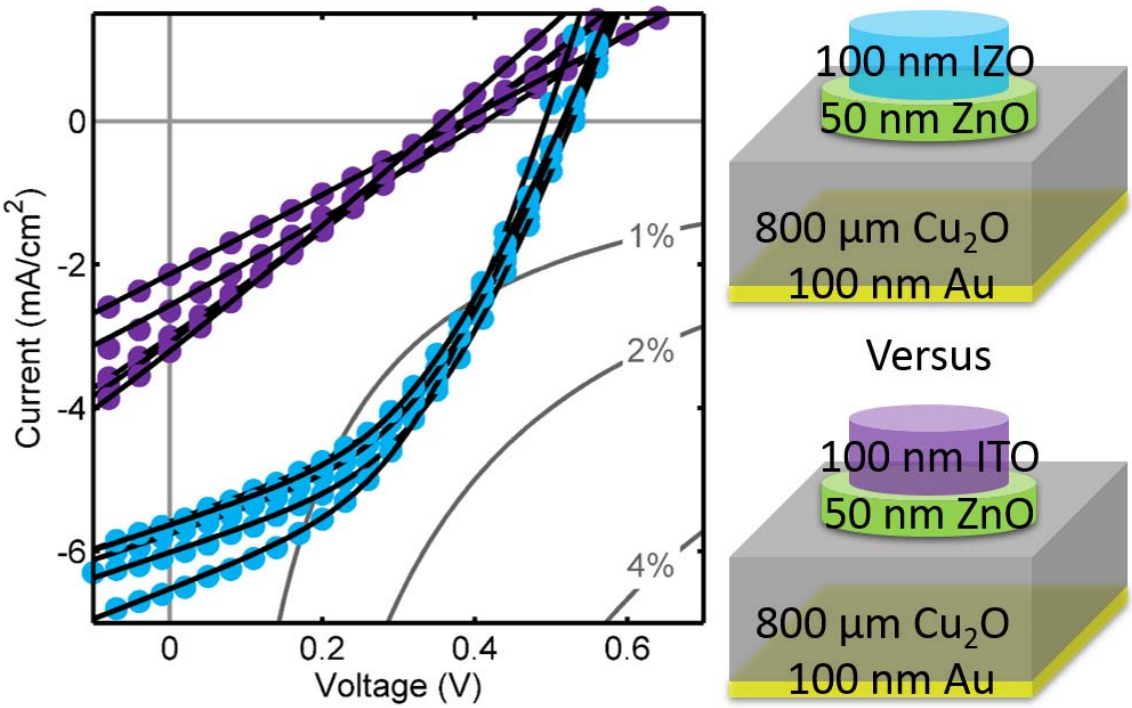

Fitting Parameter	IZO Top Contact, Light	ITO Top Contact, Light
I_0	$4.6*10^{-9} \pm 1.8*10^{-9}$A	$6.6*10^{-8} \pm 2.9*10^{-8}$A
R_S	1380 ± 160 Ω	6370 ± 1400 Ω
R_{Sh}	12,000 ± 800 Ω	166,000 ± 74,000 Ω
J_L	6.7 ± 1.0 mA/cm^2	6.6 ± 0.4 mA/cm^2
n	2	2
Fill Factor	41.7% ± 0.5%	25.5% ± 0.01%
V_{OC}	516 ± 15 mV	387 ± 20 mV
J_{SC}	5.90 ± 0.39 mA/cm^2	2.80 ± 0.45 mA/cm^2
Efficiency	1.27% ± 0.07%	0.28% ± 0.04%

Figure 6.11: Comparison of Au/Cu_2O/ZnO/IZO and Au/Cu_2O/ZnO/ITO devices under AM 1.5 G illumination. The decreased series resistance leads to an increase in fill factor, short-circuit current, and efficiency. There is a difference in the reverse saturation current that accounts for the difference in open-circuit voltage; the origin of this difference is unknown. The difference in the illuminated current and the short circuit current is due to series resistance.

longer limiting the series resistance of the devices. For this experiment we compared the diode resistance of five Au/Cu_2O/ZnO/IZO devices to two Au/Cu_2O/ZnO/IZO/Au devices. The gold thin film used for the top contact was deposited at 3 mTorr, instead of the standard 5 mTorr. This was the only difference from the standard manufacturing procedures outlined in the first section of this chapter. The J-V data as well as the ideal diode fitting for this data is shown in Figure 6.10. The gold coated devices and the devices with only IZO both had series resistances of around 1400 Ω, which tells us both that the probe contact to the TCO layer is not a significant source of series resistance and that the TCO sheet resistance is no longer limiting series resistance. It is also interesting to note that the device series resistance is greater than the bulk wafer resistance, which was measured as 800 Ω. Thus there is an unknown source of series resistance in the devices due to junction formation. We will expand on this thought more later.

Finally, we compared the devices with IZO as a top contact to those with ITO as a top contact under illumination. Due to the difference in series resistance in the dark, we would expect a difference in fill factor in the illuminated J-V curves. That is indeed what we see. The fill factor increases to over 40% when using IZO as a top contact. Additionally, the short-circuit current and power conversion efficiency increase with the decreased series resistance. The two sets of devices also show a difference in open-circuit voltage which is related to the difference in reverse saturation current. The source of this change in reverse saturation current is unknown, but is likely due to a difference in the bulk Cu_2O. In any case it has no bearing on the measure of series resistance, and thus was ignored.

6.3.3 Analysis of "Photo-shunting" Behavior

There was one final source of the low fill-factor; we found when we fit the J-V curves for the Au/Cu_2O/ZnO/IZO devices to the ideal diode equation, the apparent shunt resistance was larger in the light than in the dark. This is demonstrated in Figure 6.12. This can be caused by a photoconductive connection between the front and

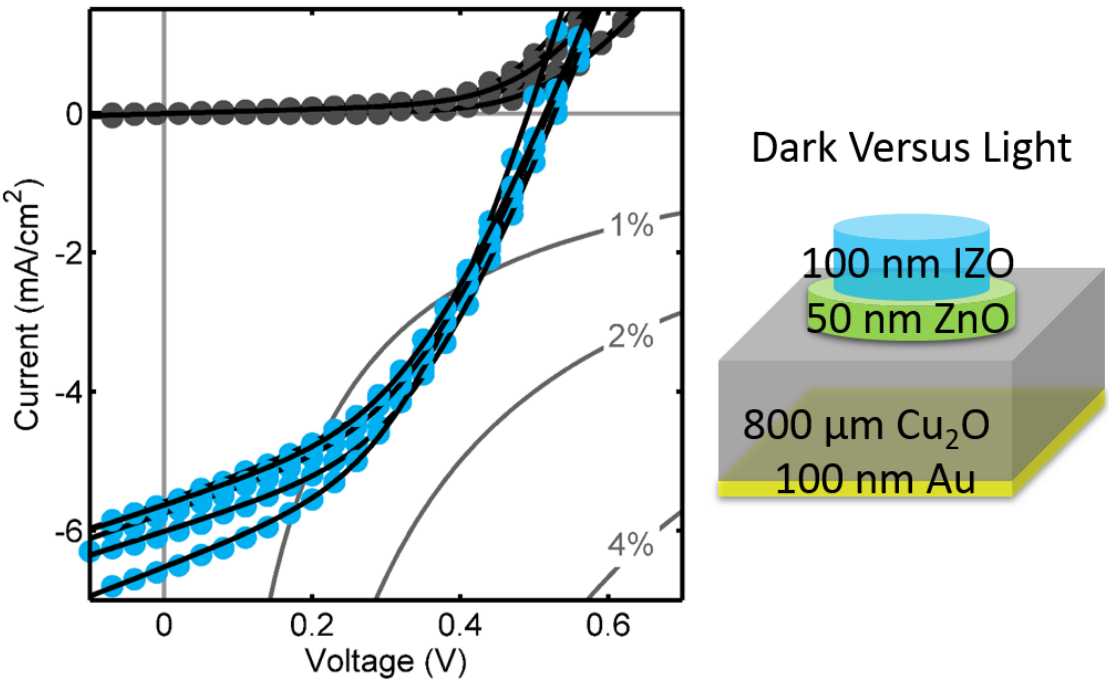

Fitting Parameter	IZO Top Contact, Light	IZO Top Contact, Dark
I_0	$4.6*10^{-9} \pm 1.8*10^{-9}$A	$1.1*10^{-9} \pm 0.6*10^{-9}$A
R_S	1380 ± 160 Ω	1405 ± 125 Ω
R_{Sh}	12,000 ± 800 Ω	171,000 ± 51,000 Ω
J_L	6.7 ± 1.0 mA/cm^2	0 A
n	2	2
Fill Factor	41.7% ± 0.5%	-
V_{OC}	516 ± 15 mV	-
J_{SC}	5.90 ± 0.39 mA/cm^2	-
Efficiency	1.27% ± 0.07%	-

Figure 6.12: Au/Cu_2O/ZnO/IZO devices both in the dark and under 1-sun AM 1.5 G illumination. The shunt resistance (R_{Sh}) seemingly decreases under illumination for unknown reasons. We suspect that there is possibly bias dependent collection occurring, and what looks like an effective shunt resistance is actually the result of a short diffusion length.

back contact, but a far more likely reason is bias dependent collection. This occurs when the minority carrier diffusion length is on the order of the depletion width in the absorber layer. Cu_2O has a very small carrier concentration, even under illumination. The carrier population in Cu_2O is about 10^{14} cm^{-3} [67], while the carrier population in ZnO is around 10^{17} cm^{-3} [47]. Thus most of the band bending in the junction occurs in the Cu_2O, and according to the solution to the 1-dimensional Poisson equations, which is shown in Figure 6.4, the space charge region extends over 2 μm into Cu_2O. The reported diffusion lengths for Cu_2O are also on the order of several microns [10, 42]. Because the space charge region has a large field associated with it, collection of carriers absorbed in it is artificially high. Essentially the effective collection length is the width of the space charge region plus the carrier diffusion length, because as soon as a minority carrier reaches the edge of the field it is immediately swept through the junction by the high field in the depletion width. As the junction is put into forward bias the width of the space charge region decreases, and this also decreases the effective collection length.

The dark versus light J-V curves for ZnO/Cu_2O junctions and the fit of the curves to the ideal diode equation can be seen in Figure 6.12. Bias dependent collection gives J-V curves a tilt around J_{SC} that can be modeled as a small shunt resistance, but the presence of an actual photo-active shunt is physically unlikely. Additionally, bias dependent collection has been identified previously in Cu_2O devices with diffusion lengths below 1 micron [32].

The most likely cause of bias dependent collection is a small diffusion length. Thermally oxidized Cu_2O is known for having a long diffusion length, thus we would expect bias dependent collection to not be an issue. However, we also have seen evidence of chlorine in most XPS of the Cu_2O surface. A low resolution survey scan showing the chlorine can be seen in Figure 6.13. Chlorine is one of the few impurities that is well known to decrease the diffusion length of Cu_2O [11]. We think that elimination of chlorine contamination in our system could greatly reduce the bias dependence and increase the fill factor.

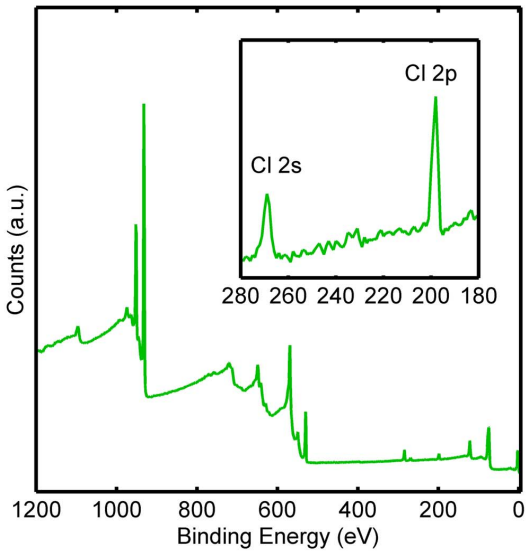

Figure 6.13: Low-resolution X-ray photoelectron spectroscopy spectrum of Cu_2O air-exposed surface. Analysis of the surface composition shows that the surface is around 1% chlorine. It is unknown if the chlorine is only present on the surface, but it is likely also present in some concentration in the bulk of the material. Chlorine contamination has previously been shown to lower diffusion lengths for thermally annealed Cu_2O significantly[11].

6.3.4 Review of Efforts to Increase the Fill Factor

Fill factor describes the square character of the J-V curve and is generally affected by series resistance and shunt resistance. We analyzed two of the most common sources of series resistance in a photovoltaic cell, the TCO and the contribution from the bulk wafer. Resistance from the bulk wafer was found to be the primary source of series resistance in the Cu_2O cells. But there seems to be a secondary source of series resistance that is due to junction formation. We could account for 800 Ω of series resistance due to the bulk wafer, but an additional 600 Ω of series resistance seems to arise from the formation of the junction itself. We were unable to track down the source of this series resistance, but we speculate that there could be several causes. There could be a secondary reactive species forming at the interface, such as some Cu-Zn-O compound that is highly resistive. However, we do not see evidence for the formation of another reactive species in XPS. Additionally, the contact between the ZnO and the TCO could be more resistive then anticipated, although a highly resistive contact between intrinsically doped ZnO and IZO would be unprecedented in literature. There also could be a series resistance contribution from formation of the space charge region. It is usually assumed that there is no power loss when current flows through the space charge region, but the space charge region for Cu_2O is large and the bias across it is diffuse. It could be acting as an essentially intrinsic interfacial region which is highly resistive. In addition to concerns about series resistance, the shunt resistance of the illuminated devices is also an order of magnitude smaller then the dark devices. The most likely reason for this is bias dependent collection, which does have precedence in Cu_2O literature [11].

6.4 Zn(O,S)/Cu_2O Photovoltaic Devices

We were able to reach the voltage entitlement for ZnO/Cu_2O devices by manipulating the interface stoichiometry, as demonstrated above. However, the maximum voltage of a ZnO/Cu_2O device was quite limited due to band alignment of the two materials,

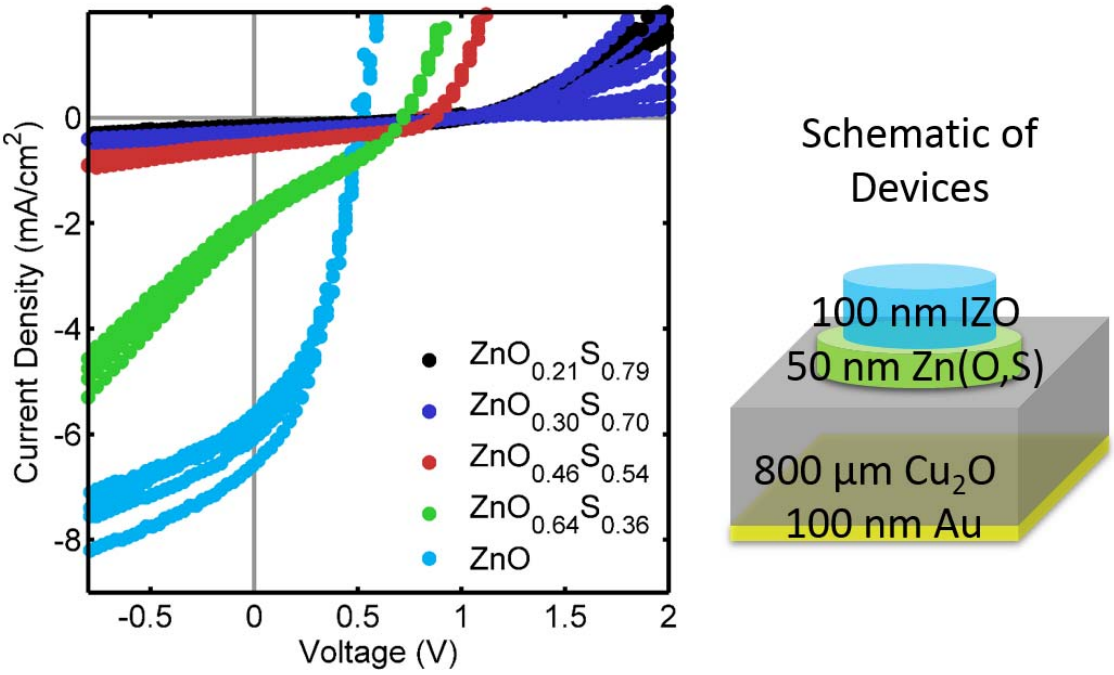

Zn(O,S) Composition	Measured V_{OC}	Modeled I_0
ZnO	517 ± 15 mV	$4.6*10^{-9} \pm 1.8*10^{-9}$A
$ZnO_{0.64}S_{0.36}$	710 ± 10 mV	$5.4*10^{-12} \pm 1.1*10^{-12}$ A
$ZnO_{0.46}S_{0.54}$	857 ± 28 mV	$2.5*10^{-13} \pm 0.3*10^{-13}$ A
$ZnO_{0.30}S_{0.70}$	1011 ± 18 mV	$1.4*10^{-15} \pm 1.7*10^{-15}$ A
$ZnO_{0.21}S_{0.79}$	1013 ± 18 mV	$3.3*10^{-15} \pm 1.1*10^{-15}$ A

Figure 6.14: Current density-voltage (J-V) characteristics for Au/Cu_2O/Zn(O,S)/IZO devices. The composition of the 50 nm Zn(O,S) buffer layer is indicated. The open-circuit voltage (V_{OC}) of the devices increases continuously with increasing sulfur concentration. The J-V curves were fit to the ideal diode equation with a series and shunt resistance term to extract the reverse saturation current of the diodes. This term decreased with increasing sulfur concentration, accounting for the gains in V_{OC}.

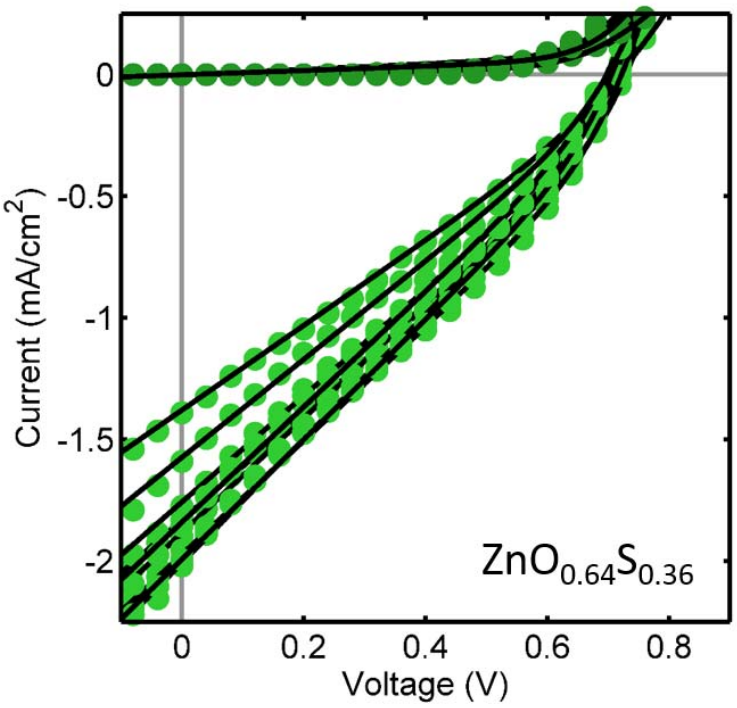

Fitting Parameter	$ZnO_{0.64}S_{0.36}$, Light	$ZnO_{0.64}S_{0.36}$, Dark
I_0	$5.4*10^{-12} \pm 1.1*10^{-12}$ A	$4.2*10^{-12} \pm 1.2*10^{-12}$ A
R_S	3070 ± 2100 Ω	4860 ± 3080 Ω
R_{Sh}	19,500 ± 1200 Ω	660,000 ± 280,000 Ω
J_L	2.07 ± 0.14 mA/cm^2	0 A
n	2	2
Fill Factor	28.2% ± 0.5%	-
V_{OC}	710 ± 10 mV	-
J_{SC}	1.80 ± 0.21 mA/cm^2	-
Efficiency	0.36% ± 0.05%	-

Figure 6.15: Current density-voltage (J-V) characteristics for $Au/Cu_2O/ZnO_{0.64}S_{0.36}$/IZO devices and fitting parameters.

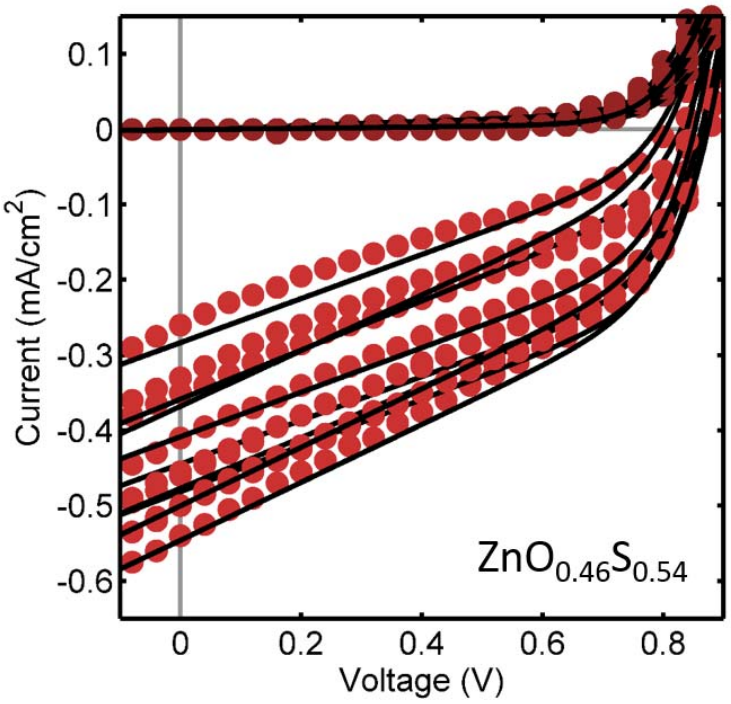

Fitting Parameter	$ZnO_{0.46}S_{0.54}$, Light	$ZnO_{0.46}S_{0.54}$, Dark
I_0	$2.5*10^{-13} \pm 0.3*10^{-13}$ A	$2.6*10^{-13} \pm 0.6*10^{-13}$ A
R_S	3700 ± 1600 Ω	9780 ± 1700 Ω
R_{Sh}	150,000 ± 1800 Ω	4,240,000 ± 1,810,000 Ω
J_L	0.44 ± 0.08 mA/cm^2	0 A
n	2	2
Fill Factor	37.5% ± 0.05%	-
V_{OC}	857 ± 28 mV	-
J_{SC}	0.43 ± 0.08 mA/cm^2	-
Efficiency	0.14% ± 0.04%	-

Figure 6.16: Current density-voltage (J-V) characteristics for $Au/Cu_2O/ZnO_{0.46}S_{0.54}$/IZO devices and fitting parameters.

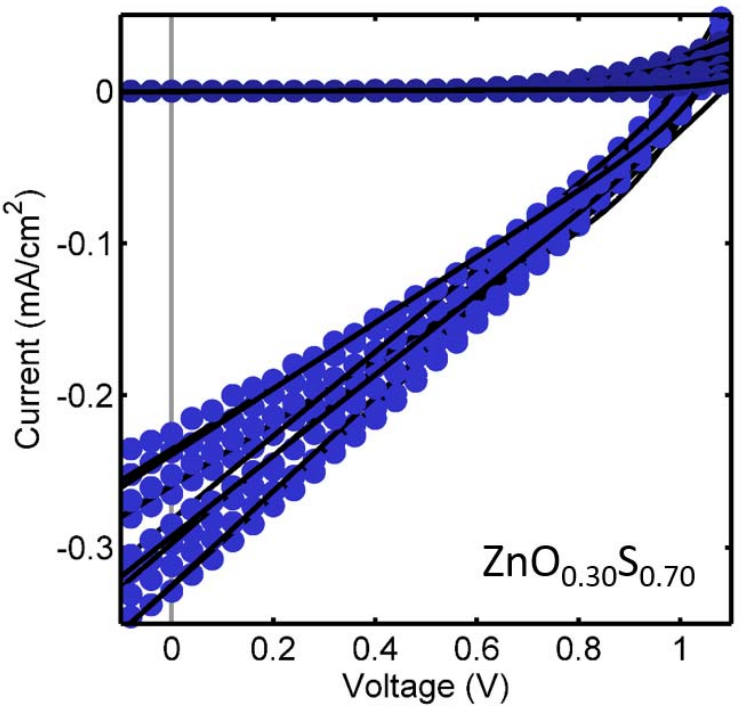

Fitting Parameter	$ZnO_{0.30}S_{0.70}$, Light	$ZnO_{0.30}S_{0.70}$, Dark
I_0	$1.4*10^{-15} \pm 1.7*10^{-15}$ A	$7.3*10^{-15} \pm 11.6*10^{-15}$ A
R_S	43,000 ± 23,000 Ω	462,000 ± 201,000 Ω
R_{Sh}	156,000 ± 43,000 Ω	35,500,000 ± 22,500,000 Ω
J_L	0.38 ± 0.12 mA/cm^2	0 A
n	2	2
Fill Factor	26.8% ± 1.9%	-
V_{OC}	1011 ± 18 mV	-
J_{SC}	0.28 ± 0.04 mA/cm^2	-
Efficiency	0.08% ± 0.01%	-

Figure 6.17: Current density-voltage (J-V) characteristics for $Au/Cu_2O/ZnO_{0.30}S_{0.70}/IZO$ devices and fitting parameters.

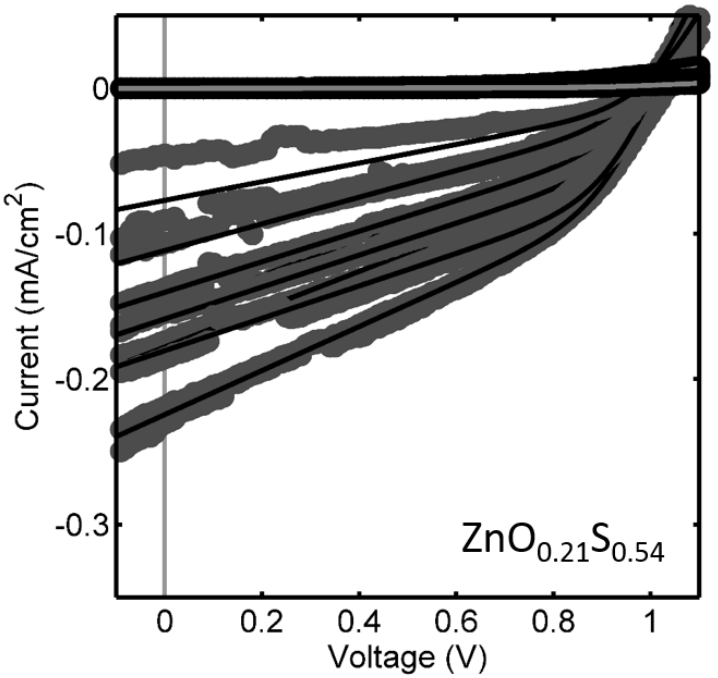

Fitting Parameter	$ZnO_{0.21}S_{0.79}$, Light	$ZnO_{0.21}S_{0.79}$, Dark
I_0	$4.1*10^{-15} \pm 1.2*10^{-15}$ A	$2.6*10^{-15} \pm 1.6*10^{-15}$ A
R_S	35,000 ± 2,900 Ω	820,000 ± 190,000 Ω
R_{Sh}	400,000 ± 77,000 Ω	20,600,000 ± 6,400,000 Ω
J_L	0.18 ± 0.05 mA/cm^2	0 A
n	2	2
Fill Factor	25.8% ± 0.7%	-
V_{OC}	10113 ± 18 mV	-
J_{SC}	0.13 ± 0.07 mA/cm^2	-
Efficiency	0.04% ± 0.03%	-

Figure 6.18: Current density-voltage (J-V) characteristics for $Au/Cu_2O/ZnO_{0.21}S_{0.79}$/IZO devices and fitting parameters.

as discussed in Chapter 5. Because we believed the chemistry between Zn and Cu was favorable for interface formation, as demonstrated in Chapter 4, we also tested the band offset with ZnSe and ZnS. We found that ZnSe had a favorable band offset with Cu_2O, but was reactive with the interface and was also impossible to contact. ZnS formed a stoichiometric interface, but had too large of a conduction band spike for efficient injection of minority carriers across the interface. However, based on the alignment of the ZnS and ZnO conduction bands with Cu_2O, we believed a Zn(O,S) alloy could have potential as a heterojunction partner. Furthermore this alloy had already been demonstrated to have a continuously tunable conduction band offset with CIGS devices [21, 29, 40]. Thus we decided to pursue Zn(O,S) as a heterojunction partner due to the favorable chemistry of Cu_2O with Zn, the demonstrated ability of ZnO and ZnS to form a stoichiometric interface with Cu_2O, and the previous success of Zn(O,S) as a heterojunction partner in CIGS devices.

6.4.1 Review of Current-Voltage Character of Zn(O,S)/Cu_2O Heterojunctions

The Zn(O,S) used in these experiments was fabricated according to the procedure in Chapter 3. Photovoltaic devices were made according to the processing steps outlined previously in this chapter. In brief, 50 nm of Zn(O,S) was deposited directly onto untreated Cu_2O wafers followed by 10-20 nm of Zn(O,S) graded to ZnO to make low resistance contact with the IZO top contact. A 100 nm thick Au film was sputtered as a back electrical contact. Current density vs. potential (J-V) measurements on the full photovoltaic devices were performed under AM 1.5G 1-sun illumination. Current-voltage characteristics for these devices are shown in Figure 6.14. The full fittings and device parameters for the individual Zn(O,S) compositions are given in Figures 6.16-6.18. Devices made with ZnO buffer layers had open-circuit voltages of 515 $\pm$15 mV, which was within the error for previous results with ZnO as a buffer layer. As the sulfur composition in the Zn(O,S) increased, the open-circuit voltage increased from 710 $\pm$10 mV to 857 $\pm$28 mV to 1013 $\pm$18 mV. Results were highly reproducible

and voltages were averaged over a minimum of 5, and more typically 9, devices. To our knowledge this is the largest reported open circuit voltage for a device made with a thermally oxidized Cu_2O emitter. This is also the first demonstration of Zn(O,S) as an emitter layer in Cu_2O. The only larger open-circuit voltage ever reported of 1.2 eV was for a device with an electrodeposited Cu_2O absorber layer and a Ga_2O_3 emitter [32]. Zn(O,S) is thus only the second heterojunction partner to reach open-circuit voltages above 1 V, and it is the first heterojunction partner composed of widely produced elements to reach these voltages.

However, though the voltages increase fairly linearly with sulfur concentration, the current density decreases greatly. We were unable to fully determine the cause of this, but we believe the answer at least partially lies in the X-ray photoelectron spectroscopy analysis of the Zn(O,S)/Cu_2O interface. The data, seen in Figure 4.13, shows the formation of SO_4^{2-} at the interface. This occurs when the Zn(O,S) reduces the CuO on the surface of the air-exposed Cu_2O. The enthalpy of formation data for thermodynamically stable species in the Cu-Zn-S-O compound family was listed in Table 4.1. $ZnSO_4$ had by for the highest heat of formation for the listed compounds. We synthesized this compound, and the optical data for it is shown in Figure 3.17. The band gap expanded quite dramatically with limited oxygen. Thus, we speculate that the formation of $ZnSO_4$ at the interface is causing a conduction band spike and impeding current flow.

6.4.2 Modeling Implied Open-Circuit Voltage for Zn(O,S)/Cu_2O Heterojunctions

The open-circuit voltage for the Zn(O,S)/Cu_2O devices reported above is greatly limited by the low light generated current, reflected in the small value for short circuit current. Open-circuit voltage is defined by the ratio of light generated current to reverse saturation current, as is described by the following equation, which is repeated from above:

$$V_{OC} = \frac{nkT}{q} \ln\left(\frac{I_L}{I_0} + 1\right)$$

Composition of Zn(O,S) Composition	Average V_{OC}	Modeled I_0	Implied V_{OC}
ZnO	517 ± 15 mV	$4.6*10^{-9} \pm 1.8*10^{-9}$A	555 ± 15 mV
$ZnO_{0.64}S_{0.36}$	710 ± 10 mV	$5.4*10^{-12} \pm 1.1*10^{-12}$ A	906 ± 10 mV
$ZnO_{0.46}S_{0.54}$	857 ± 28 mV	$2.5*10^{-13} \pm 0.3*10^{-13}$ A	1066 ± 28 mV
$ZnO_{0.30}S_{0.70}$	1011 ± 18 mV	$1.4*10^{-15} \pm 1.7*10^{-15}$ A	1336 ± 18 mV
$ZnO_{0.21}S_{0.79}$	1013 ± 18 mV	$3.3*10^{-15} \pm 1.1*10^{-15}$ A	1291 ± 18 mV

Table 6.2: The implied voltage is calculated for each Zn(O,S) composition based on the modeled value of I_0, a diode ideality factor of 2, and a light generated current term of 0.0002 A, or 10 mA/cm^2. This calculation shows that if we can boost the current of the Zn(O,S)/Cu_2O photovoltaic devices, we are close to the voltage entitlement of Cu_2O.

The band gap of Cu_2O limits the short-circuit current to approximately 17 mA/cm^2 under AM 1.5 1-sun illumination. The most efficient Cu_2O devices have a short-circuit current near 10 mA/cm^2 under this illumination intensity [38, 39]. Thus we also calculate an implied V_{OC} for each Zn(O,S) composition based on the modeled value of I_0, a diode ideality factor of 2, and a light generated current term of 0.0002 A, or 10 mA/cm^2. These calculated values are shown in Table 6.2.The values of implied V_{OC} show how much larger the open-circuit voltage would be if we could increase the device current to 10 mA/cm^2. In fact, the more sulfur rich compositions of Zn(O,S) should be capable of reaching open-circuit voltages over 1.3 V. Thus we believe Zn(O,S) is a very promising heterojunction candidate for high efficiency Cu_2O photovoltaics, even though the devices we have manufactured are actually less efficient then the ZnO/Cu_2O devices we tested previously.

6.5 Summary of Work on Cu_2O Photovoltaic Devices

One of the goals of this thesis research has been to understand the deficits in the open-circuit voltage of Cu_2O photovoltaic devices. Cu_2O has an optical band gap of 1.9 eV. Through detailed balance calculations we conclude the thermodynamic maximum for Cu_2O's open-circuit voltage is approximately 1.6 V. However, the largest demonstrated open-circuit voltage is merely 1.2 V. The work reviewed in this chapter reveals two large limitations to open-circuit voltage in Cu_2O photovoltaic devices: the heterojunction interface stoichiometry and the heterojunction valence band offset. In Chapter 4 we showed how variations in the deposition conditions can alter the stoichiometry of the ZnO/Cu_2O interface. In this chapter we conclude that maintaining phase purity at the Cu_2O interface is essential for achieving the full open-circuit voltage entitlement in ZnO/Cu_2O devices. Alternatively, devices with CuO or copper at the interface have open-circuit voltages that fall far below their voltage entitlement. Thus we demonstrate the necessity of stoichiometric interfaces for large open-circuit voltages.

In Chapter 5 we reviewed valence band offset measurements that indicated the ZnO/Cu_2O junction should have severe voltage limitations due to the heterojunction valence band alignment. These measurements also indicated that adding sulfur could possibly decrease the open-circuit voltage deficit due to band alignment. We indeed find that as we increase the concentration of sulfur in the Zn(O,S), the open-circuit voltage increases. The devices do not have power conversion efficiencies above 1%, but they serve as proof of the promise of Zn(O,S)/Cu_2O heterojunctions for earth-abundant solar conversion. In fact Zn(O,S) is the first earth-abundant solar absorber to achieve an open-circuit voltage greater than 1 V in a Cu_2O photovoltaic device. Simple modeling indicates Zn(O,S)/Cu_2O photovoltaic devices have that potential to reach open-circuit voltages of greater than 1.3 V.

Chapter 7

Summary and Outlook

The work outlined in this thesis comprises two significant achievements in Cu_2O photovoltaic research. The first achievement is a method for fabrication of a stoichiometric interface between Cu_2O and an oxide heterojunction partner. The second is the introduction of Zn(O,S) as a potential high voltage heterojunction partner. We will further explore the significance of these findings after taking a moment to review the motivation for studying Cu_2O as a solar material.

The primary motivation for earth-abundant photovoltaic research is to find a photovoltaic absorber material that can be employed to generate the majority of the electricity the United States consumes annually. In order to reach this goal, a given material must be composed of elements that are primary mining commodities and

the material must be theoretically capable of producing a high efficiency device, as described in Chapter 1. Current commercial thin film solar materials like CIGS and CdTe are composed of elements that are secondary mining commodities and thus most likely can not be used in wide scale energy production. Silicon is the only commercial technology that meets the requirements stated above, however we do not anticipate Cu_2O directly competing with silicon because Cu_2O has an ideal band gap to be a top junction in a silicon dual junction device.

Cu_2O is a favorable solar material because it is manufactured in a low-cost process, it has a suitable band gap for a high energy conversion efficiency, and it is made from primary mining commodities, as described in Chapter 2. This thesis primarily describes the construction of novel Cu_2O absorber-based photovoltaics, from the fundamental material characterization, through the selection and growth of the emitter material, to contact design to device characterization. The first important result in this thesis relates to how to design a Cu_2O heterojunction to maximize device photovoltage. We find that a stoichiometric interface is essential for reaching the voltage entitlement of a ZnO/Cu_2O junction, as is described in Chapter 6. The steps necessary to prepare a stoichiometric junction with a bulk Cu_2O wafer and an oxide emitter material are described in Chapter 4. Briefly, the first step is to prepare the surface such that it is slightly oxidized. We create slightly oxidized Cu_2O surfaces by air-exposing the samples; in literature nitric acid and ammonium persulfate etches are also used to similar effect [37, 39]. Next the emitter is deposited in a reducing atmosphere. We find that if these conditions are met, and the emitter is composed of some combination of Zn, O, and S, stoichiometric interface formation is nearly automatic. We also find the necessary condition for reaching the voltage entitlement dictated by the heterojunction band alignment is a stoichiometric interface [65]. We believe that this formula for junction formation can be reproduced with any other emitter material to form high voltage junctions. Indeed, this method of interface fabrication is cited by the publication that reports the highest open-circuit voltage for a photovoltaic device with a Cu_2O absorber layer [32].

The other main result of this thesis is demonstration of Zn(O,S) as a possible

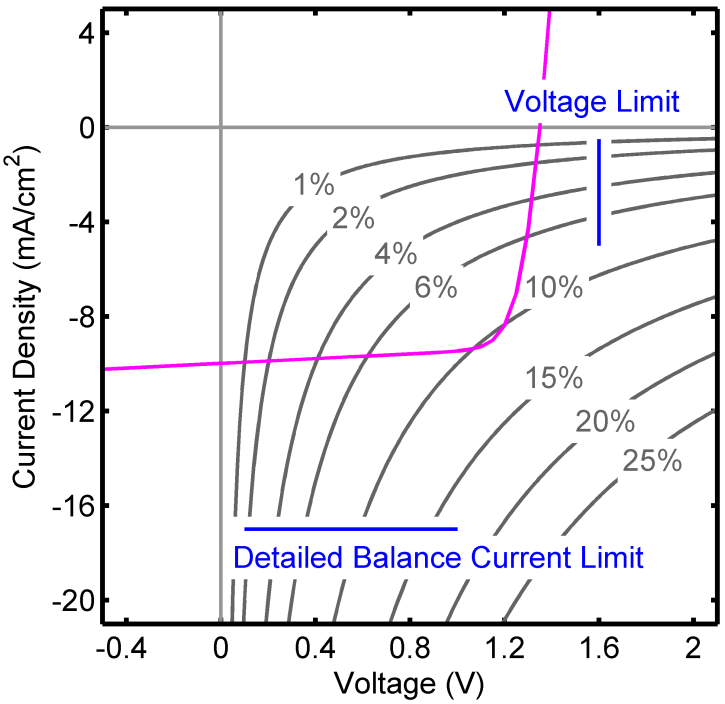

Curve Parameter	Model Value
Fill Factor	76.7%
V_{OC}	1350 mV
J_{SC}	10 mA/cm^2
Efficiency	10.36%

Figure 7.1: The efficiencies of the Cu_2O photovoltaic devices we reviewed in Chapter 6 were not large compared to previous reported devices in literature. However, we believe Zn(O,S)/ Cu_2O devices have the potential to achieve high efficiencies, as we demonstrate in the device model outlined above. This model estimates we could achieve energy conversion efficiencies of over 10% (an improvement over the current 5.38% record) if we could put all of our best devices together. The modeled V_{OC} value, at 1350 mV, would also be a record, as the currently 1200 mV is the largest value reported in literature. The parameters we use in this simulated current-voltage curve have all been achieved in separate devices, and the origin and value of each term is reviewed in Table 7.1.

Fitting Parameter	Simulation Values
I_0	$1*10^{-15}$
R_S	200 Ω
R_{Sh}	100,000 Ω
J_L	10 mA/cm^2
n	2

Table 7.1: The above table lists the value for each term used to produce the simulated current-voltage charcter shown in Figure 7.1. The value for I_0 is derived from current-voltage modeling of the $ZnO_{0.30}S_{0.70}/Cu_2O$ junction, and is reported in Chapter 6. R_S is set at 200 Ω to represent the series resistance contribution of a 200 μm thick Cu_2O wafer. 100,000 Ω is a value we commonly achieve for R_{Sh}. Diode ideality factor is consistently 2, thus we believe modeling another value would be unreasonable. Finally, 10 mA/cm^2 is a short-circuit current commonly achieved in high efficiency Cu_2O devices. A device area of 2 mm^2 is assumed for the calculation.

emitter material for a Cu_2O photovoltaic device. To the best of our knowledge, Zn(O,S) is the first earth-abundant heterojunction partner to be employed in Cu_2O device with an open-circuit voltage greater than 1.0 V. Ga_2O_3 has demonstrated voltages up to 1.2 V with Cu_2O [32], but Ga_2O_3 is not an earth-abundant material, as we review in Chapters 1 and 3. We speculate further study of Zn(O,S)/Cu_2O devices will allow us to partner the high open-circuit voltage already achieved with a high current, large fill factor, and high energy conversion efficiency. Figure 7.1 shows a modeled Zn(O,S)/Cu_2O junction. For the simulation, we use previously measured values for saturation current (I_0), diode ideality factor (n), and shunt resistance (R_{Sh}), the specific devices are reviewed in Chapter 6. Additionally we use values for R_S and I_L that have already been achieved in ZnO/Cu_2O devices to simulate a current-voltage character we could reasonably expect to achieve with a Zn(O,S)/Cu_2O device. The results show that if we could combine the best parameters from ZnO/Cu_2O devices reported in literature and the Zn(O,S)/Cu_2O devices we reviewed in Chapter 6, we

could reach a new record efficiency for Cu_2O. Though we have not yet been able to demonstrate high efficiency Zn(O,S)/Cu_2O devices, Zn(O,S) easily merits more study due to its undeniable potential as a heterojunction partner.

Appendix A

This appendix summarizes the data that was used to build Figure 3.1. No heat of formation data was available for several species. In the case of Au, Pt, Ar, etc. the oxide will not form probably due to a positive heat of formation. In the case of Cn, Rg, Ds etc. the species are not abundant enough in the earth's crust for heat of formation data to have been measured. Special notes on reactivity or toxicity are also recorded.

Z	Symbol	Element	Oxide Species	Heat of Formation of Oxide (kJ/mol)	Notes
1	H	Hydrogen	H_2O	-286	Liquid
2	He	Helium	-	-	No heat of formation data
3	Li	Lithium	Li_2O	-599	
			Li_2O_2	-633	
4	Be	Beryllium	BeO	-608	
5	B	Boron	B_2O_3	-1272	
6	C	Carbon	CO	-122	gas
			C_2O	287	gas

			CO_2	-394	gas
			C_3O_2	-94	gas
7	N	Nitrogen	N_2O_4	-35	liquid
			N_2O	82	gas
			N_2O_3	83	gas
			N_2O_5	11	gas
			NO	90	gas
			NO_3	71	gas
			NO_2	33	gas
8	O	Oxygen	O_2		gas
9	F	Fluorine	F_2O	24	gas
			FO	108	gas
10	Ne	Neon	-		No heat of formation data
11	Na	Sodium	Na_2O	-418	Corrosive, reacts with water powerful oxidizer
			Na_2O_2	-513	
			NaO_2	-261	
12	Mg	Magnesium	MgO	-601	
13	Al	Aluminum	Al_2O_3	-1676	
14	Si	Silicon	SiO_2	-911	
15	P	Phosphorus	P_4O_{10}	-3010	gas, very reactive with water
			PO_2	-315	
			PO	-24	
16	S	Sulfur	SO_2	-297	gas
			SO_3	257	gas
			S_2O	-56	gas
			SO	5	gas

17	Cl	Chlorine	Cl_2O	88	gas
			ClO	101	gas
			ClO_2	105	gas
18	Ar	Argon	-		No heat of formation data
19	K	Potassium	K_2O	-363	Corrosive, reacts violently with water
			K_2O_2	-496	
			KO_2	-285	
20	Ca	Calcium	CaO	-635	Reactive with water, air
21	Sc	Scandium	Sc_2O_3	-1909	
22	Ti	Titanium	TiO_2 (R)	-939	
			TiO_2 (A)	-939	
			Ti_2O_3	-1521	
			Ti_3O_5	-2459	
			Ti_4O_7	-3405	
			TiO	-543	
23	V	Vanadium	V_2O_3	-1219	
			V_2O_5	-1551	
			VO	-432	
24	Cr	Chromium	Cr_2O_3	-1135	
25	Mn	Manganese	MnO	-385	
			MnO_2	-520	
			Mn_2O_3	-959	
			Mn_3O_4	-1388	
26	Fe	Iron	Fe_2O_3	-826	

			Fe_3O_4	-1121	
			FeO	-272	
27	Co	Cobalt	Co_3O_4	-910	
			CoO	-238	
28	Ni	Nickel	NiO	-240	
			Ni_2O_3	-540	
29	Cu	Copper	Cu_2O	-171	
			CuO	-156	
30	Zn	Zinc	ZnO	-350	
31	Ga	Gallium	Ga_2O_3	-1089	
32	Ge	Germanium	GeO_2	-580	
33	As	Arsenic	As_2O_3	-657	toxic
34	Se	Selenium	SeO_2	-225	toxic
35	Br	Bromine	BrO	125	gas
			BrO_2	152	gas
36	Kr	Krypton	-		No heat of formation data
37	Rb	Rubidium	Rb_2O	-339	Highly reactive with water
			RbO_2	-278	
			Rb_2O_2	-472	
38	Sr	Strontium	SrO	-592	
39	Y	Yttrium	Y_2O_3	-1905	
40	Zr	Zirconium	ZrO_2	-1097	
41	Nb	Niobium	Nb_2O_5	-1900	
			NbO	-420	
			NbO_2	-795	
42	Mo	Molybdenum	MoO_2	-588	

			MoO_3	-745	
43	Tc	Technetium	-		No heat of formation data
44	Ru	Ruthenium	RuO_2	-305	
45	Rh	Rhodium	Rh_2O_3	-343	
46	Pd	Palladium	PdO	-85	
47	Ag	Silver	Ag_2O	-31	
			Ag_2O_2	-24	
			Ag_2O_3	33	
48	Cd	Cadmium	CdO	-258	
49	In	Indium	In_2O_3	-926	
50	Sn	Tin	SnO_2	-578	
			SnO	-280	
51	Sb	Antimony	Sb_2O_5	-972	
52	Te	Tellurium	TeO_2	-323	
53	I	Iodine			No heat of formation data
54	Xe	Xenon			No heat of formation data
55	Cs	Caesium	CsO_2	-286	Reacts violently with water
			Cs_2O	-346	
56	Ba	Barium	BaO	-548	
57	La	Lanthanum	La_2O_3	-1794	reacts violently with water
58	Ce	Cerium	CeO_2	-1089	
			Ce_2O_3	-1796	

59	Pr	Praseodymium	Pr_2O_3	-1810	
60	Nd	Neodymium	Nd_2O_3	-1808	
61	Pm	Promethium			No heat of formation available
62	Sm	Samarium	Sm_2O_3	-1823	
63	Eu	Europium	Eu_2O_3	-1651	Toxic
64	Gd	Gadolinium	Gd_2O_3	-1820	Eye irritant
65	Tb	Terbium	Tb_4O_7	-1865	
66	Dy	Dysprosium	Dy_2O_3	-1863	
67	Ho	Holmium	Ho_2O_3	-1881	
68	Er	Erbium	Er_2O_3	-1898	
69	Tm	Thulium	Tm_2O_3	-1889	
70	Yb	Ytterbium	Yb_2O_3	-1815	
71	Lu	Lutetium	Lu_2O_3	-1878	
72	Hf	Hafnium	HfO_2	-1145	
73	Ta	Tantalum	Ta_2O_5	-2046	
74	W	Tungsten	WO_3	-843	
75	Re	Rhenium	Re_2O_7	-1240	
76	Os	Osmium	OsO_4	-394	
77	Ir	Iridium	IrO_2	-274	
78	Pt	Platinum	-		No heat of formation data
79	Au	Gold			No heat of formation data
80	Hg	Mercury	HgO	-91	
81	Tl	Thallium	Tl_2O	-179	

82	Pb	Lead	PbO_2 Pb_3O_4 PbO	-277 -718 -219	Toxic
83	Bi	Bismuth	Bi_2O_3	-574	
84	Po	Polonium			No heat of formation data
85	At	Astatine			No heat of formation data
86	Rn	Radon			No heat of formation data
87	Fr	Francium			No heat of formation data
88	Ra	Radium	RaO	-523	
89	Ac	Actinium			No heat of formation data
90	Th	Thorium	ThO_2	-1226	
91	Pa	Protactinium			No heat of formation data
92	U	Uranium	UO_2 UO_3	-1085 -1224	Toxic
93	Np	Neptunium			No heat of formation data
94	Pu	Plutonium			No heat of formation data
95	Am	Americium			No heat of formation data

96	Cm	Curium	No heat of formation data
97	Bk	Berkelium	No heat of formation data
98	Cf	Californium	No heat of formation data
99	Es	Einsteinium	No heat of formation data
100	Fm	Fermium	No heat of formation data
101	Md	Mendelevium	No heat of formation data
102	No	Nobelium	No heat of formation data
103	Lr	Lawrencium	No heat of formation data
104	Rf	Rutherfordium	No heat of formation data
105	Db	Dubnium	No heat of formation data
106	Sg	Seaborgium	No heat of formation data
107	Bh	Bohrium	No heat of formation data
108	Hs	Hassium	No heat of formation data

109	Mt	Meitnerium	No heat of formation data
110	Ds	Darmstadtium	No heat of formation data
111	Rg	Roentgenium	No heat of formation data
112	Cn	Copernicium	No heat of formation data

Appendix B

This appendix contains raw data on abundance in ppm and production in metric tons. Data is from USGS and was compiled by Wikipedia.

Z	Symbol	Element	Abundance	Production
1	H	Hydrogen	1400	
2	He	Helium		
3	Li	Lithium	20	37000
4	Be	Beryllium	2.8	230
5	B	Boron	10	4600000
6	C	Carbon	200	
7	N	Nitrogen	19	137000000
8	O	Oxygen	461000	
9	F	Fluorine	585	
10	Ne	Neon		
11	Na	Sodium	23600	280000000
12	Mg	Magnesium	23300	750000
13	Al	Aluminum	82300	44900000
14	Si	Silicon	282000	7600000
15	P	Phosphorus	1050	

16	S	Sulfur	350	70000000
17	Cl	Chlorine	145	280000000
18	Ar	Argon		
19	K	Potassium	20900	34000
20	Ca	Calcium	41500	
21	Sc	Scandium	22	
22	Ti	Titanium	5600	6500000
23	V	Vanadium	120	63000
24	Cr	Chromium	102	7890000
25	Mn	Manganese	950	16000000
26	Fe	Iron	56300	1100000000
27	Co	Cobalt	25	110000
28	Ni	Nickel	84	2100000
29	Cu	Copper	60	17000000
30	Zn	Zinc	70	13000000
31	Ga	Gallium	19	
32	Ge	Germanium	1.5	128
33	As	Arsenic	1.8	44000
34	Se	Selenium	0.05	2000
35	Br	Bromine	2.4	580000
36	Kr	Krypton		
37	Rb	Rubidium	90	
38	Sr	Strontium	370	380000
39	Y	Yttrium	33	8900
40	Zr	Zirconium	165	1420000
41	Nb	Niobium	20	69000

42	Mo	Molybdenum	1.2	250000
43	Tc	Technetium		
44	Ru	Ruthenium	0.001	
45	Rh	Rhodium	0.001	
46	Pd	Palladium	0.015	200
47	Ag	Silver	0.075	24000
48	Cd	Cadmium	0.15	23000
49	In	Indium	0.25	670
50	Sn	Tin	2.3	230000
51	Sb	Antimony	0.2	180000
52	Te	Tellurium	0.001	
53	I	Iodine	0.45	28000
54	Xe	Xenon		
55	Cs	Caesium	3	
56	Ba	Barium	425	
57	La	Lanthanum	39	
58	Ce	Cerium	66.5	
59	Pr	Praseodymium	9.2	
60	Nd	Neodymium	41.5	
61	Pm	Promethium		
62	Sm	Samarium	7.05	
63	Eu	Europium	2	
64	Gd	Gadolinium	6.2	
65	Tb	Terbium	1.2	
66	Dy	Dysprosium	5.2	
67	Ho	Holmium	1.3	

68	Er	Erbium	3.5	
69	Tm	Thulium	0.52	
70	Yb	Ytterbium	3.2	
71	Lu	Lutetium	0.5	
72	Hf	Hafnium	3	
73	Ta	Tantalum	2	765
74	W	Tungsten	1.25	73000
75	Re	Rhenium	0.0007	52
76	Os	Osmium	0.0015	
77	Ir	Iridium	0.001	
78	Pt	Platinum	0.005	179
79	Au	Gold	0.004	2700
80	Hg	Mercury	0.085	1600
81	Tl	Thallium	0.85	10
82	Pb	Lead	14	5200000
83	Bi	Bismuth	0.0085	7400
84	Po	Polonium		
85	At	Astatine		
86	Rn	Radon		
87	Fr	Francium		
88	Ra	Radium		
89	Ac	Actinium		
90	Th	Thorium	9.6	
91	Pa	Protactinium		
92	U	Uranium	2.7	66512
93	Np	Neptunium		

94	Pu	Plutonium
95	Am	Americium
96	Cm	Curium
97	Bk	Berkelium
98	Cf	Californium
99	Es	Einsteinium
100	Fm	Fermium
101	Md	Mendelevium
102	No	Nobelium
103	Lr	Lawrencium
104	Rf	Rutherfordium
105	Db	Dubnium
106	Sg	Seaborgium
107	Bh	Bohrium
108	Hs	Hassium
109	Mt	Meitnerium
110	Ds	Darmstadtium
111	Rg	Roentgenium
112	Cn	Copernicium

Bibliography

[1] National Renewable Energy Lab. `www.nrel.gov`, 2014. [Online; accessed November 2014].

[2] Solar Frontier. `www.solar-frontier.com/eng/products/index.html`, 2014. [Online; accessed November 2014].

[3] United States Energy Information Administration. `www.eia.gov`, 2014. [Online; accessed October 2014].

[4] United States Geological Survery. `www.usgs.gov`, 2014. [Online; accessed September 2014].

[5] R. L. Anderson. "Germanium-gallium arsenide heterojunction". *IBM Journal OF Research and Development*, 4(3):283–287, 1960.

[6] J. A. Assimos and D. Trivich. "Photovoltaic properties and barrier heights of single crystal and polycrystalline Cu_2O/Cu contacts". *Journal of Applied Physics*, 44(4):1687–1693, 1973.

[7] J. D. Beach and B. E. McCandless. "Materials challenges for CdTe and $CuInSe_2$ photovoltaics". *MRS Bulletin*, 32:225–229, 3 2007.

[8] A. A. Berezin and M. Fujinaka. "Cuprous oxide-indium tin oxide thin film photovoltaic cells". *Journal of Applied Physics*, 54(6):7, 1983.

[9] A. A. Berezin and F. L. Weichman. "Photovoltaic effect in cuprous oxide-copper junctions in relation to the optical absorption spectrum of cuprous oxide". *Solid State Communications*, 37(2):157–160, 1981.

[10] F. Biccari. "Defects and doping in Cu_2O". *University of Rome*, 2009.

[11] F. Biccari, C. Malerba, and A. Mittiga. "Chlorine doping of Cu_2O". *Solar Energy Materials and Solar Cells*, 94(11):1947–1952, 2010.

[12] J. P. Bosco, S. B. Demers, G. M. Kimball, N. S. Lewis, and H. A. Atwater. "Band alignment of epitaxial ZnS/Zn_3P_2 heterojunctions". *Journal of Applied Physics*, 112(9):093703, 2012.

[13] J. P. Bosco, D. O. Scanlon, G. W. Watson, N. S. Lewis, and H. A. Atwater. "Energy-band alignment of II-VI/Z_3P_2 heterojunctions from x-ray photoemission spectroscopy". *Journal of Applied Physics*, 113(20), 2013.

[14] M. W. Chase. "NIST-JANAF thermochemical tables", 1998.

[15] S. K. Chawla, N. Sankarraman, and J. H. Payer. "Diagnostic spectra for XPS analysis of Cu-O-S-H compounds". *Journal of Electron Spectroscopy and Related Phenomena*, 61(1):1–18, 1992.

[16] B. D. Cullity and S. R. Stock. *Elements of X-ray Diffraction*. Addison-Wesley Publishing Company, Inc., Reading, Massacusetts, 1956.

[17] Z. Duan, A. Du Pasquier, Y. Lu, Y. Xu, and E. Garfunkel. "Effects of Mg composition on open-circuit voltage of $Cu_2O/Mg_xZn_{1-x}O$ heterojunction solar cells". *Solar Energy Materials and Solar Cells*, 96:292–297, 2012.

[18] A. Franciosi and C. G. VandeWalle. "Heterojunction band-offset engineering". *Surface Science Reports*, 25, 1996.

[19] Y. Fu, H. Lei, X. Wang, D. Yan, L. Cao, G. Yao, C. Shen, L. Peng, Y. Zhao, Y. Wang, and W. Wu. "Fabrication of two domain Cu_2O films on MgO by pulsed laser deposition". *Applied Surface Science*, 273(0):19 – 23, 2013.

[20] M. A. Green. *Third Generation Photovoltaics: Advanced Solar Energy Conversion*. Springer Berlin Heidelberg, Berlin, Germany, 2003.

[21] A. Grimm, D. Kieven, R. Klenk, I. Lauermann, A. Neisser, T. Niesen, and J. Palm. "Junction formation in chalcopyrite solar cells by sputtered wide gap compound semiconductors". *Thin Solid Films*, 520(4):1330–1333, 2011.

[22] A. Grimm, D. Kieven, I. Lauermann, M. Ch Lux-Steiner, F. Hergert, R. Schwieger, and R. Klenk. "Zn(O,S) layers for chalcoyprite solar cells sputtered from a single target". *EPJ Photovoltaics*, 3(30302):30302, 2012.

[23] Y. B. He, L. H. Wang, L. Zhang, M. K. Li, X. Z. Shang, Y. Y. Fang, and C. Q. Chen. "Solubility limits and phase structures in epitaxial Zn(O,S) alloy films grown by pulsed laser deposition". *Journal of Alloys and Compounds*, 534:81–85, 2012.

[24] C. Honsberg and S. Bowden. "PVCDROM". `www.pvcdrom.com`, 2014. [Online; accessed November 2014].

[25] M. Ichimura and Y. Song. "Band alignment at the Cu_2O/ZnO heterojunction". *Japanese Journal of Applied Physics*, 50(5):051002, 2011.

[26] M. Izaki, T. Shinagawa, K.T. Mizuno, Y. Ida, M. Inaba, and A. Tasaka. "Electrochemically constructed p-Cu_2O/n-ZnO heterojunction diode for photovoltaic device". *Journal of Physics D: Applied Physics*, 40(11):4, 2007.

[27] K. Jacobi, G. Zwicker, and A. Gutmann. "Work function, electron affinity and band bending of zinc oxide surfaces". *Surface Science*, 141(1):109–125, 1984.

[28] S. S. Jeong, A. Mittiga, E. Salza, A. Masci, and S. Passerini. "Electrodeposited ZnO/Cu_2O heterojunction solar cells". *Electrochimica Acta*, 53(5):2226–2231, 2008.

[29] D. Kieven, A. Grimm, I. Lauermann, M. C. Lux-Steiner, J. Palm, T. Niesen,

and R. Klenk. "Band alignment at sputtered ZnS_xO_{1-x}/CIGS heterojunctions". *Physica Status Solidi-Rapid Research Letters*, 6(7):294–296, 2012.

[30] J. Y. Kim, J. A. Rodriguez, J. C. Hanson, A. I. Frenkel, and P. L. Lee. "Reduction of CuO and Cu_2O with H_2: H embedding and kinetic effects in the formation of suboxides". *Journal of the American Chemical Society*, 125(35):10684–92, 2003.

[31] E. Kraut, R. Grant, J. Waldrop, and S. Kowalczyk. "Semiconductor core-level to valence-band maximum binding-energy differences: Precise determination by X-ray photoelectron spectroscopy". *Physical Review B*, 28(4):1965–1977, 1983.

[32] Y. S. Lee, D. Chua, R. E. Brandt, S. C. Siah, J. V. Li, J. P. Mailoa, S. W. Lee, R. G. Gordon, and T. Buonassisi. "Atomic layer deposited gallium oxide buffer layer enables 1.2 V open-circuit voltage in cuprous oxide solar cells". *Advanced Materials*, 26(27):4704–4710, 2014.

[33] Y. S. Lee, J. Heo, S. C. Siah, J. P. Mailoa, R. E. Brandt, S. B. Kim, R. G. Gordon, and T. Buonassisi. "Ultrathin amorphous zinc-tin-oxide buffer layer for enhancing heterojunction interface quality in metal-oxide solar cells". *Energy & Environmental Science*, 6(7):2112, 2013.

[34] B. Lu, N. Sun, M. Li, and H. Dong. "Nickle oxide based bulk heterojunction flexible solar cells". 512-515:109–112, 2012.

[35] B. K. Meyer, A. Polity, B. Farangis, Y. He, D. Hasselkamp, Th Kramer, and C. Wang. "Structural properties and bandgap bowing of Zn(O,S) thin films deposited by reactive sputtering". *Applied Physics Letters*, 85(21):4929, 2004.

[36] T. Minami, T. Miyata, K. Ihara, Y. Minamino, and S. Tsukada. "Effect of ZnO film deposition methods on the photovoltaic properties of ZnO-Cu_2O heterojunction devices". *Thin Solid Films*, 494(1-2):6, 2006.

[37] T. Minami, Y. Nishi, and T. Miyata. "high-efficiency Cu_2O-based heterojunction solar cells fabricated using a Ga_2O_3 thin film as n-type layer". *Applied Physics Express*, 6(4):4, 2013.

[38] T. Minami, Y. Nishi, T. Miyata, and J. Nomoto. "High-efficiency oxide solar cells with ZnO/Cu_2O heterojunction fabricated on thermally oxidized Cu_2O sheets. *Applied Physics Express*, 4(6):062301, 2011.

[39] A. Mittiga, E. Salza, F. Sarto, M. Tucci, and R. Vasanthi. "Heterojunction solar cell with 2% efficiency based on a Cu_2O substrate". *Applied Physics Letters*, 88(16):2, 2006.

[40] K. Nakashima, T. Kumazawa, T. Kobayashi, T. Mise, and T. Nakada. "Wide-gap Cu(In,Ga)Se_2 solar cells with Zn(O,S) buffer layers prepared by atomic layer deposition". *Japanese Journal of Applied Physics*, 51(10):3, 2012.

[41] J. Nelson. *The Physics of Solar Cells*. Imperial College Press, London, 2003.

[42] L. C. Olsen, F. W. Addis, and W. Miller. "Experimental and theoretical studies of Cu_2O solar cells". *Solar Cells*, 7(3):247–279, 1982.

[43] L. C. Olsen, R. C. Bohara, and M. W. Urie. "Explanation for low-efficiency Cu_2O schottky-barrier solar cells". *Applied Physics Letters*, 34(1):47, 1979.

[44] H. L. Pan, T. Yang, B. Yao, R. Deng, R. Y. Sui, L. L. Gao, and D. Z. Shen. "Characterization and properties of Zn(O,S) alloy films fabricated by radio-frequency magnetron sputtering". *Applied Surface Science*, 256(14):4621–4625, 2010.

[45] L. Papadimitriou, N. A. Economou, and D. Trivich. "Heterojunction solar-cells on cuprous oxide". *Solar Cells*, 3(1):73–80, 1981.

[46] H. H. Park, R. Heasley, and R. G. Gordon. "Atomic layer deposition of Zn(O,S) thin films with tunable electrical properties by oxygen annealing". *Applied Physics Letters*, 102(13):5, 2013.

[47] J. Perrenoud, L. Kranz, S. Buecheler, F. Pianezzi, and A. N. Tiwari. "The use of aluminium doped ZnO as transparent conductive oxide for CdS/CdTe solar cells". *Thin Solid Films*, 519(21):7444–7448, 2011.

[48] B. P. Rai. "Cu_2O solar-cells - a review". *Solar Cells*, 25(3):265–272, 1988.

[49] K. Ramanathan, J. Mann, S. Glynn, S. Christensen, J. Pankow, J. Li, J. Scharf, L. Mansfield, M. Contreras, and R. Noufi. "A comparative study of Zn(O,S) buffer layers and CIGS solar cells fabricated by CBD, ALD, and sputtering". *38th IEEE Photovoltaic Specialists Conference*, 2012.

[50] D. Scanlon and G. Watson. "Uncovering the complex behavior of hydrogen in Cu_2O". *Physical Review Letters*, 106:4, 2011.

[51] D. K. Schroder. *Semiconductor Material and Device Characterization.* John Wiley & Sons, Inc., Hoboken, New Jersey, 2006.

[52] W. Shockley and H. J. Queisser. "Detailed balance limit of efficiency of pn junction solar cells". *Journal of Applied Physics*, 32(3):510–519, 1961.

[53] SunPower Corporation. "A-300 Solar Cell". `www.cs.wmich.edu/~sunseeker/files/A-300%20data%20sheet.pdf`, 2014. [Online; accessed November 2014].

[54] T. Suzuki. "X-ray study on the binding properties of Cu_2O and Ag_2O crystals". *Journal of the Physical Society of Japan*, 15:2018, November 1960.

[55] S. M. Sze and K. K. Ng. *Physics of Semiconductor Devices.* John Wiley & Sons, Inc., Hoboken, New Jersey, 2007.

[56] J. Tauc. "Optical properties and electronic structure of amorphous Ge and Si ". *Materials Research Bulletin*, 3(1):37 – 46, 1968.

[57] Tesla Motors, Inc. "Using energy efficiently". `http://www.teslamotors.com/goelectric/efficiency`, 2014. [Online; accessed November 2014].

[58] R. R. Thankalekshmi and A. C. Rastogi. "Structure and optical band gap of $ZnO_{1-x}S_x$ thin films synthesized by chemical spray pyrolysis for application in solar cells". *Journal of Applied Physics*, 112(6):10, 2012.

[59] D. Trivich and J. A. Assimos. "The photoelectric threshold, work function, and surface barrier potential of single-crystal cuprous oxide". *Physica Status Solidi (a)*, 26(2):12, 1974.

[60] D. Trivich, E. Y. Wang, R. J. Komp, K. Weng, and A. Kakar. "Cuprous-oxide photovoltaic cells". *Journal of the Electrochemical Society*, 124(8):C318–C318, 1977.

[61] D. W. Turner and M. I. Al Jobory. "Determination of ionization potentials by photoelectron energy measurement". *The Journal of Chemical Physics*, 37(12):3007–3008, 1962.

[62] C. Wadia, A. P. Alivisatos, and D. M. Kammen. "materials availability expands the opportunity for large-scale photovoltaics deployment". *Environmental Science Technology*, 43(6):2072–7, 2009.

[63] L. Wang, H. Wu, S. R. Desai, and L. Lou. "Electronic structure of small copper oxide clusters: from Cu_2O to Cu_2O_4". *Physical Review B*, 53:8028–8031, 1996.

[64] P. Wang, X. Zhao, and B. Li. "ZnO-coated cuo nanowire arrays: fabrications, optoelectronic properties, and photovoltaic applications". *Optics Express*, 19(12):11271–9, 2011.

[65] S. S. Wilson, J. P. Bosco, Y. Tolstova, D. O. Scanlon, G. W. Watson, and H. A. Atwater. "Interface stoichiometry control to improve device voltage and modify band alignment in ZnO/Cu_2O heterojunction solar cells". *Energy & Environmental Science*, 7:3606–3610, 2014.

[66] L. M. Wong, S. Y. Chiam, J. Q. Huang, S. J. Wang, J. S. Pan, and W. K. Chim. "Growth of Cu_2O on Ga-doped ZnO and their interface energy alignment for thin film solar cells". *Journal of Applied Physics*, 108(3):033702, 2010.

[67] C. Xiang, G. M. Kimball, R. L. Grimm, B. S. Brunschwig, H. A. Atwater, and N. S. Lewis. "820 mV open-circuit voltages from Cu_2O/CH_3CN junctions". *Energy & Enviormental Science*, (4):8, 2011.

[68] H. Xu, L. Zhu, J. Jiang, H. Cai, W. Chen, L. Hu, Y. Guo, and Z. Ye. "Wavelength tunable photoluminescence of $ZnO_{1-x}S_x$ alloy thin films grown by reactive sputtering". *Journal of Applied Physics*, 114(8):083522, 2013.

[69] J. Xue and R. Diekmann. "The high-temperature phase diagram of the Cu-O system in the stability region of cuprous oxide". *High Temperatures-High Pressures*, 24:271–284, 1990.

[70] Y. Zhu, K. Mimura, J. Lim, M. Isshiki, and Q. Jiang. "Brief Review of Oxidation Kinetics of Copper at 350Â° C to 1050Â° C". *Metalurgical and Materials Transactions A*, 37A:1231–1237, 2006.